

Die approbierte Originalversion dieser Dissertation ist an der Hauptbibliothek der Technischen Universität Wien aufgestellt und zugänglich (<http://aleph.ub.tuwien.ac.at/>).

The approved original version of this thesis is available at the main library of the Vienna University of Technology on the open access shelves (<http://aleph.ub.tuwien.ac.at/>).



TECHNISCHE
UNIVERSITÄT
WIEN

VIENNA
UNIVERSITY OF
TECHNOLOGY

DISSERTATION

SPATIAL AND STATISTICAL ANALYSIS OF THERMAL SATELLITE IMAGERY FOR EXTRACTION OF COAL FIRE RELATED ANOMALIES

ausgeführt zum Zwecke der Erlangung des akademischen Grades eines
Doktors der Naturwissenschaften unter der Leitung von

Univ. Prof. Dipl. Ing. Dr. Wolfgang Wagner
122

Institut für Photogrammetrie und Fernerkundung

eingereicht an der Technischen Universität Wien
Fakultät für Technische Mathematik und Vermessung und Geoinformation

von

Jianzhong ZHANG

0227507

Grubenweg 7, Gilching D-82205, Deutschland

Wien, am 2004-04-01

Abstract

Coal fires, either man-made or resulting from spontaneous combustion, not only cause losses of natural resources, but also cause severe environmental problems. In China, coal fires are spread out over the whole northern part of the country. Therefore it is extremely difficult to keep an overview of the development of known fires as well as of newly developing ones. The study undertaken in this thesis focuses on the development of a practical approach for the extraction of coal fire related thermal anomalies at the land surface over large areas using remote sensing data sets.

An overview of the theory and case studies on detecting coal fires using remote sensing techniques is given in a literature review. The surface features and by-products of coal fires include pyro-metamorphic rocks, fumarolic minerals, burnt pits and trenches, subsidence and cracks, as well as surface thermal anomalies. These features can be detected from visible, near infrared, short-wave infrared, radar and thermal infrared remote sensing imageries. The ability to detect these features is limited by the spectral, spatial and temporal resolution of the remote sensing data.

Thermal characteristics of coal fires and their thermal anomalies were analyzed through simulated coal fires, field measurements in the study areas, and thermal anomalies on the images. Two simulated coal fires were studied during a field experiment at DLR, Oberpfaffenhofen, Germany. The results indicated that the inner temperature of such a coal fire is above 1000°C. The surface radiant temperatures of a coal fire range from 300 to 900°C. All background materials, such as sand and grasses, have relatively high radiant temperatures during daytime and comparatively low temperatures during night-time, which makes the contrast between the coal fire and the background higher during night-time.

From field measurements, it is known that surface temperature can vary up to 28°C within a small sand dune. In a coal waist pile, temperature for a slope facing to the Southeast can be 20°C higher than that for a slope facing to the North between 10:00 to 14:00. The temperature variance caused by uneven solar heating can overprint thermal anomalies related to coal fires. Underground coal fires can form thermal

anomalies above the covering bedrocks on the surface. The anomalies can best be observed in night-time data. Predawn is the optimum time for coal fire detection with thermal remote sensing techniques. Temperature profiles show that one hour after sunrise, a coal fire related thermal anomaly, only 1m away from a crack was overprinted by the effects of solar heating. Thermal anomalies did not extend for more than 3m away from the crack. The width of thermal anomalies does not decline as the background temperatures increase. The thermal pattern in remote sensing as well as field data above a coal fire actually is defined by the pattern of cracks.

Through analyses of the statistical characteristics of the thermal anomalies in different scenes of daytime and night-time Landsat-7 ETM+ band 6 images, it is shown that the minimum, median and mean values of a coal fire related thermal anomaly on ETM+ images are not only higher than its background, but also decrease with the increase of the dimension of the accounted background. Standard deviation of a coal fire or a thermal anomaly on night-time ETM+ images is higher than that of the background. On daytime ETM+ images it is smaller than that of the background. The minimum values of the thermal anomalies are much lower than the highest value of the background. Therefore thermal anomalies are not outstanding, and are hard to separate. Coal fires form thermal anomalies on images with their distinct start and end DN values. During detection, every coal fire should be counted individually. ETM+ night-time images are suitable for general survey of coal fires in large areas. About eighty percent of known coal fires can be detected.

A practical approach for the extraction of coal fire related thermal anomalies in a large area using Landsat-7 band 6 data was developed in this study. Most coal fires form thermal anomalies on the surface, which are smaller than a pixel size of Landsat-7 ETM+ band 6 image. They form a kind of weak and local thermal anomalies in the image. The thermal anomalies can be extracted within subsets of the image. Subsets of an image can be defined using a window of small size, moving over the image step by step. In such a window, thermal anomalies and their background can be separated through a threshold, which is defined as the first histogram turning point after the mean plus the standard deviation of the window. A proper threshold can minimize the number of false alarms. A result map records how many times a pixel in the image

has been counted as a thermal anomaly. When a threshold is set, the result map can be sliced to a bit map representing coal fire induced thermal anomalies and the non-fire area. Furthermore, some false alarms, such as water bodies and slopes heated by the sun, can be removed according to the statistical analysis based on known thermal characteristics of coal fires and contextual information.

The background temperature, the quality of the thermal remote sensing data, and the size and strengths of the coal fires are the factors which determine the detectability of coal fires. The performance of the algorithm for the extraction of coal fire related thermal anomalies is independent on these factors, while the result of the algorithm is dependent on the size of the moving window and the final cut-off percentage. Thermal anomalous clusters with different extent (for example 0 to 64 pixels in size in the Wuda area) can be well extracted by the algorithm using different size of the moving window. Sometimes 100% of the thermal anomalous pixels in a cluster can be delineated. The best size of the moving window for detecting coal fires in a large area in Northwest of China is the accumulative window ranging from 11*11 to 35*35 pixels for Landsat-7 ETM+ band 6 data.

To evaluate the performance, the algorithm is applied to satellite data covering an area in Xinjiang Uygur Autonomous Region, about 2000 km away from the main study areas. Thermal anomalies extracted by the algorithm here coincide well with the known locations of coal fires. Using the thermal anomalies automatically extracted from Landsat-7 ETM+ thermal data based on this algorithm, plus the land cover information derived from the multi-spectral non-thermal bands, the areas with a high potential for coal fire occurrence can be defined. Ground truth studies in areas with a high coal fire potential, which have never been investigated before, confirmed the presence of active coal fires, beforehand only picked up in remote sensing data. These assessments validate the algorithm to have the potential to investigate unknown areas. This makes it possible to set up an operational detection and monitoring system for coal fires in larger areas, such as northern China.

Acknowledgments

This thesis is the result of three years of work whereby I have been supported by many people. Since it is impossible to thank them all, I will therefore only mention those without whom this study could never have been accomplished.

The first person I would like to thank is my supervisor Wolfgang Wagner. His great experience in remote sensing research and his good knowledge of the coal fire project gave him the opportunity to always point out my mistakes in research and to guide me along a consistent way. I owe him lots of gratitude for having shown me a clear and structured way of research. I am really glad that I had Wolfgang Wagner's influence in my life for the past three years.

I would like to thank my team leader Stefan Voigt who kept an eye on the progress of my work and always was available when I needed his advice. It was Stefan who kept me working hard and finishing the research in time. Many thanks to him for teaching me the German way of working and helping me to understand the culture of Germany.

I would also like to thank my co-supervisor Paul van Dijk from ITC. His abundant geological knowledge gave me a great help during the field work. I could always rely on Paul's advice when I needed. Thanks also for his efforts on solving my administrative problems. Since Paul has already supervised my master study, I am quite happy to have him as my doctor father also.

Thanks to Claudia Kuenzer. The strict and extensive comments and many discussions and the interactions with Claudia had a direct impact on the final form and quality of this thesis. I feel so lucky to be one of her friends, especially to share the same working room with her. I am grateful to Anke Tetzlaff, and Andreas Hirner who helped me to revise parts of this thesis. Thanks to Andreas Petrocchi for the help on my IDL programming. I thank Martin Habermeyer for our discussion and supplying me the literatures on anomaly detection.

In addition, I greatly appreciate the supports during the 2002 and 2003 field campaigns provided by Yulin Sun, Yaorong Jia, Jianwei Ma, Jun Wang, Xiangmin Zhang,

Jiahong Li, Jianmin Zhang, and Christoph Hecker. I would have lost a lot of time in the coal fire areas if I had not got the guidance from Yulin Sun.

My leaders and colleagues of the German Remote Sensing Data Center (DFD), German Aerospace Center (DLR) all took care of me and gave me the feeling of being at home at work. Many thanks to Margot Pfeil, Elfi Pioszyk, Torsten Riedlinger, Guenter Strunz, Harald Mehl and Stefan Dech.

I feel a special gratitude towards my friends for their cheerful assistance and the necessary distraction. Thanks to Xueliang Wang, Shimin Zhang, Youli Li, Liding Chen, Jinshan Ye, Hongfei Hou, Xinmin Tang, Ding Zheng, Yuxian Sun, Yaoping Nie, Weimin Wang, Boqin Zhu, Zhongke Zhang, Qizhong Lin, Yanning Guan, and Shan Guo for showing me the beautiful part of the life. Thanks to Han-Peter Thamm, Heinz Pfeil and Margot Pfeil for the good time we spent together.

Finally, I would express my heartfelt thanks to my parents and my sisters for their love and supports, and a very special thank to Xiangrong Bao for her encouragement and assistance.

TABLE OF CONTENT

Acknowledgments

Abstract

Table of Content	i
List of Figures	vi
List of Tables	xiv
List of Appendixes	xv
List of Abbreviations	xvi
Chapter 1 INTRODUCTION	1
1.1 Problem Identification	2
1.2 Aim and Objectives	4
1.3 Methodology	4
1.3.1 Reference analyses.....	4
1.3.2 Fieldwork.....	5
1.3.3 Algorithm development and validation	5
1.4 Outline of the Thesis	5
Chapter 2 COAL FIRE AND ITS RELATED SURFACE FEATURES	7
2.1 Coal Fires, Their Causes and Classification.....	7
2.2 Rocks and Minerals Produced by Coal Fires	8
2.3 Coal Fire Generated Geomorphology.....	12
2.4 Surface Temperature Related to the Coal Fires.....	15
2.5 Conclusion.....	18

Chapter 3 STATE OF THE ART	19
3.1 Detecting Surface Features of Coal Fires Using Remote Sensing	19
3.1.1 Visible and near infrared remote sensing	19
3.1.2 Short-wave infrared remote sensing	21
3.1.3 Radar remote sensing.....	23
3.2 Detecting Thermal Anomalies of Coal Fires Using Thermal Remote Sensing	24
3.2.1 Airborne thermal remote sensing	24
3.2.2 Using space-borne thermal remote sensors for detecting coal fire thermal anomalies	27
3.2.3 Influence factors in the isolation of fires from other areas.....	32
3.3 Summary and Discussion	34
Chapter 4 DESCRIPTION OF THE STUDY AREAS & DATA SETS.....	37
4.1 Location of the Study Areas	37
4.2 Geography	38
4.2.1 Climate and hydrology	38
4.2.2 Soils and vegetation	38
4.2.3 Economy	39
4.3 Geology	40
4.4 Coal Fires	41
4.4.1 Coal fires in Wuda	41
4.4.2 Coal fires in Ruqigou.....	43
4.4.3 Coal fires in Gulaben.....	44
4.5 Coal Mining	45
4.6 Data Available	46

Chapter 5 THEORY.....	49
5.1 Thermal Processes and Properties	49
5.1.1 Heat, temperature, radiant flux and heat transfer	49
5.1.2 Radiant energy peaks and Wien's displacement law.....	50
5.1.3 Blackbody concept, emissivity and radiant temperature	51
5.2 Radiant Temperature Retrieval from Airborne IR Scanners and Landsat-7 ETM+ Band 6	52
5.2.1 Airborne IR scanners and their radiant temperature retrieval.....	52
5.2.2 Radiant temperature retrieval from landsat-7 ETM+ band 6.....	52
5.3 Thermal Data of Band 3-5 μm and 8-14 μm for Underground Coal Fire Detection.....	55
5.3.1 Detecting full pixel coal fires	55
5.3.2 Detecting sub-pixel coal fires	56
CHAPTER 6 THERMAL CHARACTERISTICS OF COAL FIRES	61
6.1 Thermal Characteristics of Simulated Coal Fires	61
6.1.1 Setting of the experiment.....	61
6.1.2 Data acquisition	64
6.1.3 Results.....	65
6.1.4 Conclusion	73
6.2 Thermal Characteristics of Coal Fires in the Study Areas	74
6.2.1 Field surface temperature measurements of a sand dune	74
6.2.2 Field surface temperature measurements of a coal dump pile.....	79
6.2.3 Field temperature measurements of cracks.....	81
6.2.4 A night-time temperature profile on coal fire No.12.....	87
6.2.5 A temperature profile on coal fire No.8	89

6.2.6 Discussion.....	89
6.3 Thermal Characteristics of Coal Fires in ETM+ Images (Day And Night Images).....	90
6.3.1 Data input.....	90
6.3.2 Methodology and image processing	90
6.3.3 Results.....	93
6.3.4 Conclusion and discussion.....	100
Chapter 7 ALGORITHM DEVELOPMENT FOR EXTRACTION OF COAL FIRE RELATED THERMAL ANOMALIES	103
7.1 Review of the Previous Algorithms for Anomaly Extraction	104
7.1.1 Spatial filtering	104
7.1.2 Image classification	105
7.1.3 Anomaly detection.....	106
7.2 Algorithm Development for the Extraction of Coal Fire Related Thermal Anomalies	108
7.2.1 Dividing a night-time ETM+ image into subsets using a moving window	108
7.2.2 Separation of thermal anomalies and their background based on histogram features	109
7.2.3 Presenting the output result retrieved from a suitable window size, moving steps and cut-off percentage.....	112
7.3 Removing False Alarms According to Texture Analysis Results	113
7.4 Discussion and Conclusion.....	118
Chapter 8 RESULT EVALUATION AND VALIDATION	119
8.1 Assessment of the Algorithm for Extraction of Coal Fire Related Thermal Anomalies	119

8.1.1 Data input.....	119
8.1.2 Methodology and data processing	119
8.1.3 Results and discussions.....	126
8.1.4 Conclusions.....	131
8.2 Validation of Results for Applying the Algorithm to Other ETM+ Images.....	131
8.2.1 Validation of result for extraction of thermal anomalies related to coal fires in xinjiang	132
8.2.2 Validation of result for extraction of thermal anomalies related to coal fires using day time ETM+ band 6 data in the wuda area.....	134
8.3 Detecting Unknown Coal Fires in a Previously Non-Studied Area Using Landsat-7 ETM+ Data	136
8.3.1 Methodology.....	136
8.3.2 Results.....	138
8.3.3 Discussion and conclusion.....	139
Chapter 9 CONCLUSIONS & OUTLOOK.....	141
9.1 Conclusions	141
9.2 Outlook.....	143
References	145
Appendix	157

List of Figures

Figure 2.1 Photograph of pyro-metamorphic rocks. A : Baked rock; B: Porcelanite; C: Molten rock. Specimens are from Xinjiang, China.

Figure 2.2 Field photograph of fumarolic mineral (Salmiac) in Xinjiang, China.

Figure 2.3 Field photograph of a typical burnt pit in Xinjiang, China.

Figure 2.4 Field photograph of a typical burnt trench in Xinjiang, China.

Figure 2.5 Field photograph of typical cracks in Xinjiang, China. The width of the cracks ranges between 0.1 to 1 meter.

Figure 2.6 A diagram of coal fires and their related features. 1: Original rock; 2: Coal seam; 3: Soil; 4: Ash; 5: Molten rock; 6: Baked rock; 7: Coal mine area; 8: Pillar; 9: Underground coal mine fire; 10: Surface coal mine fire; 11: Underground nature fire; 12: Surface nature fire; 13: Fumarolic mineral; 14: Burnt trench; 15: Burnt pit. 16: Crack; 17: Subsidence.

Figure 2.7 Field along-strike measurement of a temperature profile of coal fire No. 141, 142 and 143 in Xinjiang, China (measured at noon time of 17 August 1995). I: Background temperature; II: Low-amplitude thermal anomalies; III: Medium-amplitude thermal anomalies; IV: High-amplitude thermal anomalies (After Zhang, 1998).

Figure 2.8 A thermal profile over burning coal seams in Jharia coal field, India (After Mukherjee, et al., 1991).

Figure 2.9 A profile of surface temperature (field measurements) above subsurface fires in Jharia coal field, India. The background temperatures are lower than 24°C (After Gupta & Prakash, 1998).

Figure 3.1 Average reflectance of original rocks and pyro-metamorphic rocks in the wavelength of 0.5-0.6 μm , 0.6-0.7 μm , 0.7-0.8 μm and 0.8-1.1 μm in Shaanxi and Xinjiang, China, respectively. 1: Original rocks in Shaanxi, China; 2: Pyro-metamorphic rocks in Shaanxi, China; 3: Original rocks in Xinjiang, China; 4: Pyro-metamorphic rocks in Xinjiang China (Data from Guan & van Genderen, 1997).

Figure 3.2 Spectra of pyro-metamorphic rocks. 1: Dark gray siltstone with black organic material remnants; 2: Yellowish gray slightly baked siltstone; 3: Light yellow baked siltstone. From a original rock to a baked rock, the reflectance increases with temperature (After Zhang, 1996).

Figure 3.3 Spectra of pyro-metamorphic rocks. 4: Yellowish brown burnt siltstone with black molten spots; 5: Black molten siltstone; 6: Black molten rock with vesicles. From a heavily backed rock to a molten rock, the reflectance decreases with temperature increase (After Zhang, 1996).

Figure 3.4 Surface temperatures of a light yellow mud hill. Temperatures were measured at the local time 12:00-12:05, when the sun zenith is 33.6° and the sun azimuth is 174° (After Guan & van Genderen, 1997).

Figure 4.1 Location of the study areas

Figure 4.2 Coal fires in the study areas. Left: Wuda area; Right: Ruqigou and Gulaben area. Red: coal fire area mapped in the field; Green: thermal anomalous pixels interpreted from the background image; Background image: nighttime Landsat 7 band 6, 226-211, acquired on 28 September 2002; Number 1-45: coal fire reference number. Coal fires in Wuda area have been numbered from 1-17. Coal fires in Gulaben area have been numbered from 21-25. Coal fires in Rujigou have been numbered from 31-45.

Figure 4.3 Open cast mining in Dafeng coal mine, Ruqigou coalfield

Figure 4.4 Open cast mining in a private pit, Wuda coalfield

Figure 5.1 Spectral distribution curves of energy radiated from objects at different temperatures. The radiation peaks are $9.7\ \mu\text{m}$, $7.2\ \mu\text{m}$, $5.8\ \mu\text{m}$ and $4.8\ \mu\text{m}$ for temperatures of 300, 400, 500 and 600 °K respectively.

Figure 5.2 Relation of DN_s and temperature of Landsat 7 ETM+ band 6

Figure 5.3 A sub-pixel sized coal fire occupying p portion of the pixel area.

Figure 5.4 Threshold line of temperature and portion for detecting a sub-pixel coal fire by different data sets.

Figure 6.1 Map of test site at DLR, Oberpfaffenhofen

Figure 6.2 Setting of the Simulated Surface Coal Fire. HG: High grass; LG: Low grass; DG: Dry grass; EH: Electric heater; SC: Sand cover. Drawing in the lower right shows the dimension of the grill. The sand cover occupies an area of 8.5m*8.5m

Figure 6.3 Setting of the Simulated Underground Coal Fire. HG: High grass; LG: Low grass. Drawing in the lower right shows the dimension of the grill. Arrows point on the measuring spots for FRU, FRUN and FRUW.

Figure 6.4 Surface Temperature of the Simulated Underground Coal Fire. FRUN: Radiant temperature measured at the center of the North Slope of the sand cone; FRUE: East slope; FRUS: South slope; FRUW: West slope; FRU: Top; AT: Air temperature; SCB: Background temperature for the sand cover. From 19:30, the temperature of the background was the lowest. Heat from the fire transferred to the top of the sand cone within one hour. The top of the sand cone is warmer than the background by an average temperature of 3°C.

Figure 6.5 Diurnal Radiant Temperature Variations for Background Materials. AT: Air temperature; B: Background; HG: High grass; LG: Low grass; DG: Dry grass. They show the same trend: High radiant temperature during daytime and low temperature during night-time.

Figure 6.6 Diurnal Radiant Temperature Variations for Measurements with Different Distance to the Coal Fire. Group I: Measuring spots 2 meters away from the fire; Group II: 2.8 meters; Group III: 4 meters; Group IV: 4.5 meters; Group V: 5.6 meters. Thermal anomalies caused by the fire can not reach further than 4.5 meters.

Figure 6.7 Diurnal contour maps of radiant temperatures for the sand cover. Arrows indicate the main heat transfer directions. They change to every direction.

Figure 6.8 MP 50 line scanner images. X: Rows; Y: Columns; Z: Temperature (°C); S.U.F.: Simulated underground coal fire; EH: Electric heater. The coal fire with a dimension of 1m*1m forms an outstanding thermal anomalous cluster in MP 50 line scanner images, whose spatial resolution is 5cm.

Figure 6.9 Setting of measuring points on a sand dune in Wuda coal mine area. N: North; E: East; S: South; W: West; 1-8, T: measuring points. The drawings show the cross section of the sand dune from North to South and East to West.

Figure 6.10 Average surface temperatures for slopes facing to North, East, South and West of a sand dune in Wuda coal mine area. Average_N: average of temperature measurements for measuring points N1-N8 and T; Average_E: average of measuring points E1-E6 and T; Average_S: average of S1-S9 and T; Average_W: average of W1-W9 and T; SR: sunrise; SS: sunset; TM: TM overpass. The slope facing to the East reaches its highest temperature at 13:00. The slope facing to the North, South and West reach their highest temperatures at 14:00.

Figure 6.11 Surface temperature variance of a sand dune in Wuda coal mine area. N_{diff} , E_{diff} , S_{diff} , W_{diff} : temperature variance within a slope facing North, East, South and West; A_{diff} : average temperature variance among slopes; E_{diff} : temperature variance in the sand dune. Arrows point on the maximum values of the temperature variances within East, South, North and West slopes. Temperature measurements could vary 28°C in a sand dune.

Figure 6.12 Setting of measuring points on a coal dump pile in Wuda coal mine area. NL, NM, NU, SEL, SEM, and SEU: measuring points; 350° and 135°: slope dip direction.

Figure 6.13 Surface temperatures and their variance for a coal dump pile in Wuda coal mine area. NL, NM, NU, SEL, SEM, and SEU: temperature for the correspondent measuring point; SR: sunrise; SS: sunset; TM: TM overpass. MAX-MIN: temperature variance.

Figure 6.14 Surface temperatures for a crack in Wuda coal mine area. Lower: setting of measuring points; middle and upper: temperature profile. Temperature for the crack fire is relatively stable during the day. The thermal anomaly does not extend more than 3m from the crack. The width of the thermal anomaly does not decline as the background temperature increases.

Figure 6.15 Underground temperature at measuring points NE3 and NE6. A@B: at measuring point A and time B. One hour after the sunrise, thermal anomaly to be formed 1m away from the coal fires crack was overprinted by the sun uneven heating. At NE3, heat from the sun reaches 3.2cm below the surface at 09:30 and 6.4cm at 11:30. At NE6, heat from the sun reaches 6.4cm below the surface at 09:30 and more than 12.8cm at 11:30.

Figure 6.16 Temperature profile for a crack at coal fire No. 8, Wuda coal mine area (measured on September 10 and 14, 2002). From -2cm to the surface, temperature drops rapidly. On the surface 30cm away from the crack temperatures dropped to the normal background level.

Figure 6.17 A temperature profile on coal fire No.12, Wuda coal mine area (measured at 21:55 on 12 September 2002). Underground coal fire forms a thermal anomaly above the covering bedrocks on the surface as shown by the dot line.

Figure 6.18 A temperature profile on coal fire No.8. B: background; FC: fire area with cracks; FS: fire area with surface subsidence. High surface temperature for an underground coal fire can be measured only on cracks or close to cracks (within 30cm).

Figure 6.19 Illustration of neighbourhood pixels with different spatial extends.

Figure 6.20 Determination of background pixels in the Wuda area. 1: Thermal anomalous pixels; 2: Pixels for background neighborhood 1; 3: Pixels for background neighborhood 6; 4: Pixels for background neighborhood 16.

Figure 6.21 Maximum, mean and minimum values of thermal anomalies on a night-time ETM+ image acquired in 2002. Maximum, mean and minimum values of a thermal anomaly are higher than its background. Mean and minimum decrease with the increase of the spatial extends of the backgrounds.

Figure 6.22 Standard deviation of thermal anomalies on a night-time ETM+ image acquired in 2002. Standard deviation of a thermal anomaly is higher than its background on a night-time thermal image.

Figure 6.23 Standard deviation for thermal anomalous areas on a daytime ETM+ image received in 2002. Standard deviation of a thermal anomalous area is smaller than its background on a daytime thermal image.

Figure 6.24 Skewness for thermal anomalous areas on a day ETM+ image received in 2002. Skewness of a thermal anomalous area is higher than its background on a daytime thermal image.

Figure 6.25 Histogram for field coal fire areas on a night time ETM+ image acquired in 2002. Parts of the histogram for coal fire areas surveyed in the field overlap with background histogram. They can not be detected using an ETM+ band 6 night-time image

Figure 6.26 Histogram for thermal anomalous areas on a night-time ETM+ image acquired in 2002. Different thermal anomalies related to coal fires have different start and end DN values.

Figure 6.27 Histogram for thermal anomalous areas on a daytime ETM+ image acquired in 2002. Less thermal anomalous pixels detected in daytime images than in night-time images.

Figure 7.1 Landsat-7 ETM+ band 6 night-time image 226-211 (path-row) acquired on 25 September 2001. It has 3778 columns by 3589 lines, covering an area of 185km by 185km. High DN values are related to the water body. Coal fire thermal anomalies in Wuda and Ruqigou area are not outstanding in this large-scale view.

Figure 7.2 Histograms of Landsat-7 ETM+ band 6 data. A: whole scene (3778 * 3589); B: Ruqigou area (300*300); C: Gulaben coal fire area (50*50); D: One coal fire in Gulaben (10*10). In D, Line: histogram of coal fire thermal anomalies; Dot line: histogram of the total pixels; Line-dot-line: histogram of the background. In a small subset of an image, coal fire thermal anomalies are easier to be separated from their background.

Figure 7.3 Moving window method. Subsets of an image can be derived through a window moving on it. A pixel on the image will be sampled $(M1 * N1) / (X * Y)$ times. A pixel in coal fire area will be sampled in different subsets.

Figure 7.4 Histograms of the known coal fire thermal anomalies and the background. 1: Histogram of the background with 100 pixels, which are chosen randomly from the known area in Gulaben. 2: Histogram of 100 known thermal anomalous pixels in the same area. 3: Histogram of the together 200 pixels. A, B, C, D, E, and F: thresholds for distinguishing background and thermal anomalies.

Figure 7.5 Colour Composite image of Wuda (Red: Thermal anomalies extracted from ETM+ night-time band 6; Green: ETM+ band 3; Blue: ETM+ band 2). W:

thermal anomalies caused by the water body. S: thermal anomalies caused by the sun uneven heating high thermal inertia materials. P: thermal anomalies caused by industrial plants. F: thermal anomalies caused by coal fires.

Figure 7.6 Thermal anomaly fine-tuning. A: Original Landsat-7 ETM+ band 6 image; B: Indexed thermal anomalous cluster image. C: Water body and illuminated slopes have been removed by using the standard deviation characteristics. D: Sparsely distributed small non-fire related thermal clusters have been removed by using the mean characteristics.

Figure 7.7 Flow chart for extraction of coal fire related thermal anomalies

Figure 8.1 Thermal anomalies Extracted by using different size of the moving window. A: Input image; B: Thermal anomalies extracted by a 3*3 moving window; C: Thermal anomalies extracted by a 27*27 moving window; D: Thermal anomalies extracted by a 51*51 moving window.

Figure 8.2 Threshold images for extraction thermal anomalies using different size of the moving window. A: Threshold image of the 3*3 moving window; B: Threshold image of the 27*27 moving window; C: Threshold image of the 51*51 moving window.

Figure 8.3 A thermal anomaly image and a threshold image. A: Sum of the normalized thermal anomaly images for window size 3*3 to 51*51 with interval of 2*2. B: Mean of the threshold images for window size 3*3 to 51*51 with interval of 2*2.

Figure 8.4 Result maps for using different cut-off percentages. A: cut-off percentage 50%; B: cut-off percentage 70%; C: cut-off percentage 90%.

Figure 8.5 Interpreted thermal anomaly image in Wuda. A: Bit map. B: Clustered map.

Figure 8.6 Evaluation of window size and cut-off percentage for extraction thermal anomalous pixels in the clusters with different number of pixels; Upper: Cluster 8 with 42 known thermal anomalous pixels; Middle: Average of 3 clusters with 8 known thermal anomalous pixels; Lower: Average of 5 clusters with 1 known thermal anomalous pixel.

Figure 8.7 Evaluation of window size and cut-off percentage for extracting thermal anomalous pixels vs. false alarms in the Wuda area. Black: cut-off percentage 70%; Red: cut-off percentage 80%; Green: cut-off percentage 90%.

Figure 8.8 Accuracy evaluation of window size and cut-off percentage for extraction thermal anomalous pixels in the Wuda area. Accurate result can be acquired by using the 17*17 to 35*35 moving windows.

Figure 8.9 Extraction of thermal anomalies in Xinjiang, China. Upper: The original Landsat-7 ETM+ band 6 data. Lower: Result map of thermal anomalies extracted by the algorithm. Red: thermal anomalous pixels with high possibility to be caused by coal fires. Green: thermal anomalous pixels possibly caused by coal fires.

Figure 8.10 Extraction of thermal anomalies in a day time image in the Wuda area. A: The original Landsat-7 ETM+ band 6 data. B: Thermal anomalies extracted by the algorithm using the starting point at mean plus standard deviation. Red: thermal anomalous pixels; C: Thermal anomalies extracted by the algorithm using the starting point at mean plus two times standard deviation. Red: cut-off percentage: 85%; Magenta: cut-off percentage: 70%; Cyan: cut-off percentage: 50%.

Figure 8.11 Combination map of thermal anomalies and land covers. Thermal anomalies are automatically derived from night-time Landsat 7 ETM+ thermal band. Land cover information is extracted based on the spectral signatures using daytime non-thermal bands. Four circled areas are interpreted as the favourite places for coal fire occurrence. The area marked by orange is the newly detected coal fire area. In the upper amplified window the red arrows point on the five thermal anomalies that have been verified in the field as coal seam fires, while in the lower one the arrow points on the thermal anomaly formed by coal waist pile fires.

Figure 8.12 A newly detected coal fire in a previously non-studied area. The arrow points on the place where a fire is burning underground.

List of Tables

Table 2.1 The classification of coal fires

Table 4.1 Dimensions of coal fires in the Wuda coalfield

Table 4.2 Dimensions of coal fires in the Ruqigou coalfield

Table 4.3 Dimensions of coal fires in the Gulaben coalfield

Table 5.1 Description of three data sets

Table 6.1 Temperature (°C) for different depths at measuring points NE3 and NE6.

Table 6.2 ETM+ band 6 data used in the study

Table 6.3 Number of pixels for field coal fire areas and their thermal anomalies on night-time and daytime ETM+ images acquired in 2002. FN: Fire name number; F: Field coal fire distribution map; N: AnoNight2002; D: AnoDay2002; Ni: Pixels in both AnoNight2002 and FieldFire2002; No: Pixels in AnoNight2002 but FieldFire2002; T: Total.

Table 7.1 Pixel number of clusters for the interpreted thermal anomaly image in Wuda

List of Appendixes

Appendix 6.1 Ground Temperature Measurements of Coal Fire Experiment in DLR, Oberpfaffenhofen.

Appendix 6.2 Surface Temperature Measurements for a Sand Dune in Wuda Coal Mine Area, Inner Mongolia, China.

Appendix 6.3 Surface Temperature Measurements for A Coal Dump Pile in Wuda Coal Mine Area, Inner Mongolia, China. 23rd September 2002

Appendix 6.4 Surface Temperature Measurements for a Crack in Wuda Coal Mine Area, Inner Mongolia, China. 23rd September 2002.

Appendix 6.5 Statistical Characteristics of Thermal Anomalous Areas on ETM+ Night Image (28 September 2002).

Appendix 6.6 Statistical Characteristics of Thermal Anomalous Areas on ETM+ Day Image (21 September 2002).

List of Abbreviations

ABAS- Advanced BIRD airborne simulator

ASTER- Advanced Space-borne Thermal Emission and Reflectance Radiometer

ATSR- Along Track Scanning Radiometer

AVHRR- Advanced Very High Resolution Radiometer

BIRD- Bi-spectral InfraRed Detection

CCT- Computer Compatible Tape

DFD- German Remote Sensing Data Center

DLR- German Aerospace Center

ETM+- Enhanced Thematic Mapper Plus

GMT- Greenwich Mean Time

GPS- Global Positioning System

IR- Infrared

MIROR- Michelson Interferometer with Rotating Retroreflector

MODIS- Moderate Resolution Imaging Spectroradiometer

PCA- Principal Components Analysis

RXD- RX Detector

SAR- Synthetic Aperture Radar

TM- Thematic Mapper

Chapter 1 INTRODUCTION

Coal fires not only result from different causes (man-made, lightning strike, accident, forest fire or spontaneous combustion) worldwide, but also have a long history. In Xinjiang Uygur autonomous region (Xinjiang) of China, the paleo coal fires, caused by spontaneous combustion, were dated to be Pleistocene (de Boer et al. 1997, Schneider 1996, Zhang & Kroonenberg 1996). In New South Wales, Australia, the oldest known continuously burning fire, caused by lightning striking on a large coal seam at the surface, started over 2,000 years ago. Today this fire burns more than 152 meters underground, and is still slowly spreading in the coal seam. In Jharia, India, some of the subsurface coal fires, caused by mining introduced spontaneous combustion, have already been burning over five decades, and now they are still spreading (Mukherjee et al. 1991, Sinha 1989). In southwestern Pennsylvania, US, most of coal mine fires started about over 10 years ago by people burning trash in pits where the coal seam was close to the surface (Glover 1998). Forest fires ignite fires in surface outcrop deposits of coal. Coal fires continue to smolder underground after surface forest fires were extinguished, only to flare up again several months later, restarting forest and brush fires. This happened in Indonesia during each of the past three years. A conservative estimate based on actual field data suggests more than a quarter million tonnes coal and peat may be burnt out in Indonesia (Hamilton 2001).

Coal fires cause a lot of problems and are severe hazards (Feng et al. 1973, Guan et al. 1996). Coal fires produce harmful gases such as SO₂, NO, CO, CH₄ and ashes, which can be transported by wind and cause air pollution. Also problematic carbon monoxide gases and other toxic fumes can rise from the ground and seep into buildings, possibly asphyxiating people inside or causing long-term respiratory problems. In addition to the danger of the fire spreading to homes and wooded areas, subsidence can occur when the fire consumes the thick coal pillars left to help support the overburden in room-and-pillar mining (Chen 1997, Guan 1989, Rosema et al 1993). Subsidence can damage the infrastructure, such as roads and buildings. Some towns have been evacuated because of the danger of collapse as the underground coal seams slowly burn away. Coal fires not only burn out coal resources, particularly those that could be

easily exploited, but also lead to blockage and devaluation of coal resources in the seams below, above and around them. Forest related coal fires could destroy a large area of forest, including valuable reintroduction habitat for endangered species. Also coal fires contribute to the problem of global warming by producing a huge amount of CO₂. Their global warming potential is currently under evaluation.

In order to take effective mitigating actions, it is crucial to detect the coal fires, including the position, area, depth, the direction and the speed of fire movement, especially for those fires having burnt for a prolonged period of time, producing significant amounts of pollutants. Borehole measurements and geophysical methods, such as electrical and magnetic methods, have served for this purpose for quite a long time (Chen 1997). The shortcomings of these methods are that they are time consuming, difficult to repeat, and costly to apply over large areas; especially since many coal fires occur in isolated areas, high up in the mountains, in dense forests, and other inhospitable terrain. Hence the use of remote sensing techniques, particularly satellite remote sensing with a capability of repeated observation of the earth surface, was considered as a very suitable tool to detect, locate, analyse and monitor coal fires over a large areas.

1.1 Problem Identification

Since May 1963 when the first study for detecting coal fires over coal refuse piles using remote sensing techniques was undertaken in Scranton, Pennsylvania, US (Slavecki 1964), much work has been done in different countries and on different types of coal fires in the past 40 years. For example, within the framework of a Sino-Dutch project the coal fires of Ruqigou syncline in north-western Ningxia Hui Autonomous Region, China, were well studied (Prakash et al. 1999). Other coal fields investigated are the Jharia coalfield, India (Mukherjee et al. 1991), or the Pennsylvanian coal fires near Centralia (Chaiken et al. 1998) amongst others. However, all previous studies using space borne data were using GIS (with existing coal fire distribution maps) and undertook trial and error density slicing methods, which are only suitable for small and known areas (Chen, 1992; Reddy & Bhattacharya, 1995; Vekerdy & van Genderen, 1999; Vekerdy et al., 1999; Zhang et al., 1997a,b, 1998). So far, the detection of coal

fires using remote sensing techniques has not been applied in an operational fashion over large areas (Zhang et al. 2003). The main obstacles are:

- limitation of knowledge about the specific geo-spatial characteristics of coal fires; especially of underground coal fires;
- the need for a practical approach to demarcate coal fire areas from images over large areas

China is the biggest producer of coal in the world mining about 1000 Mt of raw coal per year and approximately 70% of Chinas energy consumption is covered by coal. According to the 10th five-year-plan (2001-05) of the State Economic and Trade Commission for the coal industry, coal will continue to be the major source of energy for China's industries in the next five years. Taking into account economic growth rates of 7-8% in the coming years, it is obvious, that coal is going to play an even more important role in Chinas economic development (Voigt et al. 2003). At the mean time it is estimated that about 10 Mt of coal are being burnt in coal fires in China each year (Guan & van Genderen 1997). Since the coal fires are spread out over the whole northwestern part of the country, especially in Xinjiang Uygur Autonomous Region, Inner Mongolia Autonomous Region, and Ningxia Hui Autonomous Region, it is extremely difficult to keep an overview of the development of known fires as well as of newly developing ones. In May of 2001 the German Remote Sensing Data Center (DFD) of the German Aerospace Center (DLR), launched a remote sensing project as the preparing phase for the current Sino-German joint project 'Innovative Technologies for Exploration, Extinction and Monitoring of Coal Fires in North China' that started in September of 2003. The main objective of the remote sensing project was to develop a methodology, based principally on the use of space remote sensing data, to detect, analyse and monitor the areas of coal fires in Northwest China, with an area of about 700,000km². Although nowadays satellite remote sensing offers a powerful tool to observe and monitor such large regions, special methods and techniques have to be derived.

1.2 Aim and Objectives

The aim of the research is to develop a practical approach for detecting coal fires in large areas using thermal satellite imagery.

The approach should be capable to automatically derive coal fire related information in order to become independent of manual techniques like trial and error thresholding or on screen digitization. It should be able to investigate unknown areas, not yet studied during past coal fire research, and to detect new coal fires. Furthermore, the approach should be transferable to different scenes of images, to become really operational. Within the DLR-DFD remote sensing project, this approach was composed of three parts. One is the classification of the satellite multi-band data to derive landcover maps and locate the favorite coal fire occurrence areas, such as areas close to the outcrop of coal seams, as well as non-coal fire areas, such as water bodies, industrial areas, etc. The second is the extraction of coal fire related thermal anomalies using the thermal bands to directly locate the position of coal fires, which should be based on a good understanding of the thermal characteristics of coal fires and their background. The last part is the quantification of the coal fires detected. This thesis is concentrated on the extraction of thermal anomalies related to coal fires.

To achieve this aim, two objectives are defined:

Objective 1 Analysis of thermal characteristics for coal fires and their background;

Objective 2 Development of a practical approach for the extraction of coal fire related thermal anomalies in a large area.

1.3 Methodology

1.3.1 Reference analyses

All the possible references have been collected for the understanding coal fires and their related surface features, and were reviewed with respect to the detection of coal fires using remote sensing techniques. Landsat-7 ETM+ band 6 data were chosen as the main data source for extracting coal fire related thermal anomalies due to the

improvement of Landsat-7's detection capability compared to former Landsat sensors. Material about the geography, geology, coal geology, and coal fires was acquired for obtaining an overview of the study areas. Three study areas, named Wuda, Ruqigou and Gulaben, located in the border area between the Inner Mongolia Autonomous Region and the Ningxia Hui Autonomous Region were defined.

1.3.2 Field work

Two field work campaigns have been conducted in September 2002 and September 2003. In the field work 2002, the surface temperatures of coal fires and their backgrounds were measured by using contact and radiant thermometers. Detailed distribution maps of coal fires in the study areas were generated with the help of Global Positioning System (GPS) instruments for navigation. In the field work 2003, thermal anomalous pixels extracted by the algorithm developed were validated. A new coal fire area with previously unknown coal fires, outside the three study areas could be detected. This confirmed the validity and suitability of the developed approach.

1.3.3 Algorithm development and validation

Based on the analysis of thermal characteristics for simulated coal fires and field coal fires in the study areas, a practical algorithm for the extraction of coal fire related thermal anomalies from the images was developed. The characteristics of coal fires on different images were studied, which could be used for fine-tuning the results from the algorithm. To assess the transferability of the algorithm, coal fires in another scene covering an area in Xinjiang Autonomous Region, about 2000 km away from the three study areas, were detected. The detection capability of new coal fires in previously not studied areas was evaluated.

1.4 Outline of the Thesis

The thesis is organized in the following way. After the introduction, Chapter 2 discusses coal fires, their causes and classification, rocks and minerals produced by coal fires, coal fire generated geomorphology, and surface temperature related to coal fires. This chapter gives an overview of coal fires and their related surface features, which are the base for the coal fire detection using visible and near infrared bands of

remote sensing data. Chapter 3 reviews the previous work on detection of coal fires using different sensors in different areas, with emphasise on the cases using thermal remote sensing imagery. Chapter 4 describes general information in the study areas, especially coal fire information, and the data sets. Chapter 5 states basic concepts on thermal remote sensing. The theory on detecting a sub-pixel coal fire is discussed as well. In Chapter 6, thermal characteristics of coal fires are studied. Coal fires include two simulated coal fires in the experimental scale, and coal fires in the real scale in the study areas. The statistical characteristics of the known coal fires on different images are also studied. These thermal and statistical characteristics of the known coal fires are the basis of developing a suitable algorithm for extracting coal fire related thermal anomalies. In Chapter 7, the algorithm for the extraction of coal fire related thermal anomalies is developed. In the next Chapter 8, the algorithm is applied to the study areas, and an area two thousand kilometres away from the study areas. Results are assessed and validated. It is confirmed that unknown coal fires in a previous non-studied area can be detected by the algorithm. Finally, conclusions and outlook are given in Chapter 9.

Chapter 2 COAL FIRE AND ITS RELATED SURFACE FEATURES

2.1 Coal Fires, Their Causes and Classification

In the thesis, a coal fire is defined as combustion of coal in a coal seam (or a pile of stored or waste coal), which has a potential to burn for a long time by spreading along both directions of the strike and dip of the coal seam (or within the pile). Coal fires can be ignited in different ways, by forest fires (Bustin & Mathews 1982, 1985), coal mining accidents, careless handling fires on the coal seam outcrop, lightning strike (Guan et al. 1996) or spontaneous combustion of coal. Spontaneous combustion of coal occurs due to the accumulation of heat generated during the interaction of oxygen with coal, and poor thermal conductivity favoring heat accumulation. This interaction with oxygen is mainly due to the oxidation of carbonaceous matter in coal. The other factors that might also assist in the generation of heat are due to the oxidation of pyrite present in coal and absorption of water vapor in coal. Heating due to bacterial activity or from earth movement are possible causes, however, these are of no practical importance. Coal rank, coal type, geomorphologic setting, geological conditions, geographic conditions, hydrological conditions, and human interactions are important factors for spontaneous combustion of coal (Banerjee et al. 1970, 1972, Banerjee 1982, 1985, Gijbels & Bruining 1982, Schmal 1987, Zhang & Tang 1994).

Coal fires have been classified into different types by different researchers (Guan & van Genderen 1997, van Genderen & Guan 1997, Yang 1995, Zhang 1998). Yang (1995) indicated that spontaneous combustion of coal could be divided into the following groups: surface and subsurface according to the depth of combustion; paleo and recent according to the starting time of a coal fire; extinct, dormant and active according to burning state of a coal fire; and also coal field fire, coal mine fire and stock pile fire upon where the coal fires got started. van Genderen & Guan (1997) described the coal fires as underground and surface coal fires. They also mentioned that combustion could occur either within the coal seams themselves or in piles of stored or waste coal on the surface. Guan & van Genderen (1997) classified the coal fires into three first categories: coal field fire, coal mine related fire, coal waste or stock fire. And these three first categories could be classified into several second

categories. In 1998, Zhang classified coal fires into four groups: underground mine fire, coal seam fire (coal field fire), coal refuse fire, and coal-stack fire. There are no arguments on the “coal refuse fire, and coal-stack fire”, however for the “coal mine (related) fire” and “coal field fire”, even the same term has different meanings when used by different people.

Based on the general understanding, the following coal fire classification was derived and recommended (Table 2.1). Coal fires, firstly, upon the position of coal, can be classified into two types: coal seam fire (coal is in-situ) and coal heap fire (coal is non-in-situ). Secondly, the coal seam fire can be classified in to coal mine fire (mining related) and nature coal fire (not related to the mining). While coal heap fire includes coal waste and stockpile fire. Thirdly, each coal fire type can be divided into the following classes by their attributes: surface (fire is burning on the surface of the earth) and underground or subsurface (fire is burning in subsurface); paleo (fire was burning in the paleo-time) and recent (fire was burning in recent time); extinct (now fire is extinct, incapable of further burning), dormant (fire is not spreading, but probably capable of re-burning) and active (fire is burning and spreading).

First class	Second class	Attributes
Coal seam fire	Nature coal fire	Surface/Underground or Subsurface Paleo/Recent
	Coal mine fire	
Coal heap fire	Coal waste fire	Extinct/Dormant /Active
	Coal stockpile fire	

Table 2.1 The classification of coal fires

2.2 Rocks and Minerals Produced By Coal Fires: Pyro-Metamorphic Rocks and Fumarolic Minerals

In coal fire areas, coal fire related products like ash, pyro-metamorphic rocks and fumarolic minerals can be found on the surface.

When coal burns away, it becomes ash. Normally a coal seam with a thickness of 20 meters thickness can leave an ash layer with a thickness of 15-20 cm, which shows a pink or light pink color, and can only be seen on the outcrop (Zhang 1996).

Pyro-metamorphic rocks, also called burnt rocks, are the rocks metamorphosed by the heat coming from the adjacent combustion of the coal seams. According to the thermal metamorphosed degree depending upon the distance from the combustion of the coal seam and the degree of the accumulation of heat, pyro-metamorphic rocks can be further divided into three types (Guan 1963, Zhang et al. 1996): baked rock, porcelanite, and molten rock. Baked rock (See Figure 2.1, A) is a kind of pyro-metamorphic rock that is formed after the original rock baked under a relative low temperature (340-800°C). The baked rock still keeps its original texture, but changed its color because of dehydration and oxidation. Porcelanite (See Figure 2.1, B) is a kind of pyro-metamorphic rock that is formed after the original rock heated under a medium temperature (600-1400°C). The rock became very hard and formed ceramic texture. The color of the original rock has been greatly changed. Molten rock (See Figure 2.1, C) is a kind of pyro-metamorphic rock that is formed after the original rock heated under a high temperature (1500-2000°C), commonly distributed in burnt center or near coal seams. The granulated minerals in the rocks smelted to form a kind of black lava.

The original rocks commonly have dark color and moisture content. When a rock is heated by a coal fire at the temperature of 340-800°C, the rock experiences dehydration and oxidation. Dehydration affects the different types of H₂O components in the rock at different temperature. That is, free water (45-200°C), bound water (>100°C), and constitutional water (500-700°C). Oxidation changes gray, green color rocks to yellow, orange, red or brown color rocks. All organic materials become gases after the temperature reaches 350-500°C. At the first phase of this stage, rocks are becoming dry and turn into yellow color. At the second phase, with the increasing amount of heat received by the rock the rock becomes purple, brick red or brown. With increasing temperature, the rock will eventually be molten (1500-2000°C), or first turns to porcelanite (600-1400°C), depending upon the mineral contents in the rock, whether favorable to form porcelanite or not. From the microscope observation, it is known that in this stage iron mineral has already re-concentrated and the color change is most likely due to hematite (de Boer et al. 1997).

The distribution of the pyro-metamorphic rocks is dependent on the scale of the coal fires. In Xinjiang, China, normally it extends over a large area of about 0.1-1 ha but sometimes it can extend over distances of kilometers in the case of paleo coal fires.

Fumarolic minerals are newly generated minerals by the coal fires. The minerals in the original formation were dissociated by the heat caused by coal fires and transferred along the cracks to the surface, where they re-crystallized due to the drop of the temperature and the pressure. The newly generated minerals are generally sulfur (S), gypsum ($\text{CaSO}_4 \cdot \text{H}_2\text{O}$), calcite (CaCO_3), salmiac (NH_4Cl) (See Figure 2.2) (Zhang, 1996), tschermigite ($(\text{NH}_4)\text{Al}(\text{SO}_4)_2 \cdot 12(\text{H}_2\text{O})$), and apjohnite ($\text{MnAl}(\text{SO}_4)_4 \cdot 22\text{H}_2\text{O}$) (Livingood 1999).

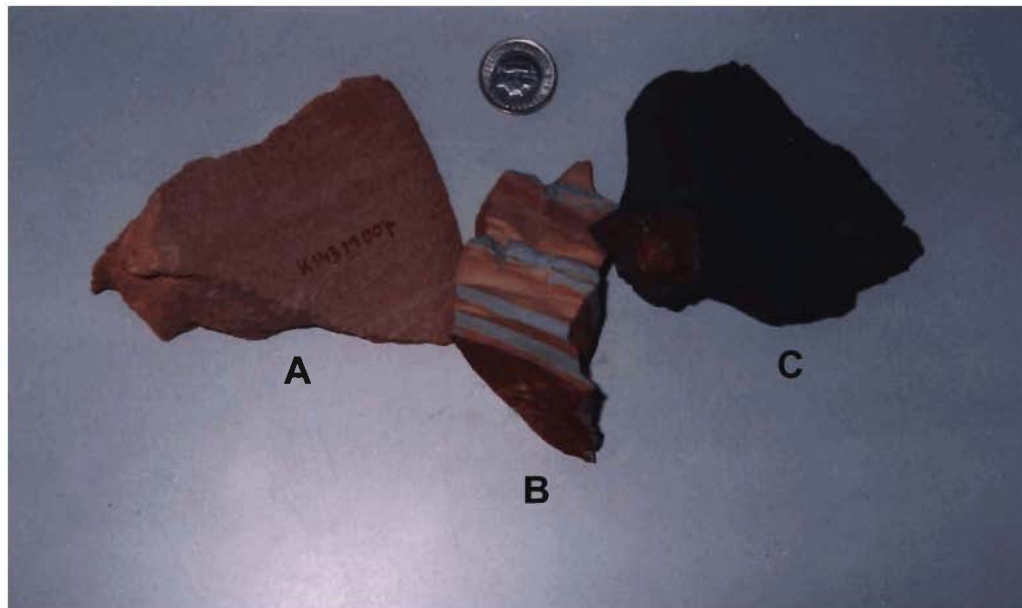


Figure 2.1 Photograph of pyro-metamorphic rocks. **A:** Baked rock; **B:** Porcelanite; **C:** Molten rock. Specimens are from Xinjiang, China.



Figure 2.2 Field photograph of fumarolic mineral (Salmiac) in Xinjiang, China.

In Centralia, U.S.A., vents and fissures are scattered all throughout relieving the increased underground pressure caused by the fires. Sulfuric steam and smoke rise from these vents and tschermigite and apjohnite deposits are found surrounding the fissures. Apjohnite is found as a crust, which coats the entire vent structure and is white with a slightly vesicular appearance. Apjohnite is deposited through precipitation from condensing steam that distributes the mineral as a coating over the vent. Tschermigite deposits are found as blocky masses right at the vent openings suggesting hydrothermal deposition from heated groundwater. Apjohnite usually is white to pale yellow, has a hardness of 1.5 to 2, and has encrustation (forms crust-like aggregate on matrices) habit. Tschermigite, also known as ammonia alum, is soft (hardness = 1.5-2.0) and is usually white to colorless (Barthelmy 1999a,b). Tschermigite is very rare and only found natively in Czechoslovakia, but also has been reported to form as deposits around volcanic vents and fumaroles and other “hot spot” areas (Livingood 1999, Lowenstern 1999). In Xinjiang, China, yellow sulfur, or greenish yellow, stable below 96°C, is a very common mineral existing in the crevasse area as affected by coal fires. It is frequently associated with salmiac, gypsum and

calcite. The spatial distribution of the fumarolic minerals is several ten meters by several ten meters, sparsely distributed around the mouths of the smokers of the coal fires (Zhang 1996).

2.3 Coal Fire Generated Geomorphology: Burnt Pits and Trenches, Subsidence and Cracks (Fractures)

When a coal fire occurs at the outcrop of a coal seam with a large dip angle, after the coal has burnt, a burnt pit forms. Figure 2.3 shows a burnt pit in Xinjiang, China. It has a diameter of 10 meters, a depth of 10 meters, and at the bottom, the coal is burning. The fire will spread along the strike direction and dip direction at a speed of approximately 1-4 m per year. After a long time, all the shallow coals will be burnt out and on the surface, a burnt trench will be left. Around a burnt pit and trench, the burnt rocks are well developed. Figure 2.4 depicts a burnt trench in Xinjiang, China, with a 20 meter width and a 4 km length.

When a coal fire occurs in the outcrop of a coal seam with a gentle dip angle, after the burning of a coal seam or several coal seams, the cap rock collapses, resulting in land slides and cracks as shown in Figure 2.5. The cracks are typically 50-500 meters long and 0.1 to 1 meter wide. The longest cracks extend to over 1 km, and widest cracking measured in the field in Xinjiang, China was 2.5 meters. The cracks are perpendicular to the spreading direction of the underground coal fire.

With the burning of the underground coal seams, coal voids may be formed which could result in surface subsidence. The subsidence induced from coal fires is commonly restricted to large coal fire areas. Usually, its displacements are very small in dimension and mostly invisible from morphological features on the aerial photographs. Sometimes, rather large subsidence can be formed at coal mining area due to the burning of the coal pillars. This could be the combined effect of coal fires and coal mining.



Figure 2.3 Field photograph of a typical burnt pit in Xinjiang, China.



Figure 2.4 Field photograph of a typical burnt trench in Xinjiang, China



Figure 2.5 Field photograph of typical cracks in Xinjiang, China. The width of the cracks ranges between 0.1 to 1 meter.

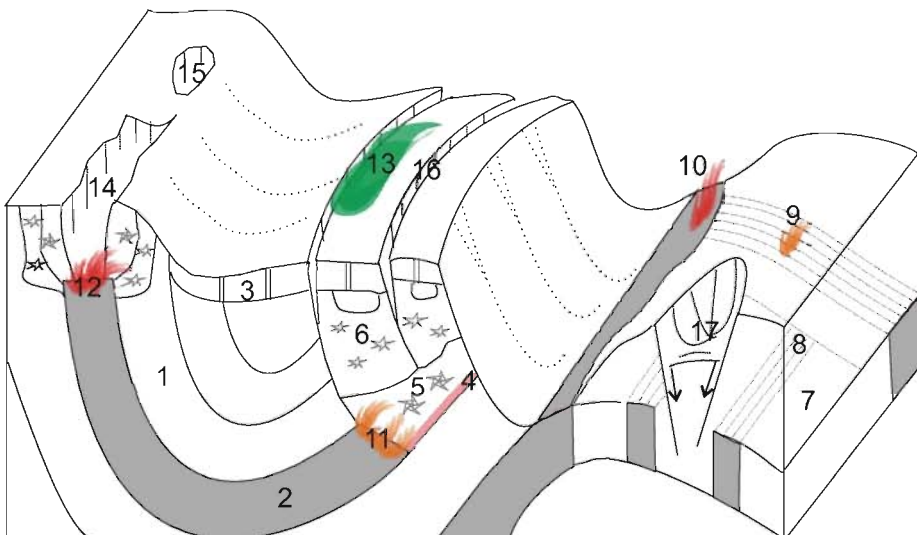


Figure 2.6 A diagram of coal fires and their related features. 1: Original rock; 2: Coal seam; 3: Soil; 4: Ash; 5: Molten rock; 6: Baked rock; 7: Coal mine area; 8: Pillar; 9: Underground coal mine fire; 10: Surface coal mine fire; 11: Underground nature fire; 12: Surface nature fire; 13: Fumarolic mineral; 14: Burnt trench; 15: Burnt pit; 16: Crack; 17: Subsidence.

In Australia, extensive fracturing and subsidence is associated with the fire. The subsidence of strata is thought to be caused by a reduction in volume of the burning coal seam. The orientation of fractures associated with the subsidence appears to be controlled by preexisting planes of weakness which correspond to longitudinal joints and one plane of a conjugate set of diagonal joints. These fractures are approximately a meter in length and a few centimeters wide. A chimney formed by these fractures, named 'Burning Mountain', with an area approximately 400 m², is moving south along a ridge, presumably corresponding to a fire slowly consuming a seam of coal. During the last 120 years it appears that the chimney has moved about 80 m (Mitchell 1839, Abbott 1918). Another chimney, named 'little Burning Mountain', formed by a rectangular fracture approximately 2 m², appears to be stationery and it has not moved since it was first observed by Abbott in 1852 (Abbott 1918).

Figure 2.6 depicts the general overview of coal fires and the related surface features.

2.4 Surface Temperature Related To the Coal Fires

Coal fires create higher temperatures on the earth's surface than the background. For the surface coal fires, they have much higher temperatures (normally higher than 400°C) than the background. For the underground coal fires, the temperature difference between the fire anomalies and the background is much more subtle and varies with location, observaton time, weather, etc.

Surface temperatures were measured in the coal fire areas in Xinjiang, China, by using a portable infrared thermometer in 1994 and 1995 (Zhang 1998). The distance between the measurements was 5 meters and in total about 700 temperature measurements were taken. On the bases of field observations and surface temperature measurements, the thermal anomalies above the underground coal fire (with depth of 50-150meters) areas were classified into three groups (See Figure 2.7): 1) low-amplitude thermal anomalies: they have surface temperatures of up to 20°C higher than the background. On the surface there are no significant changes in texture and color. 2) medium-amplitude thermal anomalies: they are usually 20°C to 120°C above the background temperature. There are haloes of sulfur crystals, micro-cracks on the surface. 3) high-amplitude thermal anomalies: they have temperatures of about 120°C to over 300°C

above the background temperature. There are salmiac deposits, molten rocks, and big cracks on the surface. The highest temperatures were typically located at hill tops over active coal fires, apparently because the higher topographic elevation ensures a longer chimney system to supply the fire with oxygen. The width of individual high-amplitude thermal anomalies usually does not exceed a few meters from the hot source or vent. Among the three thermal anomalies, low-amplitude thermal anomalies have the largest occurrence (Zhang 1998). Temperature measurements at a fracture in the Burning Mountain chimney, Australia, through which hot fumes are escaping, showed a horizontal gradient in damp soil of 3.8°C per cm (Ellyett & Fleming 1974).

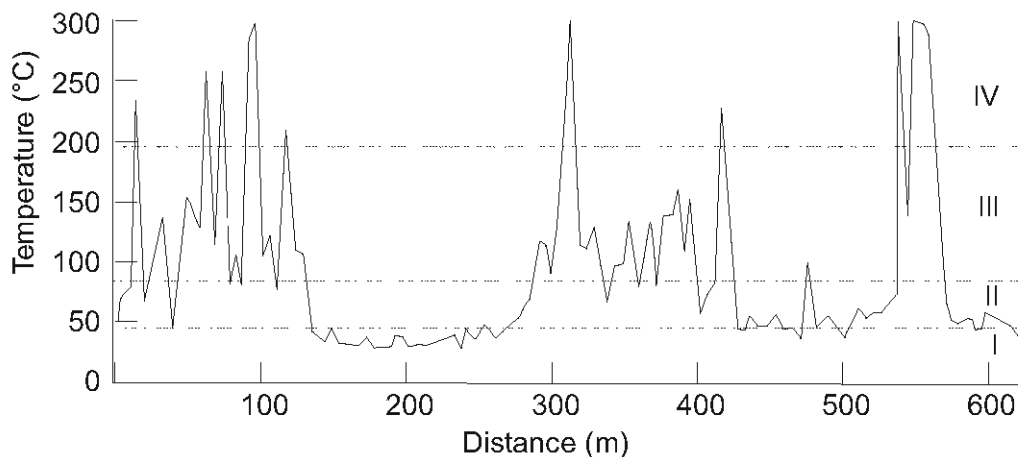


Figure 2.7 Field along-strike measurement of temperature profile of coal fire No. 141, 142 and 143 in Xinjiang, China (measured at noon time of 17 August 1995). I: Background temperature; II: Low-amplitude thermal anomalies; III: Medium-amplitude thermal anomalies; IV: High-amplitude thermal anomalies (After Zhang 1998).

In the Mukunda area, Jharia coal field, India, thermal profiles of digitally recorded temperature data along scan lines by using an AADS 1268 Daedalus Multi-spectral Scanner System in February and March of 1989 were studied across a known geologic section in order to correlate them with anomalous temperatures associated with the fires. One typical temperature profile, along with the section of fire-affected coal seams, is shown in Figure 2.8. The temperature profile depicts distinct anomalous zones with respect to the background temperature. The average ambient temperature is about 12°C. The fluctuations along the profile seem to be due to variations in temperature associated with the inhomogeneity of the top soil and sand stone. There

may also be minor cracks. The background noise is thus separated by graphical smoothing for the calculation of the duration of the fire or the depth of the fire. Temperature anomalies of a magnitude of about 68°C along the profile at about 200m and 400m appear to correspond to fires in the IX/X and VIIIA coal seam at depths of about 45m and 40m, respectively. The age of the fire associated with the IX/X seam is computed to be about 8 years and that with the VIIIA seam to be about 7 years. The anomalies towards the extreme right of the profile seem to be from the fire in the workings of the VIII seam (Mukherjee et al. 1991). Gupta & Prakash (1998) showed a field temperature profile of an area with subsurface fires in the same coal field (Figure 2.9). The background temperature was lower than 24°C, and the highest anomalous ground temperatures were about 28°C in this profile.

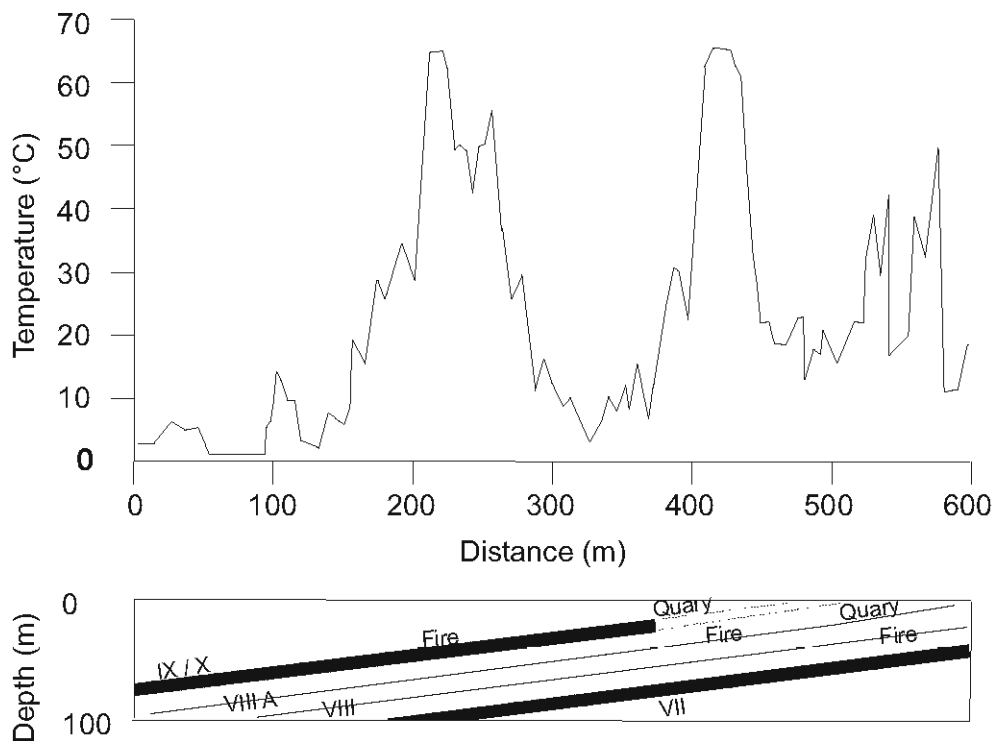


Figure 2.8 A thermal profile over burning coal seams in Jharia coal field, India (After Mukherjee et al. 1991).

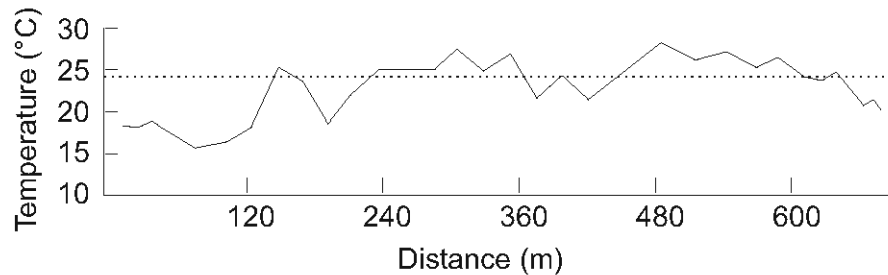


Figure 2.9 A profile of surface temperature (field measurements) above subsurface fires in Jharia coal field, India. The background temperatures are lower than 24°C (After Gupta & Prakash 1998).

2.5 Conclusion

In brief, coal fires, defined as combustion of coal seams and piles having a potential to burn for a long time, occur all around the world. They cause a lot of problems to people and to the environment. Coal fires can ignite in different ways and can be classified in different types. They change the cap-rocks to pyro-metaphoric rocks and generate fumarolic minerals on the surface. Smoke, burnt pits and trench, subsidence and cracks, surface thermal anomalies can be generated by coal fires, too. These surface features can be used as indicators for coal fires detection by using remote sensing techniques (Zhang et al. 1995). Coal fire detection includes isolating coal fires areas, locating the front of coal fires, calculating the depth and ages of coal fires. Smoke, fumarolic minerals, and thermal anomalies are direct indicators for active coal fires. Pyro-metaphoric rocks and burnt pits and trenches are good indicators for paleo-coal fires and can also be helpful to detect active coal fires. Land subsidence can be also used for coal fire zonation detection.

Chapter 3 STATE OF THE ART

3.1 Detecting Surface Features of Coal Fires Using Remote Sensing

Coal fires cause not only an increase in temperature, but also a series of other surface features, which include: emission of smoke, new generated fumarolic minerals and pyro-metamorphic rocks, burnt pits and trenches, subsidence and cracks (fractures). These surface features can be used by the various remote sensing platforms and sensors as indicators for detecting coal fires.

3.1.1 Visible and near infrared remote sensing

There are many airborne and space borne remote sensing systems operating in the visible and near infrared regions of the electromagnetic spectrum. Landsat TM and ETM+ provide four 30 meters spatial resolution bands (Band 1: 0.450-0.515 μm , Band 2: 0.525-0.605 μm , Band 3: 0.630-0.690 μm and Band 4: 0.750-0.900 μm) in a sensitivity range of the visible and near infrared spectral region. SPOT XS has three bands with 20 meters spatial resolution in this spectral region. ASTER provides three bands (Band 1: 0.52-0.60 μm , Band 2: 0.63-0.69 μm and Band 3: 0.76-0.86 μm) with a spatial resolution of 15 meters. These bands, with suitable processing techniques, can be used to isolate the pyro-metamorphic rocks from the original rocks according to their spectral difference. Figure 3.1 depicts the average reflectance of the pyro-metamorphic rocks and the original rocks in the wavelength of 0.5-0.6 μm , 0.6-0.7 μm , 0.7-0.8 μm and 0.8-1.1 μm in Shaanxi and Xinjiang, China, respectively (Based on the field measurements by Guan & van Genderen 1997). It can be seen that the average reflectance difference between the pyro-metamorphic rocks and the original rocks has the maximum value of 8.4 % (in Shaanxi) and 7.3 % (in Xinjiang) at the wavelength of 0.5-0.6 μm , and it declines with the increase of the wavelength, at the wavelength of 0.8-1.1 it reaches the minimum value of 4.4 % (in Xinjiang) and -1.0 % (in Shaanxi).

In the enthusiasm for satellite images and new forms of airborne remote sensing, one should not overlook the advantages of aerial photographs (Goetz & Rowan 1981, Sabins 1996). Color-infrared aerial photographs also provide a sensitivity range of visible and near infrared spectral region. Yang et al. (1996) mentioned that the smoke

and the long parallel cracks caused by the coal fires can be clearly observed on a color-infrared aerial photograph with the scale of 1:10,000 in Xinjiang, China. With their unique spectral reflectance, pyro-metamorphic rocks showed the distinctive color of yellowish orange. Furthermore, with the stereo photograph pairs, the geological structures and the coal seam outcrops were interpreted and mapped. Chen (1997) conducted mapping subsidence introduced by coal mining and coal fires using color infrared aerial photographs of scale 1:10,000 in Ningxia, China. Subsidence had two pronounced characteristics, which were scarps and cracks. The formation of scarps made it easy to delineate the subsidence areas from aerial photos. However, in most cases the subsidence areas were lacking scarps. For this case, the subsidence could only be inferred from the occurrence of cracks and other features. Unlike space borne remote sensing, aerial photography has a limitation of relatively expensive acquisition on a regular base for monitoring purposes, especially for a large area. Also, the large number of photographs needed for interpretation is a drawback.

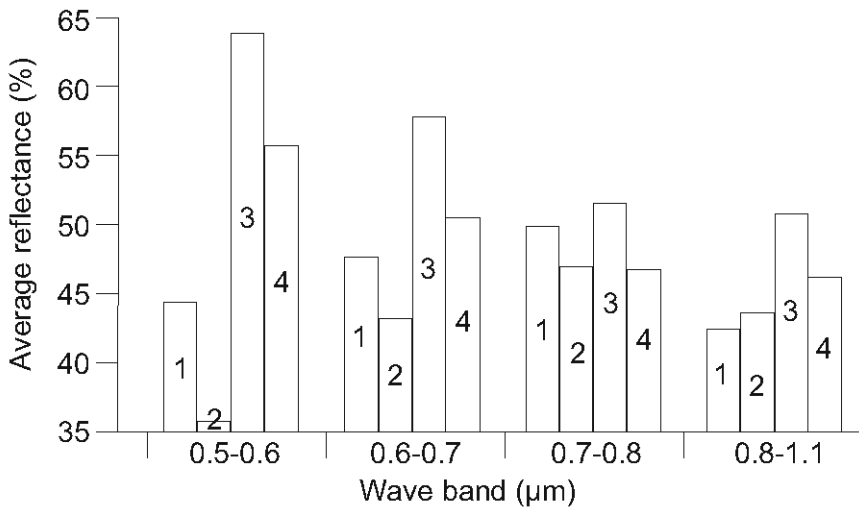


Figure 3.1 Average reflectance of original rocks and pyro-metamorphic rocks in the wavelength of 0.5-0.6μm, 0.6-0.7μm, 0.7-0.8μm and 0.8-1.1μm in Shaanxi and Xinjiang, China, respectively. 1: Original rocks in Shaanxi, China; 2: Pyro-metamorphic rocks in Shaanxi, China; 3: Original rocks in Xinjiang, China; 4: Pyro-metamorphic rocks in Xinjiang China (Data from Guan & van Genderen 1997).

3.1.2 Short-wave infrared remote sensing

In the short-wave infrared region (1.3-2.5 μm), the spectral features of rocks are mainly due to the vibrational process of water molecules (H_2O), hydroxyl (OH^-), and carbonate (CO_3^{2-}) (Charles 1987, Hunt et al. 1970, 1971a,b, 1972, 1973 a,b,c, 1974, 1975, 1976 a,b, 1977, van der Meer 1995). This makes it difficult to distinguish different original rocks, but it does make it easy to distinguish the pyro-metamorphic rocks from the original rocks, because the pyro-metamorphic process itself is a process of dehydration and oxidation. Zhang (1996) measured the spectra of rocks in the wavelength of 1.3-2.5 μm in coal fire areas, Xinjiang China. The original sedimentary rocks (sandstone, siltstone, mudstone and gray shale) commonly with dark color and moisture content showed the same spectral absorption features at the wavelengths near 1.410, 1.910, 2.125, 2.210, 2.350, 2.380 and 2.500 μm (Figure 3.2, 1). Their low total reflectance (4-28%) was due to the moisture and black organic material remnants influence. When rocks were heated by a coal fire, rocks became baked rocks. They were dry and turn into yellow color. Their spectra showed 3 strong absorption bands near 1.419, 1.900 and 2.190 μm and a increasing reflectance up to 70%. Their spectral features were dominated by the free water molecules (Figure 3.2, 2), or water molecules existed in the lattice (Figure 3.2, 3). With the increasing amount of heat received, the baked rocks became purple, brick red or brown. Their total spectral reflectance decreases. Two clear absorption bands near 1.906 and 1.410 μm (Figure 3.3, 4) were caused by constitutional water molecules. With the increasing temperature, the rocks eventually became porcelanite or molten rocks. Porcelanite and molten rocks show no absorption bands as the constitutional water molecules gradually disappeared. Their overall reflectance decreased up to 4% (Figure 3.3, 5 and 6).

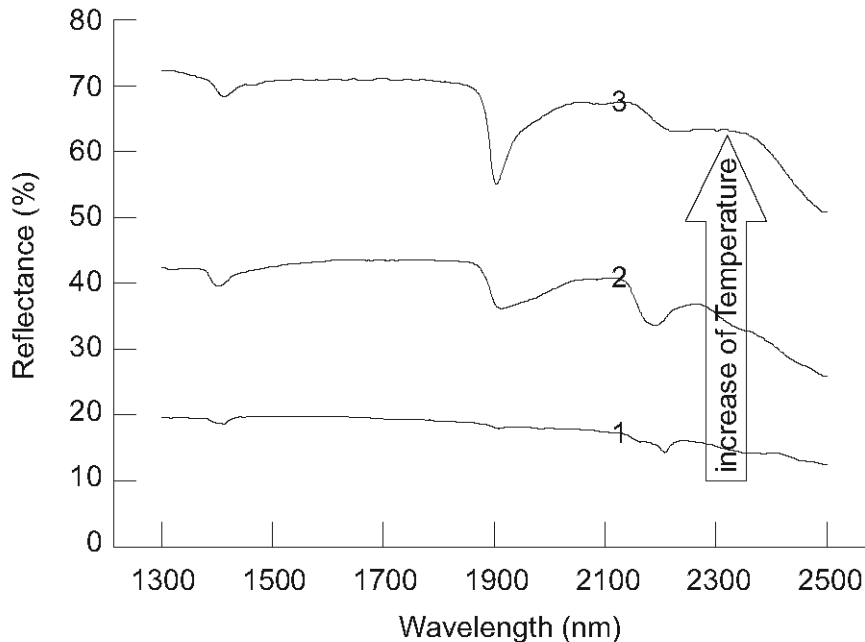


Figure 3.2: Spectra of pyro-metamorphic rocks. 1: Dark gray siltstone with black organic material remnants; 2: Yellowish gray slightly baked siltstone; 3: Light yellow baked siltstone. From a original rock to a baked rock, the reflectance increases with the temperature (After Zhang 1996).

Every fumarolic mineral has its own distinctive spectral features in short-wave infrared spectral region. Sulfur and gypsum are stable under the temperature of 100°C. They could be the indicators of underground active coal fires. Salmiac in the coal fire fields most of the time exists at the surface when the temperature was above 100°C. It could be the indicator for surface coal fires. Through these fumarolic mineral indicators, Zhang (1996) successfully distinguished the active surface coal fires and underground coal fires in Xinjiang, China using airborne short-wave infrared data with 8 bands (1.550-1.650 μm , 2.062-2.137 μm , 2.093-2.193 μm , 2.150-2.250 μm , 2.220-2.275 μm , 2.275-2.325 μm , 2.303-2.355 μm , 2.400-2.500 μm).

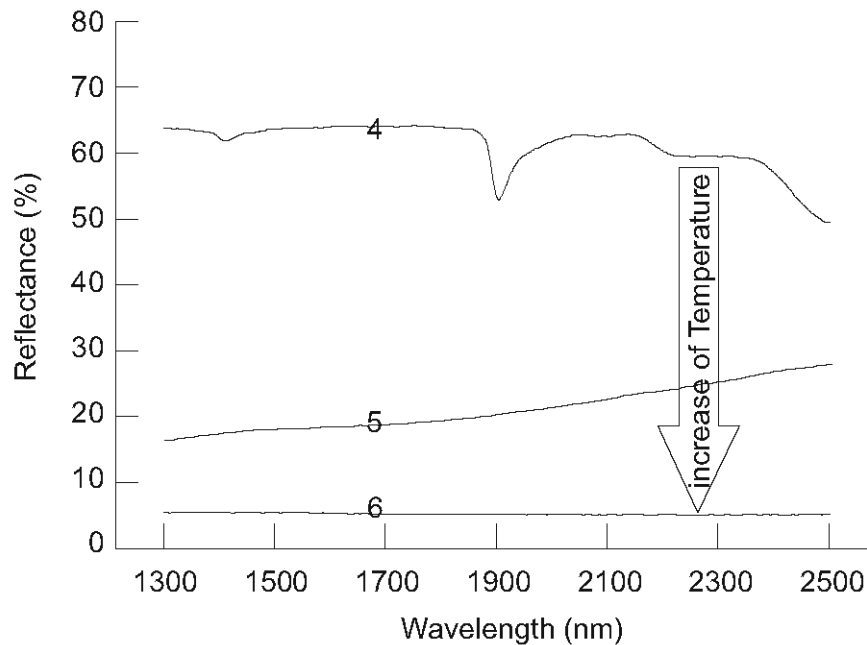


Figure 3.3: Spectra of pyro-metamorphic rocks. 4: Yellowish brown burnt siltstone with black molten spots; 5: Black molten siltstone; 6: Black molten rock with vesicles. From a heavily backed rock to a molten rock, the reflectance decreases with the temperature increases (After Zhang 1996).

3.1.3 Radar remote sensing

The European Space Agency’s ERS-1 and ERS-2 satellites have on board a Synthetic Aperture Radar (SAR) sensor operating in the C band with a spatial resolution of approximately 25 meters. These two satellites were flown in a so-called ‘Tandem’ mode with one-day interval between data acquisitions. By using SAR interferometric techniques, a DEM can be produced, which will be helpful to reduce the solar affects in optical imagery. Using differential interferometry, very small vertical land subsidence movements (in the order of centimeters) can be accurately measured (Gabriel et al. 1989, Gens & van Genderen 1996). Prakash et al. (2001) tried to use SAR interferometric techniques to detect coal fire introduced land subsidence in Ningxia, China. One limitation to use land subsidence to locate coal fire areas is that the coal fire is not the only source to induce the subsidence. Underground coal mining

and some geological movements can induce subsidence, too. Chen (1997) mentioned that the subsidence resulting from underground coal mining was usually large and easy to detect from the morphological features. However, the subsidence resulting from underground coal fire was usually small and difficult to detect from remote sensing imagery. Even though some subsidence is not directly related to a coal fire but only coal mining (room and pillar method), it can be still used in zonation of coal fire prone area detection. Because the subsidence can make the underground coal, such as the pillars left after coal extraction, exposed to air by fracturing, it is vulnerable to initiate a new coal fire. Furthermore the subsidence could directly bring current coal fires to a new place or help the coal fires to expand by air ventilation through cracks.

3.2 Detecting Thermal Anomalies of Coal Fires Using Thermal Remote Sensing

3.2.1 Airborne thermal remote sensing

3.2.1.1 The first case study of detecting coal fires using thermal imagery

The first documented study for detecting coal fires by using remote sensing techniques was carried out in May 1963, when HRB-Singer Inc. was invited to test the feasibility of detecting and locating coal fires over coal refuse piles at Scranton, Pennsylvania, U.S. with its thermal camera RECONOFAX Infrared Reconnaissance System (Slavecki 1964). Visual interpretation of the thermal infrared imagery showed refuse piles under fire as 'hot' light toned areas. These hot areas were also correlated with ground photos where areas of red ash typically represented surface burning. At two locations 'hot' light toned areas on the aerial photographs had no corresponding red-ash on ground photos. It was concluded in this case that fires were in fact burning but had not reached the surface of coal refuse piles.

3.2.1.2 Isolating coal fires using daytime and night-time thermal data

Greene et al. (1968, 1969) conducted aerial infrared surveys of twenty-two coal mine fires in the anthracite field of Pennsylvania and in the field near Pittsburgh, U.S. Aerial infrared data in the 8-13 μm range was used in this study. This data was collected just before dawn since a maximum thermal contrast between fire areas and their surroundings is expected at this time. In addition to this, thermal infrared imagery was

also acquired during the daytime as surface temperature measurements suggested that the intensity of the underground fires at certain locations would make their detection possible on daytime imagery as well. This study brings out some interesting points in terms of isolation of fires from other areas on daytime and night-time (or pre-dawn) thermal imagery (Rathore & Wright 1993).

Although thermal anomalies caused by mine fires were detectable on both imageries, areas of bare rock outcrops, which are hot during the daytime, appeared warm on the daytime imagery creating confusion with areas of underground fires. In contrast, water bodies appeared warm on the night-time imagery and created a similar confusion with mine fires. The twenty-two underground fires considered in this study were categorized in relation to the depth at which they were burning (shallow, intermediate or deep). The categories included shallow fires, where the burning coal was within 10 meters of the surface, intermediate fires where the burning coal was between 10-30 meters and deep fires where the burning coal was at a depth greater than 30 meters. It was found that shallow fires could easily and successfully be detected on the thermal infrared imagery. Intermediate fires were detected where heat was carried to the surface through open cracks, fractures or bore holes by convection or by conduction through the overburden material at those places where fires were burning for a very long time. Deep fires were detectable only at places where heat was transferred by convection through fractures or cracks as it would take a considerably longer time (somewhere around 10 years) for conductive heat to manifest at the surface from depths greater than 30 meters. This study also calculated the age of a deep mine fire using the equation of linear heat flow in a semi-infinite medium.

Some other examples of the use of airborne thermal infrared data to locate coal fires around the 1970s include Moxham & Greene (1967), Knuth et al. (1968), Fisher & Knuth (1968), Rabchevsky (1972), Ellyett & Fleming (1974).

3.2.1.3 Detecting coal fires using multi-spectral thermal remote sensing

Since the 1980s, China and India, both suffering greatly from coal fire problems, started airborne multi-spectral remote sensing investigations on coal fires. In China during 1982-1986, Multi-spectral scanner data, dual band thermal infrared scanner data

(3-5 μm and 8-12.5 μm), and color infrared aerial photographs were used for detecting coal fires in Taiyuan Xishan, Shanxi (Guan 1984, Li 1985), Ruqigou, Ningxia (Huang et al. 1991), Shenfu, Shaanxi (Feng 1990, Kang 1991), respectively. In cooperation with Russia, India started using airborne multi-spectral data for coal fire mapping in the Jharia coal field during 1984-1987 (Bhattacharya et al. 1991, 1994, Bhattacharya & Reddy 1994, Mansor et al. 1994, Mukherjee 1991, Prakash et al. 1995a, b).

Zhang (1998) conducted a study on detection of coal fires in Kelazha, Xinjiang, China, in an anticline of 8 km long and 2 km wide. There three middle Jurassic coal seam layers, with a thickness of 20m, 6m, and 2m, respectively, were suffering spontaneous combustion. Hangding-40 Airborne Multi-spectral Scanner data, acquired at daytime and night-time in July-August 1992, were used in the study. The data included six bands, which were in 0.45-0.51 μm , 0.53-0.61 μm , 0.61-0.69 μm , 0.69-0.77 μm , 3-5 μm , 8-12.5 μm wavelength region of the electromagnetic spectrum. Based on the field thermal measurements, thermal anomalies caused by coal fires were grouped into 3 categories: low amplitude (up to 20°C above the background), medium amplitude (20-120°C above the background) and high amplitude (over 120°C above the background).

Night-time band 8-12.5 μm data clearly showed coal fires and background areas. However, the disadvantage for this night-time data is saturation at medium and high amplitude areas. Daytime band 8-12.5 μm image was used to detect medium amplitude thermal anomalies, which represent partial underground coal fires with partial solar heating of non-burning coal seams and black shale with higher emissivity. Daytime band 3-5 μm data provided information both from the spectrally reflected solar radiation and radiation from high amplitude surface thermal anomalies of the underground coal fires. Daytime band 0.61-0.69 μm data were used to adjust the band 3-5 μm data for reducing the effects of the spectrally reflected solar radiation. The adjusted image showed the enhanced high-amplitude thermal anomalies of the underground coal fires. Three bands of data have been fused to integrate the background, low, medium, and high amplitude thermal anomalies, which were highly correlated to the field thermal measurements. On the basis of spatial patterns of thermal anomalies and the underground coal fire spreading models set up through field observations, the spreading direction of underground coal fires was inferred into three

groups, namely upward, downward and lateral. Comparing daytime and night-time band 8-12.5 μ m data, the solar heated coal seams were detected as areas that may have the occurrence of high-risk coal fires occurring in the future. This study brings out some interesting points in terms of coal fire spreading direction detection and coal fire favorite area prediction from multi-spectral airborne data.

Airborne thermal remote sensing for detecting coal fires has several advantages. It is time independent. Data can be acquired in daytime and night-time, at any hour, in any season. Time independence makes it possible to get the optimal image with the highest contrast between coal fire areas and the background. It is also height independent. Flying height decides the spatial resolution of an image. High spatial resolution data are essential for detecting coal fires with a small size. It is temperature independent, too. Most scanners are now equipped with internal temperature calibration sources, which are mounted on either side of the angular field of view. The scanner records the radiant temperature of the first calibration source, then sweeps the terrain, and finally records the temperature of the second source. Calibration source could be set at temperatures of different degrees respectively. These reference temperatures provide a scale for determining the terrain temperature. Through adjusting the two calibration sources, data with the interested temperature range can be acquired. The disadvantage of airborne thermal remote sensing for detecting coal fires is the high price for data acquisition.

3.2.2 Using space-borne thermal remote sensors for detecting coal fire thermal anomalies

There are several satellite systems with thermal infrared sensors at spatial resolution ranging from 60m to 1.1km in operation. The Advanced Very High Resolution Radiometer (AVHRR) aboard NOAA has a spatial resolution varying from 1.1km at nadir up to 8km at the border of the image. Along Track Scanning Radiometer (ATSR), another data source for thermal anomaly detection, on board of ESA's ERS-1 satellite has a spatial resolution of approximately one kilometer. Moderate Resolution Imaging Spectroradiometer (MODIS) aboard the Terra (EOS AM-1) satellite, which was launched in December 1999 and began collecting science data in February 2000,

and has a spatial resolution of 1km. The Russian RESURS-1 has a spatial resolution of about 600m. The Bi-spectral InfraRed Detection (BIRD) on the small BIRD satellite, which is a German fire remote sensing satellite, launched in October 2001, has two bands at the wavelength of 3.4-4.2 μ m and 8.5-9.3 μ m with a spatial resolution of 370m. Advanced Space-borne Thermal Emission and Reflectance Radiometer (ASTER), also aboard the Terra (EOS AM-1), spans the 8-12 μ m region with five contiguous bands and enables the possibility of multi-channel split window thermometry at 90m resolution (Kahle et al. 1996). Thematic Mapper (TM) band 6 (10.4 to 12.5 μ m) on Landsat 5 has a spatial resolution of 120m; Enhanced Thematic Mapper (ETM+) band 6 (10.4 to 12.5 μ m) on Landsat 7, launched in April 1999, 60m. The advantage of space-borne remote sensing for coal fire detection is that it is repeatable, cheaper in data acquisition, and easy multi-band manipulation. The disadvantage is the relatively coarse spatial resolution.

3.2.2.1 NOAA AVHRR

NOAA AVHRR has several bands in the thermal infrared region, channel 3 (3.55-3.93 μ m), channel 4 (10.3-11.3 μ m), and channel 5 (11.5-12.5 μ m on NOAA-7,9,11,12&14). This data source has been extensively studied and used for forest fire detection and for biomass burning at national, continental, and even global scales, as the data is acquired globally on a daily bases with both daytime and night-time data acquisition (Belward et al. 1994, Chuvieco & Martin 1994a, b, Chuvieco & Salas 1996, Kaufman et al. 1992, Kennedy et al. 1994, Lopez et al. 1991, Pereira & Setzer 1993, Pereira & Setzer 1996). NOAA-AVHRR data are suitable for studying and monitoring volcanoes (Harris 1995). The first published research to detect underground coal fires using NOAA AVHRR data has been carried out by Mansor et al. (1994). They reported the potential capability of the AVHRR band 3 data to detect the subsurface coal fires in the Jharia coal field in India. They proposed that the good thermal contrast between the coal fire area and its surroundings in the night-time data leads to detection. In the meantime it was reported that the coal fires did not reveal any significantly higher thermal anomalies in the other thermal bands of AVHRR (channel 4 and 5). Zhang (1998) tried to use AVHRR data for detecting underground coal fires in northern China. The research provided no positive or reliable results. It was

mentioned that AVHRR's spatial resolution was too coarse for coal fire detection. MODIS has four bands (band 20: 3.660-3.840 μm , band 21: 3.929-3.989 μm , band 22: 3.929-3.989 μm and band 23: 4.020-4.080 μm) similar to AVHRR channel 3 with 1km spatial resolution. BIRD has one band at the wavelength of 3.4-4.2 μm , but a better spatial resolution of 370m. With these two new sensors, better results can be expected.

3.2.2.2 Landsat TM (ETM+) band 6

Landsat TM band 6 (daytime and night-time) data were the space borne data with the highest spatial resolution (120m) available in the 1990s. Daytime TM band 6 data acquired between 9:30 and 10:30 a.m. were used for detecting underground coal fires by numerous authors (Bhattacharya et al. 1991, 1996, Cracknell & Mansor 1992, Mansor et al. 1994, Prakash et al. 1995a, 1995b, Saraf et al. 1992, 1995, van Genderen et al. 1996, Wan & Zhang 1996a 1996b). Night-time TM band 6 data have the advantage of easing the removal of daytime solar heating effects. But they were difficult to be registered to the base map. They were used by Zhang (1998) and Prakash et al. (1999) to detect coal fires in Xinjiang and Ningxia, China, respectively. Density slicing method with the threshold decided by trial and error technique was the identical method for isolating coal fire areas in all studies.

Saraf et al. (1992, 1995) conducted a typical research in the Jharia coal field, India. They compiled the data and maps of coal fires from the field organizations to a coal fire base map. Then density slicing technique was adopted to identify the threshold digital number (DN) for discriminating pixels related to subsurface coal fire from non-fire ones. The field data of subsurface coal fires served to control the satellite thermal data processing and interpretation at different stages. Trial and error technique was adopted for density slicing using TM band 6 DN-values. It was observed that TM band 6 DN 137/138 threshold in the data set provided a reasonable and overall best match for discriminating non-fire areas from the fire areas. The pattern of TM band 6 digital numbers was converted into kinetic temperature values. It was observed that for the Landsat-TM scene (28 November 1990) the kinetic temperatures ranged from 16.0°C to 31.6°C in the Jharia coal field, with a threshold value of 25.6°C associated with the anomalies. Six classes were classified: thermal anomaly (TM band 6), coal fire (field

data), coal fires observed on the Landsat data and matching with field maps, coal fires that had laterally shifted since mapped, coal fires that were mapped in field but not sensed by TM, coal fires that had probably just started. It was indicated that the limitations arose from the following factors, such as: rather coarse spatial resolution of 120m of TM band 6, ignoring the atmospheric effects, non-uniform background temperature, ignoring lateral variation in spectral emissivity of the ground material, etc.

Reviews on surface temperature estimation using TM band 6 have been given by Gupta (1991), Kahle (1980), Markham & Barker (1986), Reddy et al. (1993), and Rothery et al. (1988). In brief, surface temperature calculation needs three steps. The first step is converting image DN's value back to spectral radiance. The second step is calculating radiant temperature from spectral radiance. The third step is transferring the radiant temperature to surface temperature. During this step, the emissivity of the surface must be known (Becker 1987, Becker & Raffy 1987, Becker & Li 1990a, b, Coll et al. 1994, Gaikovich 1994, Hook et al. 1992). Normally the emissivity value is between 0.8-1 for most natural materials. For the sandstone, shale and the burnt rocks the emissivity can be selected as 0.97 (Li 1985, Nerry et al. 1990, Salisbury & D'Aria 1992, Zhang 1998). It should be mentioned here that for discriminating coal fires it is not always necessary to calculate the surface temperature from the image due to the linear relationship between the digital number and the surface temperature in a certain image.

The sixteen-day repeat cycle of Landsat makes TM (ETM+) band 6 (both during day and night) an ideal data source for monitoring of underground coal fires, and for checking the effectiveness of fire fighting and extinguishing activities being carried out. However, as the spatial resolution of the thermal channel on Landsat TM band 6 is 120 m, small or deep coal fires are often not detected (Zhang et al. 1997a). With the 60 meters spatial resolution of ETM+ band 6 on board, this could be improved. Another way to improve the results is using ASTER data, which has 5 bands in the thermal infrared region (Band 10: 8.125-8.475 μ m, Band 11: 8.475-8.825 μ m, Band 12: 8.925-9.275 μ m, Band 13: 10.25-10.95 μ m and Band 14: 10.95-11.65 μ m) with a spatial resolution of 90m.

3.2.2.3 Landsat TM (ETM+) Band 5 and band 7

During 1990s researchers also started to use short wavelength remote sensing such as band 7 (at the wavelength range of 2.08-2.35 μm) and band 5 (at the wavelength range of 1.55-1.75 μm) of TM data for the detection of high extensive hot sources such as volcanoes and surface coal fires (Andres & Rose 1995, Rothery et al. 1988,1990, Francis & de Silva 1989, Abrams et al. 1991, Bhattacharya et al. 1993 , Gupta & Badrinath 1993, Prakash et al. 1997, Reddy et al. 1993), because these high extensive hot sources can cause the greatest increase of radiance on the shortwave imagery. Using band 5 and band 7, the surface temperature can be calculated (Oppenheimer et al. 1993, Rothery et al. 1998). Furthermore, the size and temperature of the hot sources covering sub-pixel areas can also be retrieved by using band 5 and band 7 through a so-called dual-band method proposed by Dozier (1981) & Matson & Dozier (1981).

Unlike the thermal infrared region of the spectrum where there is negligible reflected solar radiation and measured radiance is virtually all thermal in origin, thermal radiance at shorter wavelengths is combined (in daytime data) with solar radiance which has been reflected by the surface and scattered by the atmosphere. To correct it, the neighbor non-thermal pixels could be used to subtract from the thermal anomaly pixels. This dual band method to detect sub-pixel coal fires was applied by Zhang (1998) and Prakash et al. (1999b) in Xinjiang coal fire area and Jharia coal fire area respectively. The results fitted the field measurements. However, the method is limited by assumptions about the solar reflected component, the background temperature, the spectral emissivity, etc., and particularly by the availability of only two SWIR bands in the TM sensor. ASTER data with a spatial resolution of 30m and 5 SWIR bands (Band 4: 1.600-1.700 μm , Band 5: 2.145-2.185 μm , Band 6: 2.185-2.225 μm , Band 7: 2.235-2.285 μm , Band 8: 2.295-2.365 μm and Band 9: 2.360-2.430 μm) supply a better solution to overcome the shortage of bands availability.

3.2.3 Influence factors in the isolation of fires from other areas

There are a number of factors that are important in the application of thermal remote sensing to detect coal fires. The factors of relief, vegetation, and soil moisture often produce anomalous tones and patterns on thermal infrared imagery which for our

purpose are merely noise and artifacts which needs to be recognized and eliminated either before the survey is flown or during interpretation of the resulting imagery.

Because the aspect and dip angle decide the radiant time and density of the sun, the morphology has a strong relation with the reflectance and radiant temperature of an object (Dave & Bernstein 1982). Guan & van Genderen (1997) measured in the field that the different points on a small hill have different temperature. Figure 3.4 shows positions and temperatures of their measurements. The hill is a light yellow mud hill with a relative high difference about 10 meters. The aspect of the hill's axis is 310° . The measurements were done at the local time 12:00-12:05, when the sun zenith is 33.6° and the sun azimuth is 174° . It can be seen that the temperature difference could reach 18°C . Ellyett & Fleming (1974) mentioned that shadow effects are obvious on the midday image and the evening image shows that slopes with a northwest aspect still remain warmer than southeast-facing slopes. Effects of anisotropic surface heating are minimal on the dawn image and the slopes with different aspect have virtually reached equilibrium, which becomes the best solution for escaping the relief influence for the airborne thermal survey. For space borne thermal data, even though the best time can not be chosen, but the relief influence can be corrected through image processing methods (Holben & Justice 1981, Justice et al. 1981, Kawata et al. 1988). Deng et al. (2001) tried to reduce the effect of solar radiation on TM thermal infrared images, and extracted the thermal anomalies caused by coal fires using neural network training. Wan & Zhang (1996a, b) tried to use a digital elevation model (DEM) to reduce the anisotropic surface heating effects.

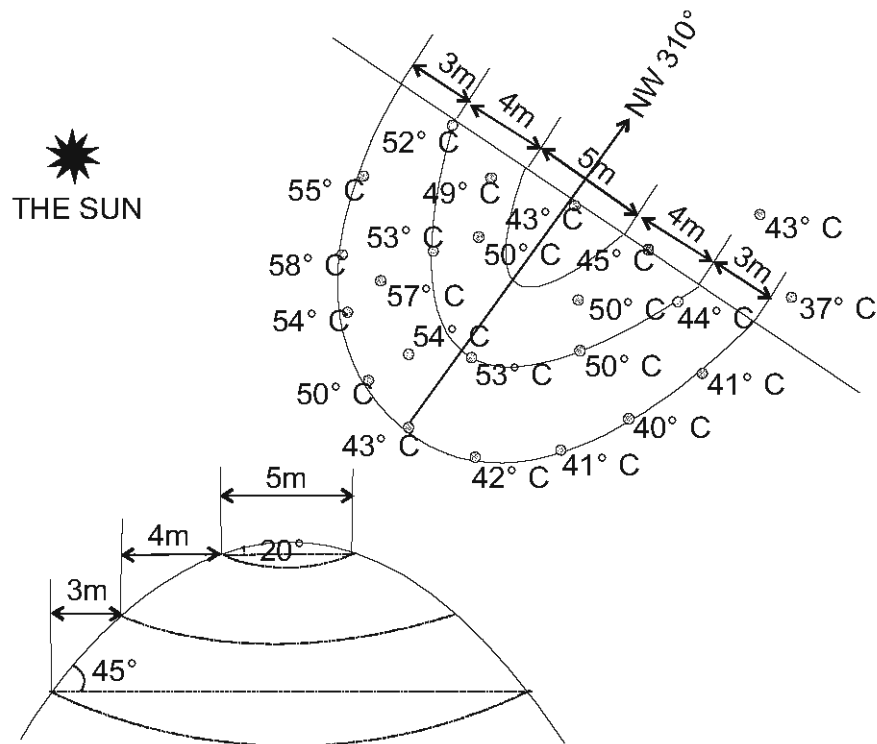


Figure 3.4: Surface temperatures of a light yellow mud hill. Temperatures were measured at the local time 12:00-12:05, when the sun zenith is 33.6° and the sun azimuth is 174° (After Guan & van Genderen 1997).

Materials with different colors have different radiant temperatures. Guan & van Genderen (1997) measured the temperatures of two mudstones, one with the brick-red color and the other with light yellow color. They located in one slope with the same strike and the same dip angle. The distance between them was 1 meter. The measurements were 42°C for the light yellow one and 48°C for the brick-red one, a difference of 6°C.

For the other influencing factors, such as soil moisture, and vegetation, etc., measurements (the reading were made in April 1972 between 10:30 and 12:50 hours under fine weather conditions) indicate that soil overlying sediments is some 4°C hotter than that overlying basalt, areas of damp soil over both rock types were up to 3°C cooler than the dry soil, and a difference of 10°C was observed between the sun-

facing sparsely vegetated basalt area and the heavily grassed southeast facing slope (Ellyett & Fleming 1974). It is reported that the wind influenced the radiant temperature of the surface (Sabins 1996), which Singh (1994) also confirmed for water surfaces.

3.3 Summary and Discussion

When using thermal remote sensing data to detect coal fires, the factors of relief, vegetation, soil moisture, etc. often produce anomalies on imagery which for our purpose are merely noise that needs to be recognized and eliminated. The background temperature, the quality of the thermal remote sensing data, and the significance of the coal fires are the factors which determine the detectability of coal fires. Surface temperature could be calculated according to the calibration sources in the airborne thermal sensor, or according to Plank's formula for the space sensor, such as Landsat TM (ETM+). Then the front, depth, and age of a fire can be inferred through coal fire thermal models (Cassells & van Genderen 1995, Cassells et al. 1996). At the mean time the atmospheric influence should be also considered and corrected with different methods (Bartolucci et al. 1988, Cooper & Asrar 1989, Desjardins et al. 1990, Eymard & Taconet 1995, Li & McDonnell 1988, Ouaidrari et al. 1994, Singh 1984, Sobrino et al. 1991, Vidal 1991, Wukelic et al. 1989).

Since the first test in 1964, airborne thermal remote sensing to detect coal fires has been successfully applied in a number of countries, such as United States, Australia, India, and China. The method is practicable nowadays because the spatial resolution and the acquisition time can be chosen according to the purpose of the campaign. This allows reducing anisotropic illumination of the terrain by the sun and also makes the detection of coal fires of small size feasible. For airborne thermal survey the image spatial resolution is given by the fly height of the plane, which is flexible. Normally 3-10m spatial resolution image was used for detecting coal fires. The higher the spatial resolution is, the smaller the size of coal fires that can be detected. But, the more data come, the more time is required for data processing and interpretation. Therefore, it is important to choose the suitable spatial resolution for airborne thermal surveys.

Space borne remote sensing for detecting coal fires, on the other side, is restrained by the fixed overflight time and spatial resolution. The relatively coarse spatial resolution is one main limitation of spaceborne data. Zhang et al. (1997a) mentioned that Landsat TM night-time thermal data are suitable for regional coal fire investigation, but for early detection of coal fires with a relatively small size and low temperature, their 120 m spatial resolution is still too coarse. Higher spatial resolution Landsat thermal image could be simulated (Liu & Moore 1997), but it is not suitable for the purpose of coal fire detection. All previous studies using space borne data were using GIS (with coal fires distribution map) based trial and error density slicing method, which is only suitable for the known areas (Chen 1992, Reddy & Bhattacharya 1995, Vekerdy & van Genderen 1999, Vekerdy et al. 1999, Zhang et al. 1997a,b, 1998). So far the methods have not been applied in an operational fashion over large areas. With the ASTER and Landsat 7 ETM+ band 6, space borne thermal data with the spatial resolution of 90m and 60 m are achieved, which will improve the ability of coal fire detection in large areas.

Chapter 4 DESCRIPTION OF THE STUDY AREAS & DATA SETS

4.1 Location of the Study Areas

Three study areas are chosen in the research, which are the Wuda area, the Ruqigou area, and the Gulaben area. Figure 4.1 shows their locations.

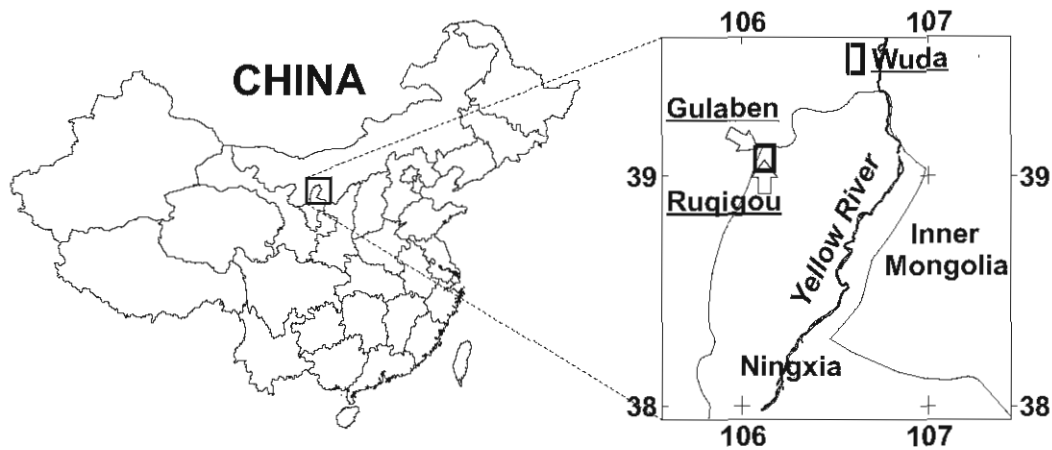


Figure 4.1 Location of the study areas

The Wuda area includes Wuda coalfield and its surrounding areas in Inner Mongolia Autonomous Region. Wuda coalfield is located at $39^{\circ}28' - 39^{\circ}34'N$ and $106^{\circ}36'40'' - 106^{\circ}38'41''E$, and extends for 10km from North to South and 3-5km from East to West, covering an area of 35km^2 . The Wuda area lies on the western side of the Yellow River, north of the Helan mountain range not far from the border to Ningxia Hui Autonomous Region. Northwest of the Wuda area is the Badai Jaran Desert. Altitude in the study area of Wuda varies from 1010 to 1980 meters above sea level.

The Ruqigou area, located within the northern part of the Helan mountain range, is in Ningxia Hui Autonomous Region. Ruqigou coalfield is situated between latitudes $39^{\circ}00'54''N$ and $39^{\circ}08'10''N$ and between longitudes $106^{\circ}02'54''E$ and $106^{\circ}11'23''E$. It is 14km long and 5.3km wide, covering an area of nearly 54km^2 . The average altitude is 2000m. The highest peak in the area reaches 2451m. The lowest part of the area is at its northeastern limit, with an altitude of about 1800m.

The Gulaben area is adjacent to the Ruqigou area, but in Inner Mongolia Autonomous Region. It is located about 25km west of Shizuishan-Dawukou City and 70 km northwest of Yinchuan City. The highest peak of the area is 2725m and the lowest part is 1813m.

4.2 Geography

4.2.1 Climate and hydrology

The climate of Wuda, Ruqigou, and Gulaben area is a middle latitude strong continental semi-arid to fully arid climate, with large daily and seasonal temperature amplitudes influenced mainly by the East Asian Monsoon (Weischet 1988, Xie 2001). Winters are cold and long, summers can be very hot, precipitation is low and winds are strong. The climate station in Yinchuan (1112m above sea level) shows an average annual temperature of 8.6°C, an average annual precipitation amount of 193 mm, and an average absolute daily maximum and minimum of 39.3°C and -30.6°C respectively. Since precipitation in northern Ningxia decreases from the South to the North precipitation in Wuda is substantially lower than in Ruqigou and Gulaben. It averages 100-150 mm and is distributed to 7-20 days within the year. Annual evaporation rates of above 2500 mm lead to a water shortage of the surface flow as well as underground (Chen 1997, Kuenzer et al. 2003, Wu & Zhang 2003).

As a consequence, most fluvial features like creeks, wadis, and small rivers are seasonal. One exception is the Yellow River running from South to North through Ningxia Autonomous Region and into Inner Mongolia Autonomous Region, being the most important water supply for agricultural irrigation. The run off from the mountains in the study areas is nearly 100%, due to the sparse development of soil- and vegetation cover, accounting for large water volumes transported in the wadi beds in times of rainfall or snowmelt (Kuenzer et al. 2003, Rosema et al. 1999).

4.2.2 Soils and vegetation

Due to the semi-arid to arid climate soil development in the area is slow. Therefore, large areas, especially in the mountains and structural hill slopes, show no soil cover but weathered bedrock, a cover of aeolian sand or coarse alluvial fan material. Soils

occur mainly on the irrigated river terraces of the Yellow River and on its actual floodplains as sandy, silty and loamy types. On a global scale the soils of the region (except the ones influenced by rivers) belong to the class of grey to brown half-desert and desert soils (Driessen & Dudal 1991).

Vegetation cover is very sparse too and is dominated by dry desert shrubs with partially sclerophyllous leaves, which are commonly *Tetrandea mongolica*, *Reaumuria soongorica*, *Bassia dasyphylla* and species of *Artemisia*. Furthermore, in the Helan Shan Mountains and on gentle hillslopes and alluvial fans sparsely distributed grasslands, partly used for grazing, can be found (Chen 1997, Kuenzer et al. 2003).

4.2.3 Economy

The predominant sources of employment are coal mining and related activities. Coal mining takes place in state-run, locally-controlled and private mines. Coal mining related industry includes coal washing, coal cooking and coal power plants, respectively. Here, labour productivity is very low compared to other countries. The average coal output per employee is 163 t/year which is only 1/20th of a worker in e.g. South Africa (Daniel 1994).

Further heavy industries in the area are limestone processing and related calcite and cement factories, dolomite processing, brick burning and loess mining, iron melters, cokes factories, and carbide factories. A good transportation network of roads and railways has been developed, which allows the transportation of coal and other products to the neighbouring provinces and bigger cities.

In addition to industry, the primary agricultural sector is another main source of income for the local inhabitants. Commercially grown food products include corn, sunflowers, rice, potatoes, soybeans, vegetables and fruits. These activities are mainly restricted to the flood plains of the Yellow River's, irrigated terraces and other irrigated areas. Irrigation activities and cultivation of bare land have especially increased since the economic reform at the end of the 1980s with resulting land cover changes in the Yellow River Valley and plains (Wu & Zhang 2003).

Typical average work wages range between 700 Yuan per month (ca. 90 €) for a coal worker in a state run mine, 400 Yuan per month (ca. 50€) for a middle school teacher and less than 160 Yuan (ca. 20 €) per month for a subsistence farmer (Kuenzer et al. 2003, Sun 2003, Zhang 2003).

4.3 Geology

The north-south striking syncline in Wuda coalfield holds a geological reserve of 630 Million tons of coal. The coal layers originate from Upper Carboniferous and Lower Permian times. Quaternary alluvial layers of silt, shale and gravel cover small parts of the Permian and Carboniferous outcrops. In the Lower Permian Shanxi Formation (P1S), there are 10 coal seams, from upper to lower, named 1[#], 2^{#U}, 2[#], 3[#], 4^{#U}, 4[#], 4^{#L}, 5[#], 6[#], and 7[#], embedded with sandstone. The total thickness of the coal seams in the formation is 13-19m. The Lower Permian Shanxi Formation is conformably overlain on the Upper Carboniferous Taiyuan Formation. In the Upper Carboniferous Taiyuan Formation, there are 17 coal seams, named 8[#], 9[#], 10[#], 11[#], 12^{#U}, 12[#], 12^{#L}, 13^{#U3}, 13^{#U2}, 13^{#U1}, 13[#], 13^{#L}, 14[#], 15[#], 16[#], 17[#] and 18[#], interbedded in different layers of coarse to fine-grained white to dark grey or yellowish sandstone and greyish-, brown- or green-yellowish shale. The average thickness of the coal seams is 22.6m. Among these 27 coal seams, 12 coal seams (1[#], 2[#], 4[#], 5[#], 6[#], 7[#], 9[#], 10[#], 12[#], 13^{#U2}, 13[#], and 15[#]) are stably distributed and mineable in the coalfield. Seven coal seams (8[#], 11[#], 13^{#U3}, 13^{#U1}, 14[#], 16[#], and 17[#]) are mineable in some part of the coalfield. The mineable coal seams have an average total thickness of 33.6m. Mineable reserves are stated to be 27 Million tons in Wuda coalfield, where coal is mined within the three coal mining fields of Wuhushan in the South, Huangbaici in the East and Suhaitu in the Northwest. From these fields three different quality types of coal – fat coal, cooking coal and steam coal - are being extracted. (Jia 2002, Ma 2002, Sun2003, and Zhang 2003).

The Ruqigou and Gulaben coal fields belong to an asymmetrical Jurassic synclinal basin located in the Helanshan at the western rim of the Paleo-Mesozoic sedimentary Ordos Basin. The syncline covers an area of approximately 80 km². Gulaben area is located at the western rim of Ruqigou syncline turning into Houlugou anticline. The 10

main coal seams of the two regions were deposited under lacustrine-fluvial conditions during the Middle Jurassic and are well exposed nowadays due to the Yanshanian uplift and erosion (Zhang, 1997). Among the 10 main coal seams, only some of them are minable. Most mining activities are concentrated in the coal seam 2, which consists of several, discontinuous splits. Average coal rank is high and ranges from low volatile bituminous coal to high quality Anthracite, resulting in a very good export market. Ruqigou and Gulaben area together hold a proven geologic reserve of 1.040 million tons with prospects of nearly 1 billion tons. The coal seams are interbedded in different layers of older Triassic (Yanchang formation) and younger Jurassic (Zhiluo formation) fine to coarse grained white to grey sandstones, purplish red mudstones, yellow-green siltstones and shale, occasional deposits of claystones and interbedded conglomerates (Chen 1997).

4.4 Coal Fires

4.4.1 Coal fires in Wuda

In the Wuda coal field, most coal seams have a gentle dip angle of 5°-8°. In the most southern part of the coal field, close to the axis of the syncline, coal seams have a dip angle of 8°-12°. Only the coal seams close to the fault in the eastern part of the coal field have a high dip angle. The small mines operate the dip direction from the outcrop of the coal seam into the underground. The deepest mine digs 400-800m from the mining entrance into the seam; the deepest coal fire is not deeper than 50m. Most coal fires in the Wuda area have started from the surface outcrop of the coal seams. They burn down along goafs. When they meet a coal mined area, they become stronger due to the improved ventilation. When pillars have been burnt out, land subsidence may occur. Cracks with high temperature on the surface are formed. The last crack on the surface usually corresponds with the front of the coal fire underground. According to the geomorphology, the coal fire areas can be easily demarcated on the map with the help of GPS measurements and temperatures measurements. Table 4.1 shows characteristics of the 17 coal fires investigated in the 2002 field work, in the Wuda area, including location, perimeter, area, and burning coal seam. The total coal fire area in the Wuda coalfield is 2,85km².

Fire	Coordinate(WGS 84, Zone 48)	Perimeter (m)	Area (m ²)	Burning seam
1	(640099, 4380179)	2188	236402	12 [#]
2	(638712, 4378768)	871	26412	12 [#]
3	(639688, 4379233)	2103	130056	9 [#] ,10 [#]
4	(639041, 4377751)	773	31918	9 [#] ,10 [#]
5	(639633, 4377974)	849	34701	6 [#] ,7 [#]
6	(638932, 4376809)	2744	226920	9 [#] , 10 [#]
7	(641239, 4376211)	2058	226596	1 [#] , 2 [#]
8	(639283, 4374042)	8922	491486	9 [#] , 10 [#]
9	(639993, 4374895)	609	22223	6 [#] ,7 [#]
10	(640598, 4374524)	2794	357171	1 [#] , 2 [#] , 4 [#]
11	(640760, 4373431)	4579	713900	2 [#] , 4 [#]
12	(640655, 4371896)	2129	159780	2 [#] , 4 [#]
13	(640242, 4372078)	1283	42954	6 [#] ,7 [#]
14	(641489, 4371742)	1448	74229	2 [#] , 4 [#]
15	(639482, 4377132)	571	15682	9 [#] ,10 [#]
16	(638804, 4378185)	279	3834	12 [#]
17	(641047, 4375570)	1272	60244	1 [#] , 2 [#]

Table 4.1 Dimensions of coal fires in the Wuda coalfield

The first coal fire in Wuda started in 1961 due to spontaneous combustion of coal. In 1980s, more coal fires ignited due to the private mining activities in the area. In 2002, coal fires are distributed in most of the coalfield as shown in Figure 4.2.

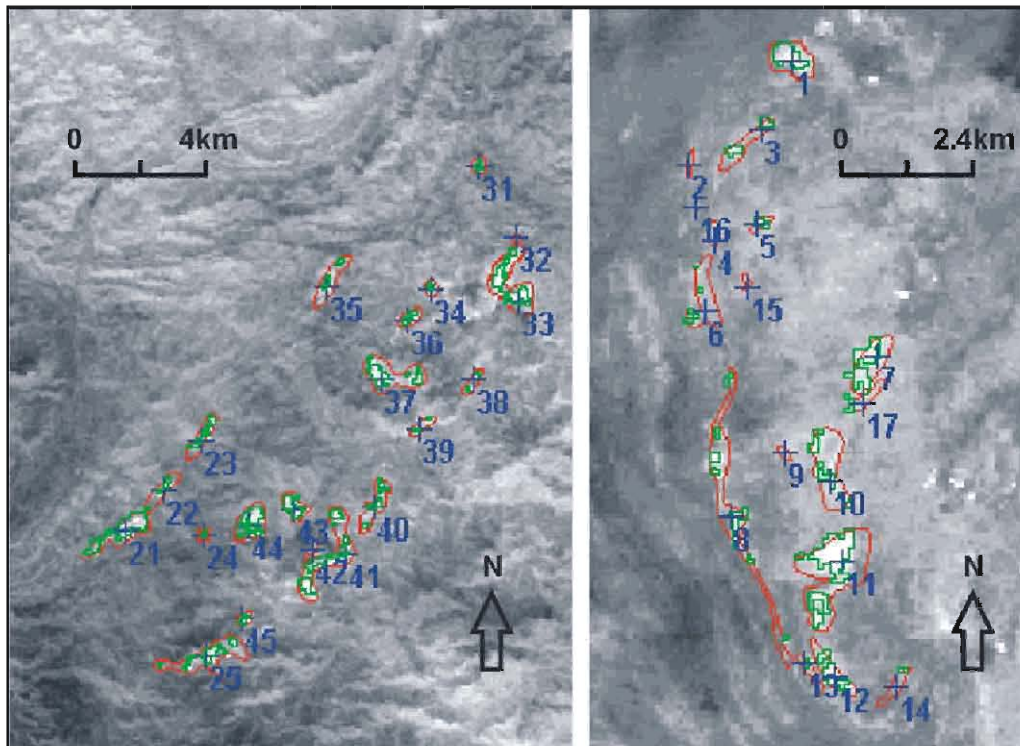


Figure 4.2: Coal fires in the study areas. Right: Wuda area; Left: Ruqigou and Gulaben area. Red: coal fire area mapped in the field; Green: thermal anomalous pixels interpreted from the background image; Background image: nighttime Landsat 7 band 6, 226-211, received on 28 September 2002; Number 1-45: coal fire name number. Coal fires in Wuda area have been numbered from 1-17. Coal fires in Gulaben area have been numbered from 21-25. Coal fires in Rujigou have been numbered from 31-45.

4.4.2 Coal fires in Ruqigou

Coal seams in Ruqigou coalfield have gentle dip angles like in Wuda. Most coal fires started from the surface outcrop of the coal seam and burnt into the underground. Some of the coal fires reach depths of up to 100m. Most coal fires occur in coal seam 2[#] and 3[#]. There are a total of 16 coal fires in Ruqigou coalfield according to the 2002 field investigation. Figure 4.2 shows their distribution. Table 4.2 shows their dimensions. The total coal fire area of the Ruqigou coalfield is calculated as 4,36km².

Fire	Coordinate (WGS 84, Zone 48)	Perimeter (m)	Area (m ²)
31	(599670, 4331795)	1135	96018
32	(600528, 4330205)	581	24382
33	(600560, 4328775)	5666	778371
34	(598621, 4329061)	1157	95647
35	(596269, 4329124)	3001	339362
36	(598049, 4328361)	1510	145343
37	(597477, 4327058)	4037	647324
38	(599575, 4327026)	1657	120155
39	(598335, 4325945)	1608	114454
40	(597350, 4324165)	3282	357998
41	(596714, 4323148)	6133	840449
42	(595951, 4323243)	883	40143
43	(595538, 4324134)	2027	244392
44	(594520, 4323784)	2545	431768
45	(594393, 4321686)	1100	87321

Table 4.2 Dimensions of coal fires in the Ruqigou coalfield

4.4.3 Coal fires in Gulaben

In the Gulaben coalfield, coal seams have a steep dip angle of 45°-60°. The minable coal seams usually have a very short distance from one to the other. Coal fires are limited from the outcrop areas as shown in Figure 4.2. Table 4.3 shows their dimensions. The total coal fire area of the Gulaben coalfield is calculated as 1,80km².

Fire	Coordinate (WGS 84, Zone 48)	Perimeter (m)	Area (m ²)
21	(591796, 4323666)	4057	545038
22	(592601, 4324554)	2595	251360
23	(593461, 4325692)	2602	254596
24	(593517, 4323527)	741	37094
25	(593573, 4320834)	5418	712815

Table 4.3 Dimensions of coal fires in the Gulaben coalfield

Except Coal fire 21, which started about 100 years ago with an unclear ignition source, the other four coal fires were all caused by the careless spreading of man-made fires in the mine for heating in the winter time. The coal in the Gulaben coal field is high metamorphosed anthracite. It is unlikely to experience spontaneous combustion.

4.5 Coal Mining

Coal mining in the study areas started about one hundred years ago. The early coal mining was in the hands of private entrepreneurs. Often with limited means, the mining operations were confined along the outcrop regions and the shallow places. The extensive state-controlled coal mining was started in the 1960's. These state-controlled coal mines are mainly distributed in the following areas: the Baijigou coal mine area, the Dafeng coal mine area, and the Ruqigou coal mine area in the Ruqigou coalfield; the Wuhushan mine area, the Huangbaici mine area, and the Suhaitu mine area in the Wuda coalfield; and Gulaben mine area in the Gulaben coalfield. Because of the good accessibility of the coal seams, the small private pits are still playing a vital role. They spread over the whole study area (Chen 1997).

Next to underground mining, open cast mining is one of the major extraction methods in the study areas. It is mainly used in those places where the coal seams are shallow and the bedding planes are gentle. With this method a large amount of overburden has to be removed from above the coal seam and a lot of waste is produced. There are two kinds of open cast mining in the study areas. One is to remove the overburden above the coal seam completely as done at the Dafeng coal mine shown in Figure 4.3. The other is to remove the overburden partially, which usually takes place under steep scarps and is employed in many places as one shown in Figure 4.4.



Figure 4.3 Open cast mining in Dafeng coal mine, Ruqigou coalfield



Figure 4.4 Open cast mining in a private pit, Wuda coalfield

4.6 Data Available

- For this research the following data were available:
- Geological and tectonic map of the Ningxia Hui Autonomous Region (1:350,000)
- Geological map of Wuda coalfield (1:5000)
- Coal fire distribution maps of the study areas (1:5000)
- A number of papers and reports with relevant coal fire and coal geology information of the study areas

- Seven scenes of Landsat-7 ETM+ data covering the study areas and a coal fire area in Xinjiang acquired during daytime and night-time
- Plenty of field temperature measurements

Chapter 5 THEORY

5.1 Thermal Processes and Properties

All matter radiates energy at thermal infrared wavelengths (3 to 15 μ m) both day and night. This radiation can be recorded as images. To interpret thermal infrared images, it is necessary to understand the basic physical processes that control the interactions between thermal energy and matter, as well as the thermal properties of matter that determine the rate and intensity of the interactions (Sabins 1996).

5.1.1 Heat, temperature, radiant flux and heat transfer

Kinetic heat is the energy of particles of matter in a random motion. The random motion causes particles to collide, resulting in changes of energy state and the emission of electromagnetic radiation from the surface of materials. The internal, or kinetic, heat energy of matter is thus converted into radiant energy.

Temperature is a measure of the concentration of heat. On the Celsius scale, 0°C and 100°C are the temperatures of melting ice and boiling water, respectively. On the Kelvin, or absolute, temperature scale, 0K is absolute zero, the point at which all molecular motion ceases. The Kelvin and Celsius scales relate as follows:

$$T_c = T_k + 273.16 \quad (1)$$

Where T_c is temperature in Celsius and T_k is temperature in Kelvin.

The electromagnetic energy radiated from a source is normally expressed as radiant flux and is measured in watts per square centimeter. The concentration of kinetic heat of a material is called the kinetic temperature and is measured with a thermometer placed in direct contact with the material. The concentration of the radiant flux of a body is the radiant temperature. Radiant temperatures can be measured remotely by nonimaging devices called radiometers. The radiant temperature of materials is always less than the kinetic temperature because of a thermal property called emissivity, which is defined as radiant flux from a real material divided by the radiant flux from a

blackbody. A blackbody is a theoretical material that absorbs all the radiant energy that strikes it.

Heat energy is transferred from one place to another by three means. 1). Conduction: it transfers heat through a material by molecular contact. 2). Convection: it transfers heat through the physical movement of heated matter. 3). Radiation: it transfers heat in the form of electromagnetic waves.

5.1.2 Radiant energy peaks and Wien's displacement law

For an object at a constant kinetic temperature, the radiant energy, or flux, varies as a function of wavelength. The radiant energy peak (λ_{max}) is the wavelength at which the maximum amount of energy is radiated. Figure 5.1 shows radiant energy curves for objects ranging in temperature from 300K to 600K. As the temperature increases, the total amount of radiant energy increases and the radiant energy peak shifts towards shorter wavelengths. This shift, or displacement, to shorter wavelengths with increasing temperature is described by Wien's displacement law.

$$\lambda_{max} = \frac{2897}{T_{rad}} \quad (2)$$

where T_{rad} is radiant temperature in degrees Kelvin and 2897 $\mu\text{m.K}$ is a physical constant

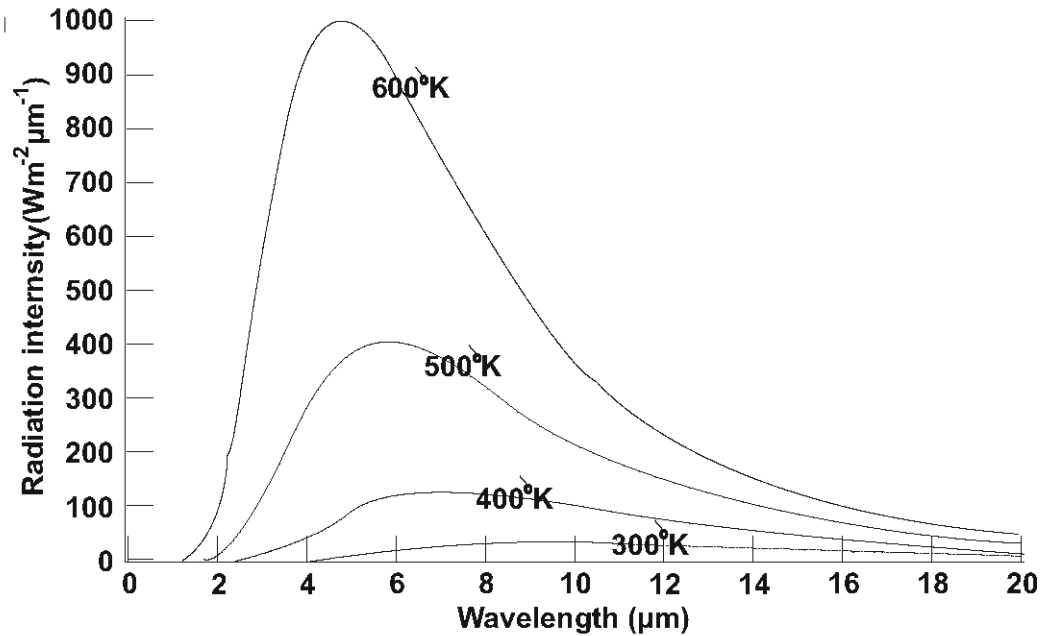


Figure 5.1: Spectral distribution curves of energy radiated from objects at different temperatures. The radiation peaks are 9.7 μm , 7.2 μm , 5.8 μm and 4.8 μm for temperatures of 300, 400, 500 and 600 K respectively.

5.1.3 Blackbody concept, emissivity and radiant temperature

The concept of a blackbody is fundamental to understand the principles of heat radiation. A blackbody absorbs all the radiant energy that strikes it, also radiates all of its energy in a wavelength distribution pattern that is dependent only on the kinetic temperature.

According to the Stefan-Boltzmann law, the radiant flux of a blackbody (F_b) at a kinetic temperature of T_{kin} is

$$F_b = \sigma \times T_{kin}^4 \quad (3)$$

Where σ is the Stefan-Boltzmann constant ($5.67 * 10^{-12} \text{ W} \cdot \text{cm}^{-2} \cdot \text{K}^{-4}$).

A blackbody is a physical abstraction, because no material has an absorptivity of 1 and no material radiates the full amount of energy given in the Equation (3). For real materials a property called emissivity (ε) has been defined as

$$\varepsilon = \frac{F_r}{F_b} \quad (4)$$

where F_r is radiant flux from a real material.

The emissivity for a blackbody is 1, but for all real material it is less than 1. Emissivity is wavelength-dependent, which means that the emissivity of a real material will be different when measured at different wavelengths of radiant energy. Materials with high emissivities absorb large amounts of incident energy and radiate large quantities of kinetic energy. Materials with low emissivities absorb and radiate lower amounts of energy.

Most thermal infrared remote sensing systems record the radiant temperature (T_{rad}) of terrain rather than radiant flux.

$$T_{rad} = \varepsilon^{\frac{1}{4}} \times T_{kin} \quad (5)$$

5.2 Radiant Temperature Retrieve from Airborne IR Scanners and Landsat-7 ETM+ Band 6

5.2.1 Airborne IR scanners and their radiant temperature retrieval

The radiant temperature of airborne infrared scanners can be retrieved using the following equation:

$$T_{(DN)} = BB_1 + DN \times \frac{BB_2 - BB_1}{DN_{max}} \quad (6)$$

Where $T_{(DN)}$ is the pixel integrated temperature. BB_1 and BB_2 are two reference temperatures of internal blackbodies installed in the sensor. DN is the digital number from thermal data. DN_{max} is the maximum value the image recorded.

5.2.2 Radiant Temperature retrieval for the example of Landsat ETM+ band 6

The procedure for converting the DN value of ETM+ band 6 to the surface temperature includes the following three steps:

Step1. Converting image DN's value back to spectral radiance

For Landsat 7, ETM+ band 6, image pixels are converted to units of absolute radiance using 32 bit float point calculations during 1G product rendering. Pixel values are then scaled to byte values prior to media output. The following equation is used to convert DNs in a 1G product back to radiance units (Landsat Project Science Office 1998, Wang 2002).

$$Radiance = gain \times DN + offset \quad (7)$$

Which is also expressed as:

$$L_{\lambda} = (DN - 1) \times \frac{L_{max} - L_{min}}{255 - 1} + L_{min} \quad (8)$$

Where the L_{λ} is the spectral radiance of a band. The L_{min} and L_{max} are the spectral radiances for each band at digital number 1 and 255, respectively. One set exists for each gain state. These values will change slowly over time as the ETM+ detectors loose responsivity. For ETM+ band 6 Low Gain, $L_{min} = 0.0$ ($W \cdot m^{-2} \cdot sr^{-1} \cdot \mu m^{-1}$), and $L_{max} = 17.04$ ($W \cdot m^{-2} \cdot sr^{-1} \cdot \mu m^{-1}$). For high Gain, $L_{min} = 3.2$ ($W \cdot m^{-2} \cdot sr^{-1} \cdot \mu m^{-1}$), and $L_{max} = 12.65$ ($W \cdot m^{-2} \cdot sr^{-1} \cdot \mu m^{-1}$). After putting these parameters into equation (8), we can use the following equation to calculate the radiance for ETM+ band 6 low gain and high gain:

$$L_{\lambda L} = 0.067 DN - 0.067 \quad (9)$$

$$L_{\lambda H} = 0.0372 DN - 3.16 \quad (10)$$

Where, $L_{\lambda L}$ is the radiance for the DN in ETM+ band 6 low gain, and $L_{\lambda H}$ is the radiance for the DN in ETM+ band 6 high gain.

Step 2. Calculating radiant temperature from spectral radiance

The radiant temperature can be converted from spectral radiance according to Planck's equation, which expresses the relation between the spectral radiance and the radiant temperature. This is the effective at-satellite temperatures of the observed Earth-

atmosphere system under an assumption of unity emissivity and using pre-launch calibration constants. The conversion formula is:

$$T_{rad} = \frac{K_2}{\ln\left(\frac{K_1}{L_\lambda} + 1\right)} \quad (11)$$

Where T_{rad} is effective at-satellite temperature in Kelvin. L_λ is spectral radiance in $W \cdot m^{-2} \cdot sr^{-1} \cdot \mu m^{-1}$. $K1 = 666.09$ ($W \cdot m^{-2} \cdot sr^{-1} \cdot \mu m^{-1}$). $K2 = 1282.71$ K.

Step 3. Transferring the radiant temperature to surface temperature

According to the equation (5), the apparent or the brightness temperature can be converted into the kinetic or true temperature of the surface.

$$T_{kin} = \varepsilon^{-\frac{1}{4}} \times T_{rad} \quad (12)$$

Where T_{kin} is the surface temperature at wavelength λ . T_{rad} is radiant temperature. And ε is the emissivity of the surface.

Emissivity values in the spectral region of the ETM+ thermal band range between 0.8-1 for most natural materials. For sandstone, shale and the burnt rocks the emissivity can be selected as 0.97 (Li, 1985, Nerry et al., 1990, Salisbury & D'Aria, 1992, Zhang 1998). Surface temperatures in Celsius can be calculated using the equation (1). Atmospheric corrections need to be applied in step 1 if the atmosphere influence is taken into account.

Figure 5.2 shows the relation between DN's and Temperature of Landsat 7 ETM+ band 6. In order to discriminate coal fires it is not necessary to calculate the surface temperature from the image due to the one-to-one relationship between the digital number and the surface temperature in a certain image.

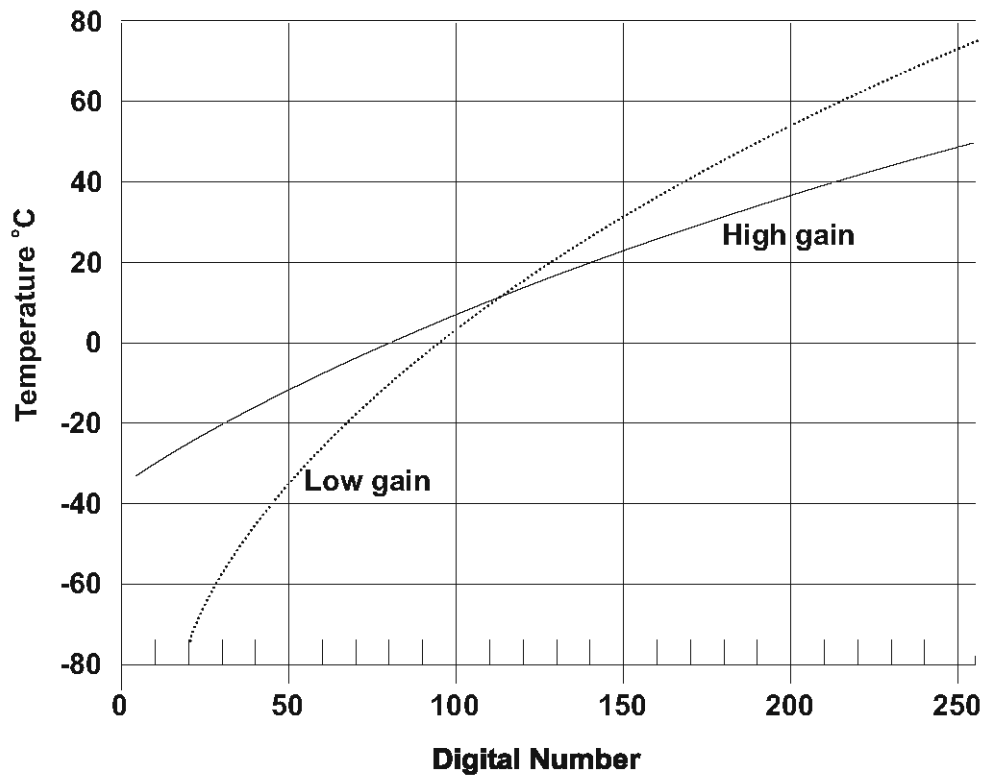


Figure 5.2: Relation of DNs and temperature of Landsat 7 ETM+ band 6

5.3 Thermal Data of Band 3-5 μm and 8-14 μm for Underground Coal Fire Detection

When a physical object, such as a coal fire, radiates a heat flux higher than the background (or its neighbourhood), it forms a thermal anomaly on the surface. When the heat flux difference between the object and its background can be differentiated by a thermal infrared image, the object causes a thermal anomaly in the image.

5.3.1 Detecting full pixel coal fires

When a coal fire related thermal anomaly on the surface is larger than an image pixel, the fire can be called 'full-pixel' coal fire. Otherwise, it may be called a 'sub-pixel' coal fire. A full-pixel coal fire is easier to form a thermal anomaly in the image than the sub-pixel coal fire. The formation of a thermal anomaly in an image for a coal fire is dependent on the following 4 factors. 1). Remote sensor's working wavelength, 2). The image spatial resolution, 3). The temperature and the size of the fire, and 4). The

temperature contrast between the fire and its background. The night-time band 8-14 μm image has the highest capability to detect coal fire induced low temperature thermal anomaly. A high spatial resolution image allows more thermal anomalies of coal fires to be picked up in the image. It is relatively easy to quantify a full pixel coal fire if the pixel DN value is not saturated. Its spatial extension and temperature can be derived from the anomalous pixels in the image directly. Care should be taken for the fact that nearly all full-pixel coal fires will saturate ETM+ band 6 (Tetzlaff 2004).

5.3.2 Detecting sub-pixel coal fires

Field observations and measurements showed that coal fire induced thermal anomalies, especially the high temperature anomalies, are usually smaller than the size of a pixel. Detecting such small (sub-pixel sized) coal fires is of great importance to identify coal fires at their early stage and to pinpoint the coal fire cores. Sub-pixel coal fire detection is based on the assumption that a sub-pixel fire can be detected when the equivalent spectral radiance as a full pixel is larger than the background.

Spectral radiance L_λ of a black body with a temperature T (radiant temperature is the same as kinetic temperature) at the wavelength λ can be calculated by using the Plank's Equation:

$$L_\lambda = \frac{2hc^2}{\lambda^5} (e^{hc/\lambda kT} - 1)^{-1} \quad (13)$$

Where e , h , c , and k are constants.

For real material, the radiant temperature (T) of the material can be calculated from its kinetic temperature (T_{kin}) through the formula (5).

The radiance of an object with the radiant temperature T in band λ_1 - λ_2 ($L_{(\lambda_1-\lambda_2)}$) can be calculated by:

$$L_{(\lambda_1 - \lambda_2)} = \int_{\lambda_1}^{\lambda_2} L_\lambda \cdot d\lambda \quad (14)$$

The spectral radiance from the ground to the sensor passes the atmosphere. Suppose the atmospheric influence function is A_λ . The radiance from the ground is L_λ . The radiance reached to the sensor is $L_{\lambda Sensor}$.

$$L_{\lambda Sensor} = A_\lambda \times L_\lambda \quad (15)$$

When the spectral radiance reaches a thermal sensor, the sensor responds and records it following the sensor's response function (R_λ) as shown in equation (16).

$$L_{\lambda Image} = R_\lambda \times L_{\lambda Sensor} \quad (16)$$

where $L_{\lambda Sensor}$ is the spectral radiance of the surface reached to the sensor. R_λ is the sensor's response function. And $L_{\lambda Image}$ is the spectral radiance recorded by the image of the sensor.

When a coal fire induced thermal anomaly occupies a sub-pixel area (Figure 5.3), the total amount of radiance from the full pixel at the wavelength λ is (Matson & Dozier, 1981):

$$L_\lambda = L_{\lambda f} \times P + L_{\lambda b} \times (1 - P) \quad (17)$$

Where L_λ is the total spectral radiance of a pixel at wavelength λ . $L_{\lambda f}$ is the spectral radiance of a coal fire at wavelength λ . $L_{\lambda b}$ is the spectral radiance of the background at wavelength λ . P is the portion of a pixel occupied by a coal fire.

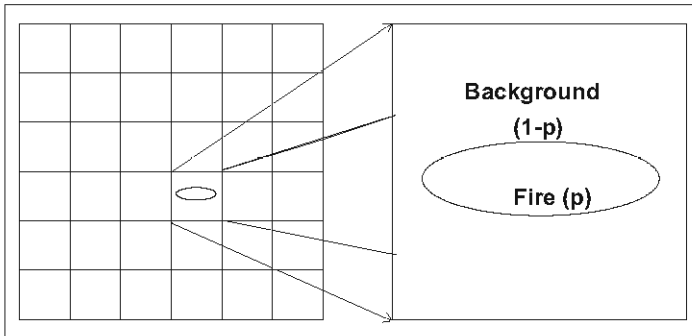


Figure 5.3: A sub-pixel sized coal fire occupying a portion (p) of the pixel area.

When the recorded radiance from a pixel containing a sub-pixel sized fire with a portion of P is larger than the radiance of a full pixel of the background, this pixel can be detected as a thermal anomaly and the sub-pixel fire is called detected.

From formula (17), we know:

$$P = \frac{L_{\lambda} - L_{\lambda b}}{L_{\lambda f} - L_{\lambda b}} \quad (18)$$

Combining formula (13), (14), (15), (16), and putting in the constants, we have:

$$L_{(\lambda_1 - \lambda_2)} = R_{\lambda} A_{\lambda} \int_{\lambda_1}^{\lambda_2} (e^{\frac{1.44 \times 10^4}{T \times \lambda}} - 1)^{-1} \cdot d\lambda \quad (19)$$

From formula (18) and (19), the following formula can be deduced:

$$P = \frac{\int_{\lambda_1}^{\lambda_2} ((e^{\frac{1.44 \times 10^4}{T_{thr} \times \lambda}} - 1)^{-1} - (e^{\frac{1.44 \times 10^4}{T_{bac} \times \lambda}} - 1)^{-1}) d\lambda}{\int_{\lambda_1}^{\lambda_2} ((e^{\frac{1.44 \times 10^4}{T_{fir} \times \lambda}} - 1)^{-1} - (e^{\frac{1.44 \times 10^4}{T_{bac} \times \lambda}} - 1)^{-1}) d\lambda} \quad (20)$$

Where,

P is the portion of a sub-pixel coal fire which can be detected by the image band ranging between λ_1 and λ_2 .

e is a constant and equals to 2.718281828.

λ_1 is the beginning wavelength of a band of a remote sensor in μm

λ_2 is the end wavelength of a band of a remote sensor in μm

T_{thr} is the threshold radiant temperature in K

T_{bac} is the background radiant temperature in K

T_{fir} is the sub-pixel coal fire radiant temperature in K

Equation (20) shows the relation between the size and temperature of a sub pixel coal fire which can be detected by images with different range of bands.

For example, we have three data sets as listed in the first column in the Table 5.1. They are airborne data covering an area in Xinjiang, China, and all have a spatial resolution of 7.5m*7.5m. Through calculation we know their background temperatures (T_{Bac}), as well as their threshold temperatures for differentiating the full pixel coal fires (T_{Thr}). After we input these values into equation (20), and assign the sub-pixel coal fire with different radiant temperatures (T_{Fir}), the correspondent portion of the sub-pixel coal fire (P) can be calculated and plotted as illustrated in Figure 5.4.

Data	T_{Bac} (°C)	T_{Thr} (°C)
Nighttime 8-12.5 μ m data	15.9	18.6
Daytime 8-12.5 μ m data	28.9	33.3
Daytime 3-5 μ m data	28.9	36

Table 5.1: Description of three data sets

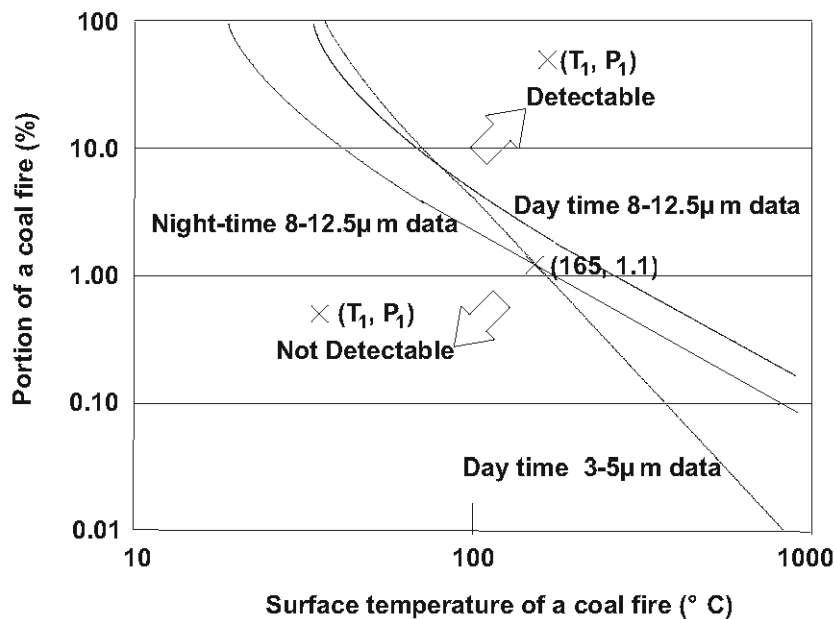


Figure 5.4: Threshold line of Temperature and portion for detecting a sub-pixel coal fire by different data sets.

Figure 5.4 shows the detection capability of the data sets. A sub-pixel coal fire, with a temperature of T_1 and P_1 portion of a pixel size, can be plotted in the figure. It can be detected when it is located in the upper-right part of the threshold line. Otherwise it is not detectable. The night-time 8-12.5 μm data curve crosses with the daytime 3-5 μm data curve at the portion of 1.1%, temperature of 165°C. For a sub-pixel coal fire with a radiant temperature lower than 165°C, the night-time 8-12.5 μm data have better detection capability than daytime 3-5 μm data. The 3-5 μm data have an increasing capability to detect a sub-pixel coal fires with higher ($>165^\circ\text{C}$) temperatures. High temperature coal fires contribute more significantly to the 3-5 μm data than to the 8-12.5 μm data.

Equation (20) can be used in another way for quantifying sub-pixel coal fires. Suppose the integrated temperature of an anomalous pixel in a data set (T_{II}) is known, as well as the background temperature. We want to know what the exact temperature of the sub-pixel coal fire is, and how much portion it occupies. Equation (18) can be used to set an equation by using T_{II} instead of T_{Thr} . The problem now is that there are two unknown variables (T_{Fir} and P) in one equation. But when the same sub-pixel coal fire form a thermal anomalous pixel in another image, the second equation can be set. For instance, we have a thermal anomaly pixel with temperature of 18.6°C in the night-time 8-12.5 μm data set. The same pixel shows 36°C in the day time 3-5 μm data set. Then we know that the sub-pixel has a temperature of 165°C and a spatial extension of $1.1\% * 7.5\text{m} * 7.5\text{m} = 0.6\text{m}^2$.

Chapter 6 THERMAL CHARACTERISTICS OF COAL FIRES

6.1 Thermal Characteristics of Simulated Coal Fires

To understand the characteristics of coal fires, an integrated controlled experiment of coal fires was conducted on 23rd and 24th of May 2002. The weather on 23rd was sunny and on 24th cloudy. Two coal fires, simulating both surface and underground coal fires, were ignited at 9:00 o'clock in the morning of the first day and kept continuously burning until 14:00 o'clock in the afternoon of the second day. An aeroplane equipped with the Advanced BIRD Airborne Simulator (ABAS) sensor for detecting and quantifying thermal anomalies passed over the test area 17 times at different flight heights. The ABAS sensor is an airborne sensor, which has the same configuration as the satellite sensor BIRD (Oettl, 2003). A spectrometer, named MIROR was placed on an observing tower for acquiring the data to determine the gas content of coal fire plumes. Additionally, a Raytec MP 50 Line Scanner, mounted on an observation tower, was tested for the recording of radiant temperatures of the fires. The fires were measured on the ground using thermometers. This paragraph concentrates on the thermal characteristics of the simulated coal fire.

6.1.1 Setting of the experiment

The experiment was located on the site of DLR, Oberpfaffenhofen, Germany. As shown in Figure 6.1, an observation tower is located in the center of the northern part of the test site. Equipment was placed on the second floor, which is about 10 meters above the ground. A concrete path with railway tracks separates the test site into two parts: the eastern part and the western part. Both parts were covered by green grass with a height of 50cm. We refer to it as 'high grass'. The simulated underground coal fire was located in the eastern part and the simulated surface coal fire was located in the western part. They were 25m away from the tower and 2m away from edges of the concrete path. Around the fires, the grass was cut to 10cm height. We refer to this second grass type as 'low grass' (See Figure 6.2).

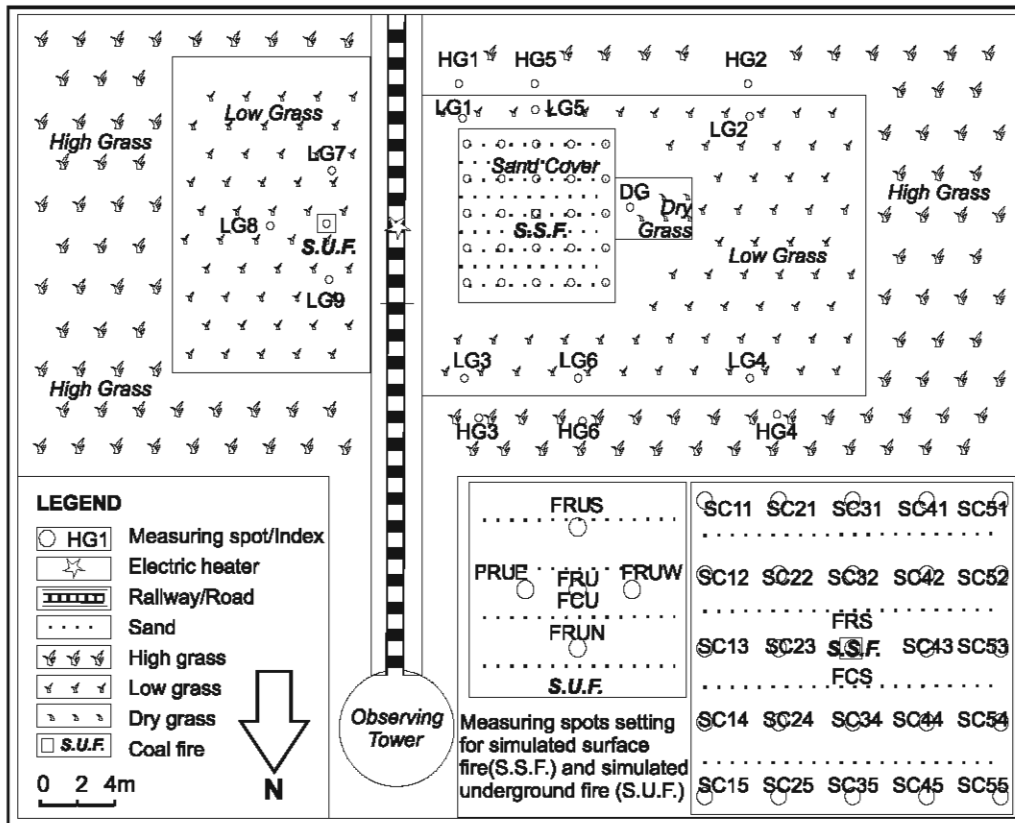


Figure 6.1 Map of test site at DLR, Oberpfaffenhofen

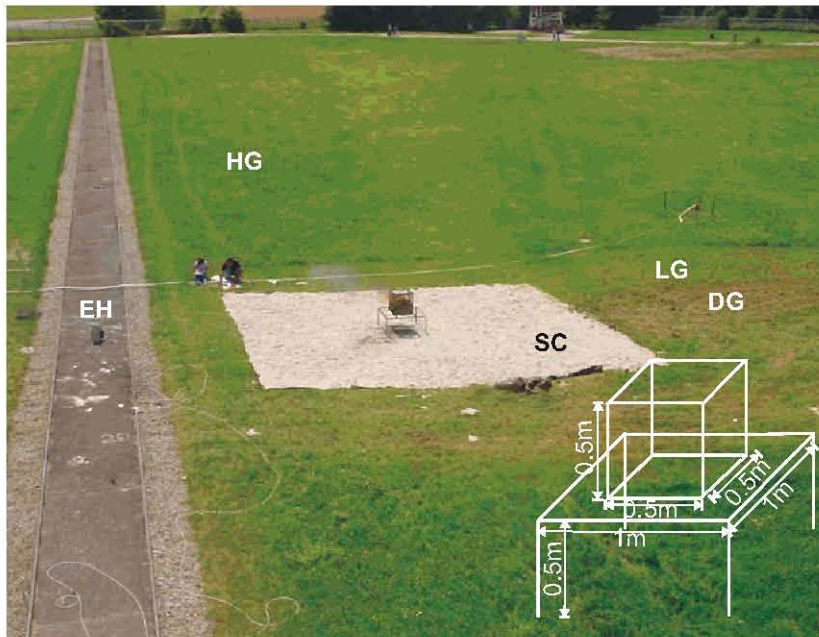


Figure 6.2 Setting of the Simulated Surface Coal Fire. HG: High grass; LG: Low grass; DG: Dry grass; EH: Electric heater; SC: Sand cover. Drawing in the lower right shows the dimension of the grill. The sand cover occupies an area of 8.5m*8.5m.

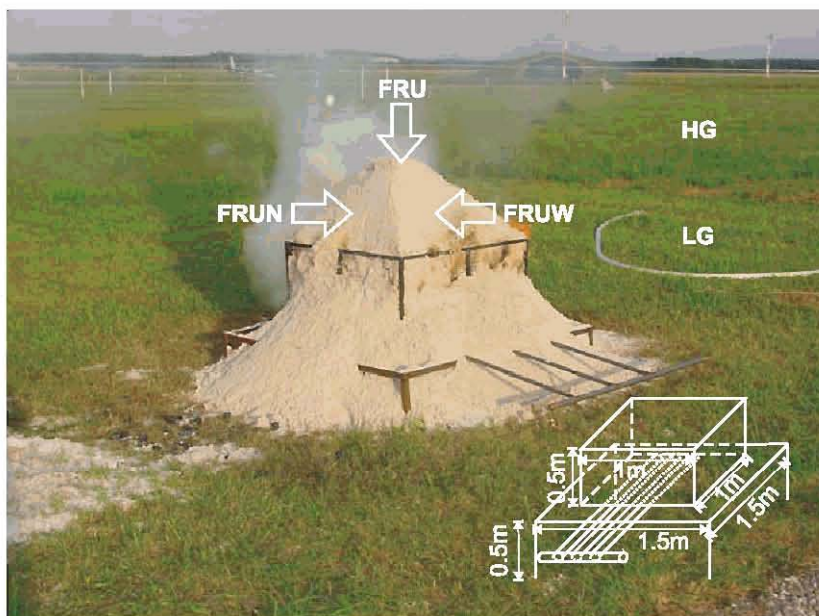


Figure 6.3 Setting of the Simulated Underground Coal Fire. HG: High grass; LG: Low grass. Drawing in the lower right shows the dimension of the grill. Arrows point on the measuring spots for FRU, FRUN and FRUW.

The simulated surface fire was ignited in a metal wire container with dimensions of 0.5m length, 0.5m width and 0.5m height. The container was fixed on a base supporter with a dimension of 1m length, 1m width and 0.5m height. The container was constructed using thermal resistant material and was perforated to provide optimal air ventilation (See Figure 6.2). An underground coal fire was simulated by covering a coal fire by a sand cone. The simulated underground fire was held in a similar container with dimensions of 1m length, 1m width and 0.5m height (See Figure 6.3). The size of the container is four times as big as the one for simulating the surface fire. The big container could hold more coal, which could not only make the fire strong enough to not be extinguished by the sand cone, but also to make the fire last long enough for the measurement cycle. The underground container had an extra ventilation system, which are perforated tubes at the bottom of the box. These three tubes were 2.5m long. They could transport air from outside the covering sand cone into the covered coal. At 19:00 o'clock the fire was covered by a sand cone with a height of 0.5m. This happened 10 hours after the fire was ignited to ensure that the fire had a homogeneous temperature distribution.

A sand covered surface area with dimensions of 8.5m x 8.5m was placed on the western part of the test site to simulate a homogeneous environment. The sand was white quartz sand with a particle diameter of 0.1-0.5mm, which was the same sand as that forming the underground coal fire sand cone. The thickness of the sand cover was about 4cm. The surface fire container was placed in the center of this sand area (See Figure 6.2). An electrical heater was placed in the middle of the two rail tracks. It was 25 meters away from the observing tower and supplied a thermal calibration for the Raytec MP 50 Line Scanner.

6.1.2 Data acquisition

During the experiment, the ABAS sensor took airborne IR images of the test site. The spectrometer MIROR and the Raytec MP 50 Line Scanner took images of the fires from the observation tower. The temperatures of the fires and background were also measured on the ground. The ABAS sensor was flown over the test site 17 times at 14:28-15:13, 05:41-06:23 and 07:57-08:31 respectively. The spectrometer MIROR

observed the simulated underground fire before and after it was covered by the sand cone. The Raytec MP 50 Line Scanner recorded temperatures of the fire areas 31 times between 14:20-20:37 on the first day and 62 times between 05:33-13:05 on the next day. Ground temperature measurements were acquired using a contact thermometer and a radiant thermometer. The contact thermometer has three components: a thermal sensor, a connecting cable and a digital reading board. When the thermal sensor is put in a fire, the reading board gives a value of the temperature of the fire. It had been used for measuring the temperature inside the simulated surface fire and the simulated underground fire. The radiant thermometer is designed like a gun. When one points it on a target, one can see a red laser marker on the target, and can get readings of the radiant temperature for the red laser marked area. It had been used for measuring the surface radiant temperature of the simulated surface fire, the simulated underground fire, high grass, low grass, dry grass, and the sand cover area. Figure 6.1 shows locations of measuring spots and their correspondent indexes using the radiant thermometer during the experiment. After the simulated underground fire was covered by the sand cone, it had 6 measuring spots located on the top of the sand cone (index: FRU), the center of the fire measured by a contact thermometer (index: FCU), and centers of 4 cone slopes facing to the North, East, South and West (index: FRUN, FRUE, FRUS, and FRUW). High grass had 6 measuring spots (index: HG1-HG5). Low grass had 9 (index: LG1-LG9) and Dry grass had one (index: DG). In the sand cover area, there were 25 measuring spots (index: SC11-SC55), which were evenly distributed in the area with a distance between two spots of 2 meters. The center spot was the simulated surface fire. Each spot was marked by a stick made from green paper to make sure that measurements were taken from the same point. Working sheets including the drawing of the measuring spots were prepared in advance to save writing time. Ground temperature measurements were acquired each hour from 11:00 to 14:00 of the next day. During ABAS overpasses the ground temperature measurements of the sand cover area were taken at 5 measuring spots instead of 25 measuring spots because of time limits. Ground temperature measurements of the coal fire experiment are shown in Appendix 1.

6.1.3 Results

1. Temperature of coal fires and their thermal anomalies

The temperature inside the simulated surface fire (FCS) was measured 10 times by using the contact thermometer between 11:00-19:00. The maximum temperature measured was 1080°C. The minimum was 880°C. The mean temperature was 983°C. The standard deviation was 64. Temperature inside the simulated surface fire was independent upon the air temperature (correlation factor 0.065).

Surface radiant temperature for the simulated surface fire (FRS) had been measured 34 times using the radiant thermometer between 11:00 on the 23rd -13:00 of the following day. Within these 26 hours, the maximum temperature measured was 900°C. The minimum was 309°C. The mean temperature was 640°C. Radiant temperature of the simulated surface fire could change up to 250°C within one measurement. Radiant temperature for some parts of the fire was 650°C, while at the same time, for other parts it was 900°C. The surface radiant temperature of the simulated surface fire was also dependent on the inside fire temperature. Their correlation factor was 0.68.

The simulated surface fire was moved away from its original place 4 times during the experiment at the time of 14:47, 14:59, 06:01 and 08:11. The radiant temperature of the sand on the fire spot was measured just a few seconds after the fire was moved, which were 49, 34, 45 and 98°C. The correspondent air temperatures (AT) were 26.3, 28.8, 15.2, and 17.2°C. Measurements at 14:47 and 14:59 showed that the temperature of the thermal anomaly formed by the surface fire drops rapidly when the surface fire was moved away.

After the simulated underground fire was covered by the sand cone, temperature inside it (FCU) had been measured 10 times using the contact thermometer from 19:00 to 05:00 of the next day. The minimum temperature measured was 842°C. The mean temperature was 954°C. The standard deviation was 112. During the last measurement, the thermal sensor melted and the thermometer broke. The melting temperature of the thermal sensor is 1200°C, which means that temperature inside the simulated underground fire reached over 1200°C.

The surface radiant temperature of the 5 measuring spots (FRU, FRUN, FRUE, FRUS, and FRUW) for the simulated underground fire was measured 11 times using the radiant thermometer from 19:15 to 04:45 of the next day. The results are shown in Figure 6.4. It can be seen that at 19:15, which is just a few seconds after the sand cone had been built, the top measuring spot of the sand cone (FRU) had a 3.5°C lower temperature than the maximum temperature of the background. Here we use the four corner measuring spots SC11, SC15, SC51, and SC55 of the sand cover (See Figure 6.1) as the background. After 35 minutes, at 19:50, it had a 1.5°C higher temperature than the maximum temperature of the background. This high temperature could be considered as a thermal anomaly of the coal fire. The thermal anomaly had a temperature ranging 1.5 to 4.2°C higher than the maximum temperature of the background. The average is about 3°C. The reason that the thermal anomaly was formed so rapidly is that the sand cone had a high porosity, which favours air ventilation and heat transfer through convection. The highest temperature difference of 6.7°C between the fire thermal anomaly and the background maximum happened at 03:45 due to a collapse of a cone slope. Radiant temperatures for measuring spots FRUN, FRUE, FRUS, and FRUW showed higher values than that of the top measuring spot FRU, because they were closer to the fire. Temperatures for FRUE, FRUS, FRUW showed big variances. They ranged from 20 to 50°C. Heat coming from the side of the fire container influenced the measurements.

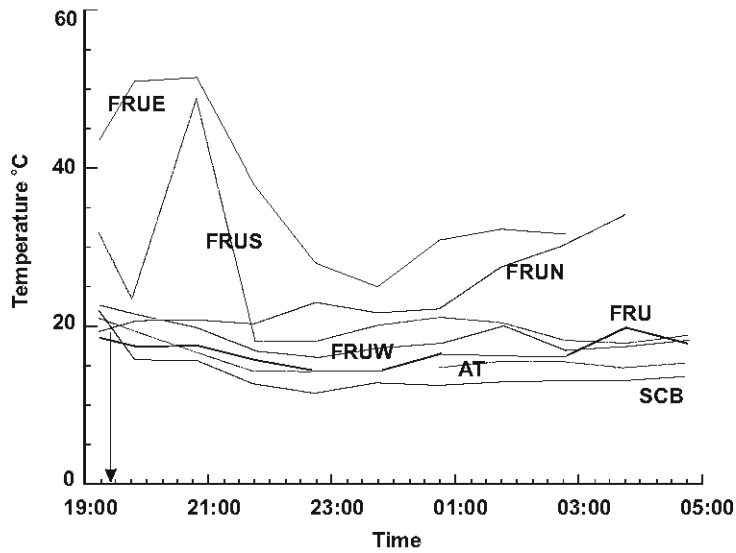


Figure 6.4 Surface Temperature of the Simulated Underground Coal Fire. FRUN: Radiant temperature measured at the center of the North Slope of the sand cone; FRUE: East slope; FRUS: South slope; FRUW: West slope; FRU: Top; AT: Air temperature; SCB: Background temperature for sand cover. From 19:30, the temperature of the background was the lowest. Heat from the fire transferred to the top of the sand cone within one hour. The top of the sand cone is warmer than the background by an average temperature of 3°C.

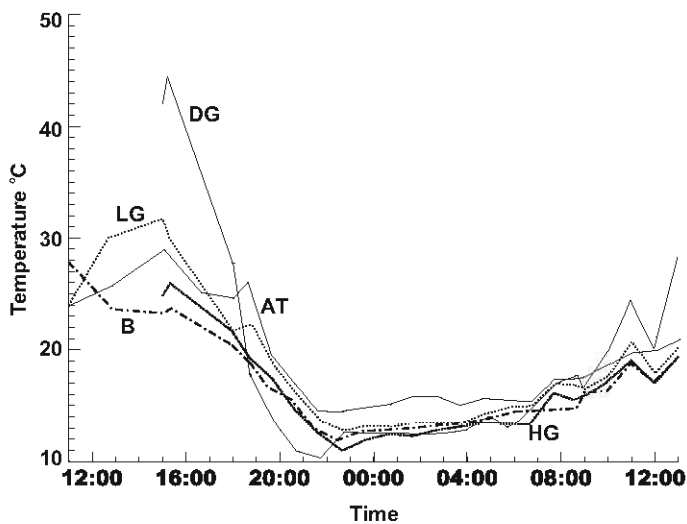


Figure 6.5 Diurnal Radiant Temperature Variations for Background Materials. AT: Air temperature; B: Background; HG: High grass; LG: Low grass; DG: Dry grass. They show the same trend: High radiant temperature during daytime and low temperature during night-time.

2. Temperature of background materials

Figure 6.5 shows diurnal radiant temperature variations for high grass, low grass, dry grass, and sand cover. Data on diurnal changes in radiant temperature for these materials are calculated from the averages of all measurements. Background temperatures result from the average measurements of the sand cover. The most rapid temperature changes, shown by steep curves, occur near dawn and sunset. Low grass showed always warmer than high grass. Dry grass showed cooler than low grass in night-time, but warmer than low grass in daytime. The curve for radiant temperature of the sand cover is located between the curves for high grass and low grass during night-time. During daytime, high grass and low grass are warmer than the sand cover (with one exception). During day time, the temperature difference among these background materials is high. But in night-time, the difference is low. The curves for all these materials have the same trends. The correlation between air temperature and the sand cover is 0.90. The correlation factor between sand cover and low grass is 0.92. Between high grass and low grass it is 0.98.

3. Temperature distribution of the sand cover

The sand cover can be considered as a homogenous area. In this 8.5m*8.5m area, 25 measuring spots (SC11-SC55) were set (See figure 6.1). Radiant temperatures for these observing spots were measured every hour during the experiment. According to the distance to the fire, these measurements were grouped into 5 groups. Group I includes the measuring spots SC32, SC23, SC43, and SC34, which were 2 meters away from the center of the fire. Group II includes the measuring spots SC22, SC42, SC24, and SC44, which were 2.8 meters away from the center of the fire. Group III includes SC31, SC13, SC53, and SC35. They were 4 meters away from the center. Group IV includes SC12, SC21, SC41, SC52, SC54, SC45, SC25 and SC14. They were 4.5 meters away from the center. Group V includes 4 corner spots (SC11, SC15, SC51 and SC55). They were 5.6 meters away from the center. Diurnal mean radiant temperature variations for these five groups are shown in Figure 6.6. Radiant temperature differences between one group and its following group were calculated. It can be seen that the radiant temperature for group one was always higher than that for

other groups. From 18:00 to 13:00 the next day the radiant temperature for group 2 was higher than that for group 3, 4 and 5. From 16:30 to 09:00 the next day the radiant temperature for group 3 was higher than that for group 4 and 5. The diurnal radiant temperature for group 4 was almost the same as that for group 5. This can be interpreted following. The simulated surface coal fire can heat the surroundings through radiation and convection in a proximate distance of 2 meters and form a 1°C difference thermal anomaly (2 measurements out of 21 were smaller than 1°C). It is hard for the coal fire to heat a distance further away than 4.5 meters. Group 4 and group 5 can be considered as background. The heating extent of the fire can some times reach 2.8 or 4 meters and form a thermal anomaly with temperature difference less than 1°C. Figure 6.7 shows diurnal maps of radiant temperatures for the sand cover. To generate the radiant temperature maps, the coal fire radiant temperature located in the center of the map (FRS) was replaced by the maximum value from the other 24 measurements (SC11-SC55). The maps indicate the thermal anomalous pattern formed by the coal fire. The axis of the high values shows the dominant heat transfer directions. Probably caused by wind influence, the dominant heat transfer directions varied to almost all directions. Although the radiant temperatures are higher when the measuring spots are closer to the fire, the pixels close to the center never formed a perfect circle. A thermal anomaly is formed not through radiation, but by heat convection.

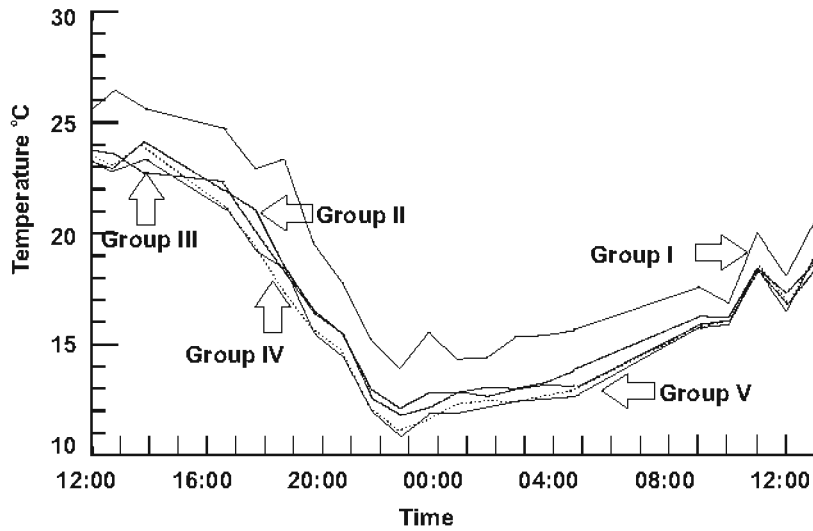


Figure 6.6 Diurnal Radiant Temperature Variations for Measurements with Different Distance to the Coal Fire. Group I: Measuring spots 2 meters away from the fire; Group II: 2.8 meters; Group III: 4 meters; Group IV: 4.5 meters; Group V: 5.6 meters. Thermal anomalies caused by the fire can not reach further than 4.5 meters.

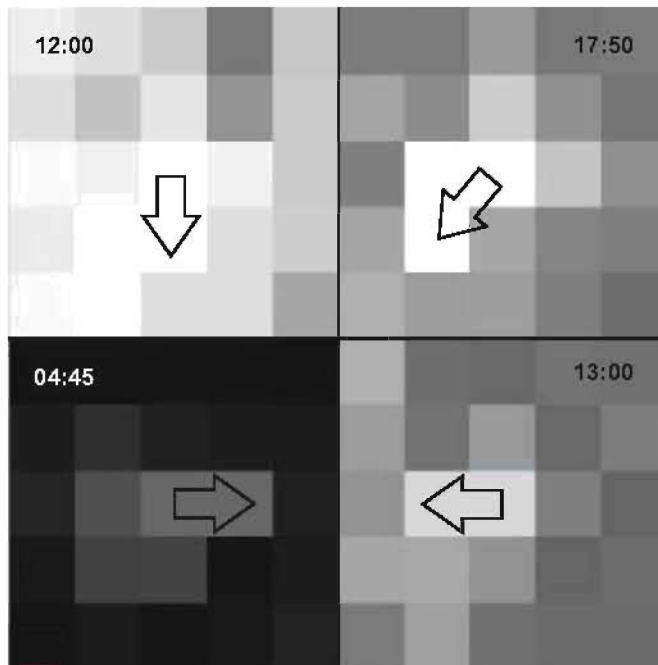


Figure 6.7 Diurnal Maps of Radiant Temperatures for the Sand Cover. Arrows indicate the main heat transfer directions. They change to every direction.

4. MP 50 line scanner images of coal fires

The MP 50 line scanner is a stationary scanner. The radiation transmitted through an IR filter is focused onto a detector that converts the radiation into an electric signal. The resulting image records radiant temperature for targets in decimal degrees. A pixel will be saturated at 300°C. The MP 50 line scanner was set 25 meters away from the fires and 10 meters above the ground. The resulting images have a spatial resolution of 5cm. Figure 6.8 shows a series of the MP 50 line scanner images acquired at 14:34, 20:29, 05:33 the next day, 08:01 the next day, 11:01 the next day, and 13:05 the next day. The images cover an area of the simulated underground coal fire and its surroundings, including the electric heater that served as a standard thermal emission source with a certain fixed temperature. The simulated underground coal fire was covered by the sand cone from 19:00 to 08:30 of the next day, which is shown in image II, III, and IV in Figure 6.8. Image I, V, and VI in Figure 6.8 show the fire not covered by the sand cone. Both fire and electric heater pixels were saturated. The fire formed a thermal anomalous cluster occupying a lot of pixels in all images. The thermal anomalous cluster was so outstanding that it could be easily separated from the background. The data can be used for further analysis of the fire when they are corrected.

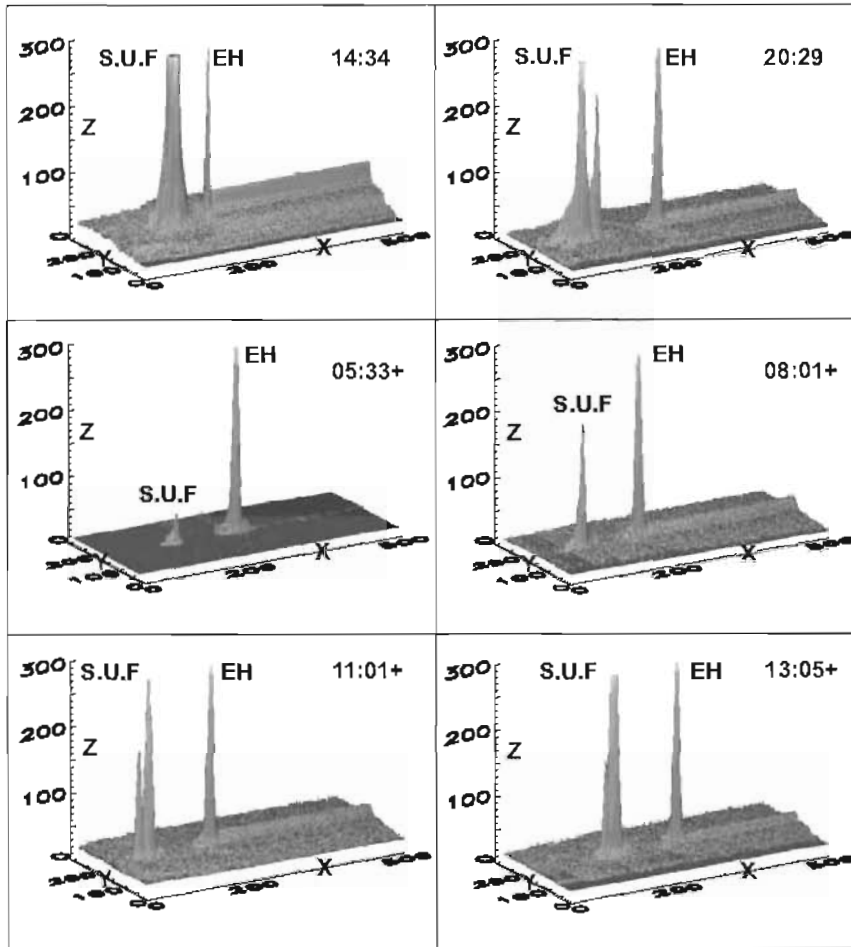


Figure 6.8 MP 50 line scanner Images. X: Rows; Y: Columns; Z: Temperature (°C); S.U.F.: Simulated underground coal fire; EH: Electric heater. The coal fire with a dimension of 1m*1m forms an outstanding thermal anomalous cluster in MP 50 line scanner images, whose spatial resolution is 5cm.

6.1.4 Conclusions

1. The interior temperature for the simulated surface coal fire is about 1000°C. For the simulated underground coal fire, the interior temperature could reach above 1200°C. The surface radiant temperature for the simulated coal fires range from 300 to 900°C. Within 1 hour heat could be transported through a 0.5 meter high sand cone to the surface and form a thermal anomaly with a temperature about 3°C higher than that of the background.

2. Diurnal radiant temperature variations for high grass, low grass, dry grass, and the sand cover showed the same trend. During day time, the temperature difference among these background materials is high. But in night-time, the difference is low.
3. The simulated surface coal fire can heat the surroundings through radiation and convection in a distance of approximately 2 meters and form a 1°C difference thermal anomaly. It is hard for the coal fire to form thermal anomaly further than 4.5 meters. The influence distance of the fire is dependent on its temperature. Heat from the simulated surface fire was transported mainly by convection, not radiation. Main heat transfer directions vary all the time.
4. The coal fire with a dimension of 1m*1m forms outstanding thermal anomalous clusters in MP 50 line scanner images, whose spatial resolution is 5cm.

6.2 Thermal Characteristics of Coal Fires in the Study Areas

In September 2002, a field campaign was conducted in the Wuda coal mine area, the Gulaben coal mine area, Inner Mongolia, and the Ruqigou coal mine area, Ningxia Hui Autonomous Region, China. The aim of the fieldwork was to understand thermal characteristics of coal fires in the field. Surface temperatures for materials related to the coal fires were measured using a Raytec thermometer and contact thermometers. The time mentioned in this paragraph is Chinese Coast time (CCT, Time Zone 8), which is equal to Greenwich Mean Time plus 8 hours (GMT + 08:00).

6.2.1 Field surface temperature measurements of a sand dune

A sand dune, located at the southern part of Coal Fire No.8 in Wuda coal mine area, was chosen as background for studying the daily temperature amplitude. Figure 6.9 shows that the sand dune consists of fine yellow sand. There are bushes growing on it, most of which are dry shrubs. The sand dune is about 2 meters high. From the northern edge to the southern edge, the distance is about 8m. From East to West, the distance is about 7m. Two measuring lines were marked on the surface of the sand dune. One is from North to South. The other is from West to East. They cross each other on the top of the sand dune. From North to South, there were 16 measuring points, named N1-N8, T and S1-S7. From West to East, there were 14 measuring points, named W1-W7, T

and E1-E6. Measuring point T represents the top of the sand dune. The measuring points were evenly distributed along measuring lines on the surface. Chopsticks with white plastic flags were used for marking all the measuring points to make sure that every time the measurements were taken in the same spots. Measuring points N1, S7, W1, E5 and E6 were located at the flat area around the sand dune as shown in the cross sections in Figure 6.9. The coordinates for the top of the sand dune are 639403, 4373774 (UTM, Zone 48). The dip angle for the slope of the sand dune ranges from 30 to 40 degrees.

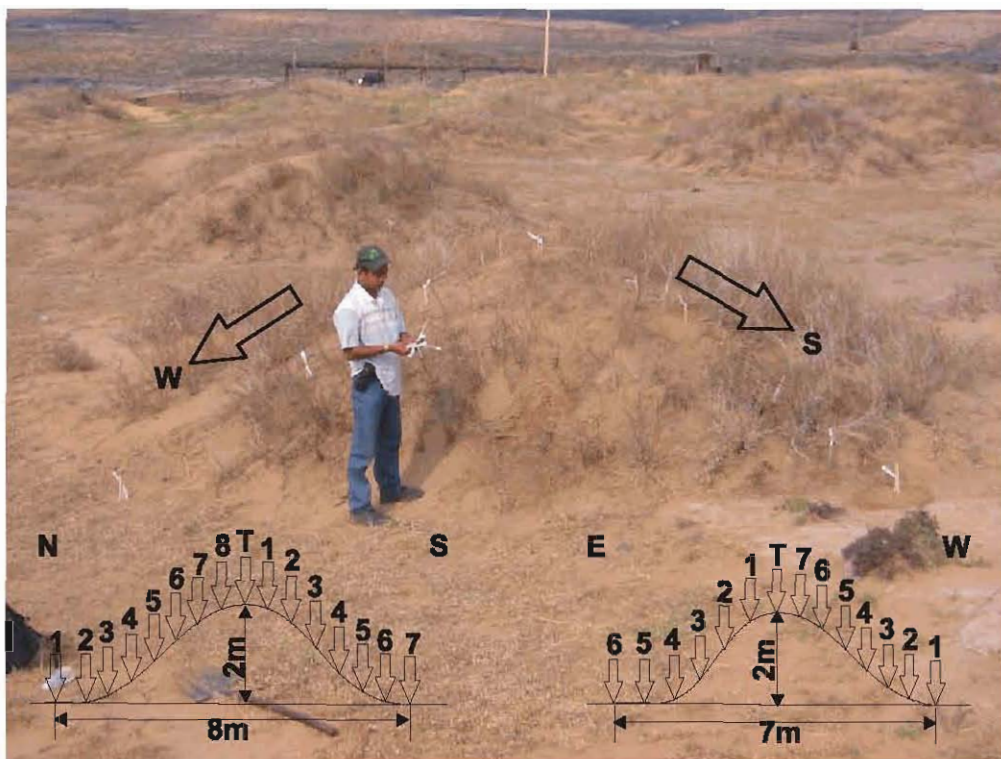


Figure 6.9 Setting of measuring points on a sand dune in Wuda coal mine area. N: North; E: East; S: South; W: West; 1-8, T: measuring points. The drawings show the cross section of the sand dune from North to South and East to West.

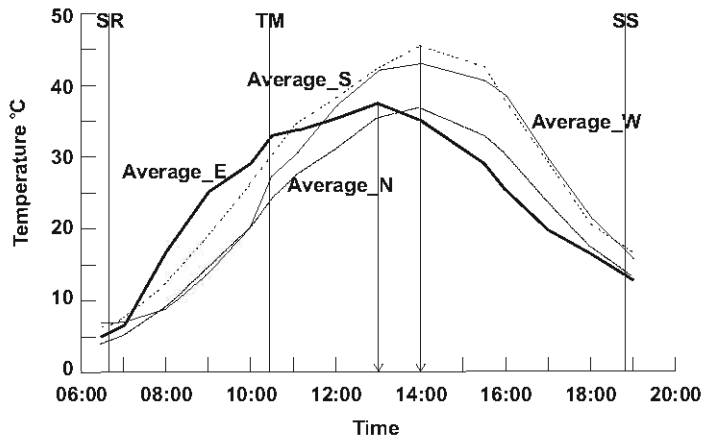


Figure 6.10 Average surface temperatures for slopes facing to North, East, South and West of a sand dune in Wuda coal mine area. Average_N: average of temperature measurements for measuring points N1-N8 and T; Average_E: average of measuring points E1-E6 and T; Average_S: average of S1-S9 and T; Average_W: average of W1-W9 and T; SR: sunrise; SS: sunset; TM: TM overpass. The slope facing to the East reaches its highest temperature at 13:00. The slope facing to the North, South and West reach their highest temperatures at 14:00.

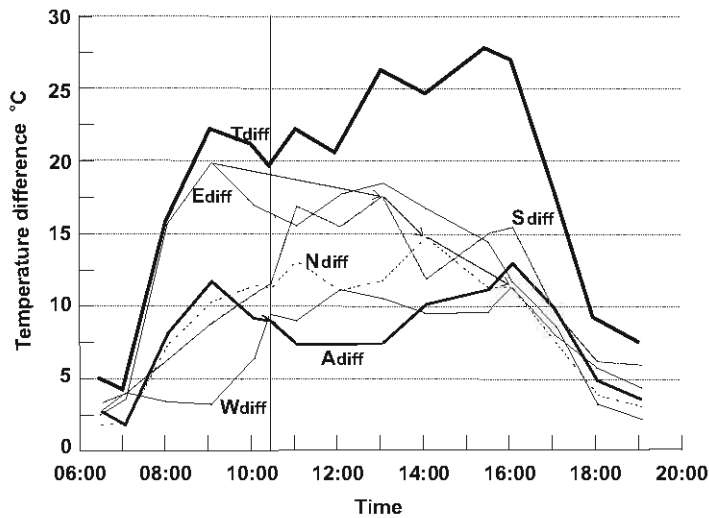


Figure 6.11 Surface temperature variance of a sand dune in Wuda coal mine area. Ndiff, Ediff, Sdiff, Wdiff: temperature variance within a slope facing to the North, East, South and West; Adiff: average temperature variance among slopes; Ediff: temperature variance in the sand dune. Arrows point on the maximum values of the temperature variances within east, south, north and west slopes. Temperature measurements could vary 28°C in a sand dune.

Surface temperatures for each measuring point were recorded every hour on the sunny day of 23rd September 2002. The measurements started at 06:30 before the sunrise (06:41) and ended at 19:00 after the sunset (18:53). The records are shown in Appendix 6.2: Surface temperature measurements for a sand dune in Wuda coal mine area, Inner Mongolia, China.

Figure 6.10 shows plots of the average temperatures for measuring points N1-N8 plus T (average_N), E1-E6 plus T (average_E), S1-S7 plus T (average_S), and W1-W7 plus T (average_W). For example:

$$average_E = \overline{T_E} = \frac{T_{E1} + T_{E2} + T_{E3} + T_{E4} + T_{E5} + T_{E6} + T_T}{7}$$

where,

average_E: average temperature for East slope

T_{E1} to T_{E6} and T_T : Temperatures for the measuring points E1 to E6 and T

They represent the surface temperature changes between 06:00 to 19:00 for the slope facing to the North, East, South and West respectively. At 6:30 before sunrise, surface temperatures for each slope show their minimum value ranging from 4 to 8°C. Temperatures for the slope facing to the East increase from sunrise until 13:00 and then decrease again. The other slopes reach their highest temperature at 14:00. From 07:15 to 11:00, average temperature for the eastern slope is higher than that for other slopes. From 11:00 to 16:00, average temperature for the southern slope is higher than that for other slopes. From 16:00 to 18:30, average temperature for the western slope has the highest value.

Figure 6.11 shows surface temperature variance in the sand dune. Firstly, the temperature difference within a slope is calculated as the result of the maximum value for the measurements within the slope minus the minimum value for the measurements within the slope. For example, for the slope facing to the East:

$$E_{diff} = Max(T_{E1}, T_{E2}, T_{E3}, T_{E4}, T_{E5}, T_{E6}, T_T) - Min(T_{E1}, T_{E2}, T_{E3}, T_{E4}, T_{E5}, T_{E6}, T_T)$$

Where,

E_{diff} : Temperature difference within the eastern slope

T_{E1} to T_{E6} and T_T : Temperatures for the measuring points E1 to E6 and T

From 07:15, temperature difference within the eastern slope is higher than 5°C. It reaches its highest value of 20°C at 09:00. From 07:30, temperature difference within the southern slope is higher than 5°C. The same applies for the northern slope. Temperature difference within the southern slope reaches its highest value of 16°C at 13:00, the northern slope 14°C at 14:15. From 09:30, temperature difference within the western slope is higher than 5°C. It reaches its highest value of 12°C at 16:00. Temperature variances within slopes facing to the East, South, North and West show the trend that the maximum value is declining and the time for the maximum value is shifting to a late time.

Secondly, temperature difference among slopes A_{diff} is calculated from the following equation:

$$A_{diff} = \text{Max}(\overline{T_N}, \overline{T_E}, \overline{T_S}, \overline{T_W}) - \text{Min}(\overline{T_N}, \overline{T_E}, \overline{T_S}, \overline{T_W})$$

From 07:30 to 18:00, average temperature difference among slopes is higher than 5°C. The maximum value of 13°C occurs at 16:00. A_{diff} reaches two peaks at 09:00 and 16:00 due to the slopes facing to the East and West. At 09:00, the eastern slope has a high average temperature and the western slope has a low one. At 16:00, the western slope has a high average temperature and the eastern has a low one.

Thirdly, temperature variance in the sand dune T_{var} is calculated using the maximum value of all the measurements minus the minimum value of all the measurements.

$$T_{var} = \text{Max} (T_{N1}, \dots, T_{N8}; T_{E1}, \dots, T_{E6}; T_{S1}, \dots, T_{S7}; T_{W1}, \dots, T_{W7}; T_T) \\ - \text{Min} (T_{N1}, \dots, T_{N8}; T_{E1}, \dots, T_{E6}; T_{S1}, \dots, T_{S7}; T_{W1}, \dots, T_{W7}; T_T)$$

Where,

T_{var} : Temperature variance in the sand dune

T_{N1}, \dots, T_T : Temperatures for measuring points correspondent with the index.

Just about 20 minutes after sunrise, temperature variance in the sand dune is higher than 5°C. It has its highest value of 28°C at 15:30 (measuring point S3 reaches 49°C while the temperature for E4 is only 21°C).

Temperature variances among measurements in the sand dune are due to the characteristics of the measuring points. Some of them are exposed to the sun, while some of them are shaded by vegetation. At 10:30, when the TM (ETM+) passes over the area, the temperature difference within the sand dune can reach 20°C, which is more than the temperature difference between the coal fire thermal anomalies and the background. This is very important to consider when aiming at the daytime extraction of thermal anomalies.

6.2.2 Field surface temperature measurements of a coal dump pile

Coal dumps are a kind of mining waste, most of which are black shale or mud stone originally embedded in coal layers. Surface temperatures for a coal dump pile were measured on the same day as the sand dune (Data are shown in Appendix 6.3: Surface Temperature Measurements for a coal dump pile in Wuda Coal Mine Area, Inner Mongolia, China). The top coordinates of the coal dump are 639460, 4373881 (UTM, Zone 48N). It is located 120 m away from the sand dune in NNE direction. Figure 6.12 shows that the coal dump pile is about 2 m high and slope angles are about 35°. Three measuring points were set on the slopes facing 350°. They represent temperatures for the lower part (measuring point NL), middle part (measuring point NM) and upper part (measuring point NU) of a coal dump pile slope facing north. Another three measuring points were set on the slope facing 135°. They represent temperatures for the lower part (measuring point SEL), middle part (measuring point SEM) and upper part (measuring point SEU) of a coal dump pile slope facing southeast. Temperature measurements for the measuring points are shown in Figure 6.13. So is the temperature difference between the maximum value and the minimum value (Max (NL, NM, NU, SEU, SEM, SEL) – Min (NL, NM, NU, SEU, SEM, SEL)). At 06:50, which is 9

minutes after sunrise, temperatures for all the measuring points are close to each other. The difference between the maximum value and the minimum value is 1.6°C. From 7:15 to 17:00, temperature measurements for the SE slope are higher than that for N slope. From 10:00 to 14:00, the maximum measurement for the SE slope is over 20°C higher than the minimum measurement for the N slope. TM (ETM+) overpass time (10:30) is included in this time range. Temperature measurements for all 6 measuring points changed within 5°C in the time range before 07:00 and after 17:30.

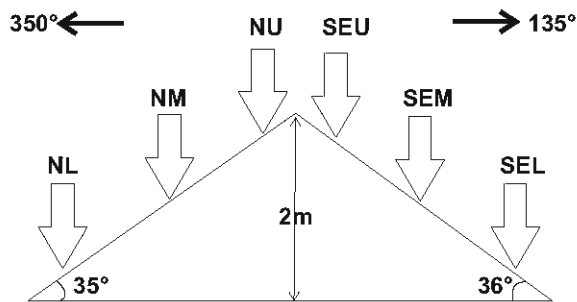


Figure 6.12 Setting of measuring points on a coal dump pile in Wuda coal mine area. NL, NM, NU, SEL, SEM, and SEU: measuring points; 350° and 135°: slope dip direction.

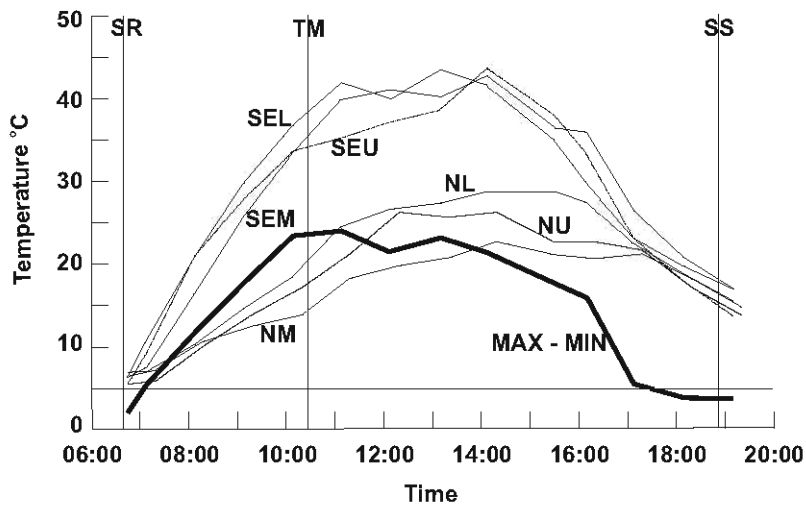


Figure 6.13 Surface temperatures and their variance for a coal dump pile in Wuda coal mine area. NL, NM, NU, SEL, SEM, and SEU: temperature for the correspondent measuring point; SR: sunrise; SS: sunset; TM: TM overpass. MAX-MIN: temperature variance.

6.2.3 Field temperature measurements of cracks

A crack, 30 meters north of the sand dune, was chosen as coal fire related thermal anomaly for studying surface temperature changes during a day. The crack is about 3m long, 40cm wide and 2m deep. It strikes to the NW. At the bottom of the crack, the coal fire is burning; a red flame can be seen. The bedrock around the crack is covered by the same yellow fine sand forming the sand dune. A NE trending measuring line was set as shown in Figure 6.14. From the crack to SW, there were 6 measuring points named SW1, SW2, SW3, SW4, SW5 and SW6. From the crack to the NE, there were 10 measuring points named NE1, NE2, NE3, NE4, NE5, NE6, NE7, NE8, NE9, and NE10. Chopsticks with white plastic flags were used for marking all the measuring points to make sure that every time the measurements were taken at the same spots. The coordinates for the measuring point NE10 are 639399, 4373749 (UTM, Zone 48). Surface temperatures for each measuring point were recorded in the same way on the same day as for the sand dune. The records are shown in Appendix 6.4: Surface temperature measurements for a crack in Wuda coal mine area, Inner Mongolia, China. The dip direction and dip angle for the surface plane, where the measuring points are located, are also shown in Appendix 6.4

The measurements show that between 06:30 to 19:00 the surface temperature of the fire at the bottom of the crack (measuring point C) has a highest temperature of 239°C and the lowest of 233°C, with an average of 237°C, and a standard deviation of 1.56. It is relatively stable during the day. From 06:30 to 14:00, temperatures for other measuring points increase from 6 °C to 43°C. Past 14:00 they decrease again.

The measuring points SW1, SW2, SW3, NE8, NE9 and NE10 are taken as background. The temperatures higher than the background are taken as thermal anomalies. Figure 6.14 shows that the width of the thermal anomaly is 3.8m, 3.8m, 3.8m and 4.1m at 07:00, 09:00, 11:00 and 13:00 respectively. This shows that the width of the thermal anomaly does not change as the background temperature increases. The maximum temperature difference between the crack and the background occurs predawn. The thermal anomaly does not extend more than 3m from the crack.

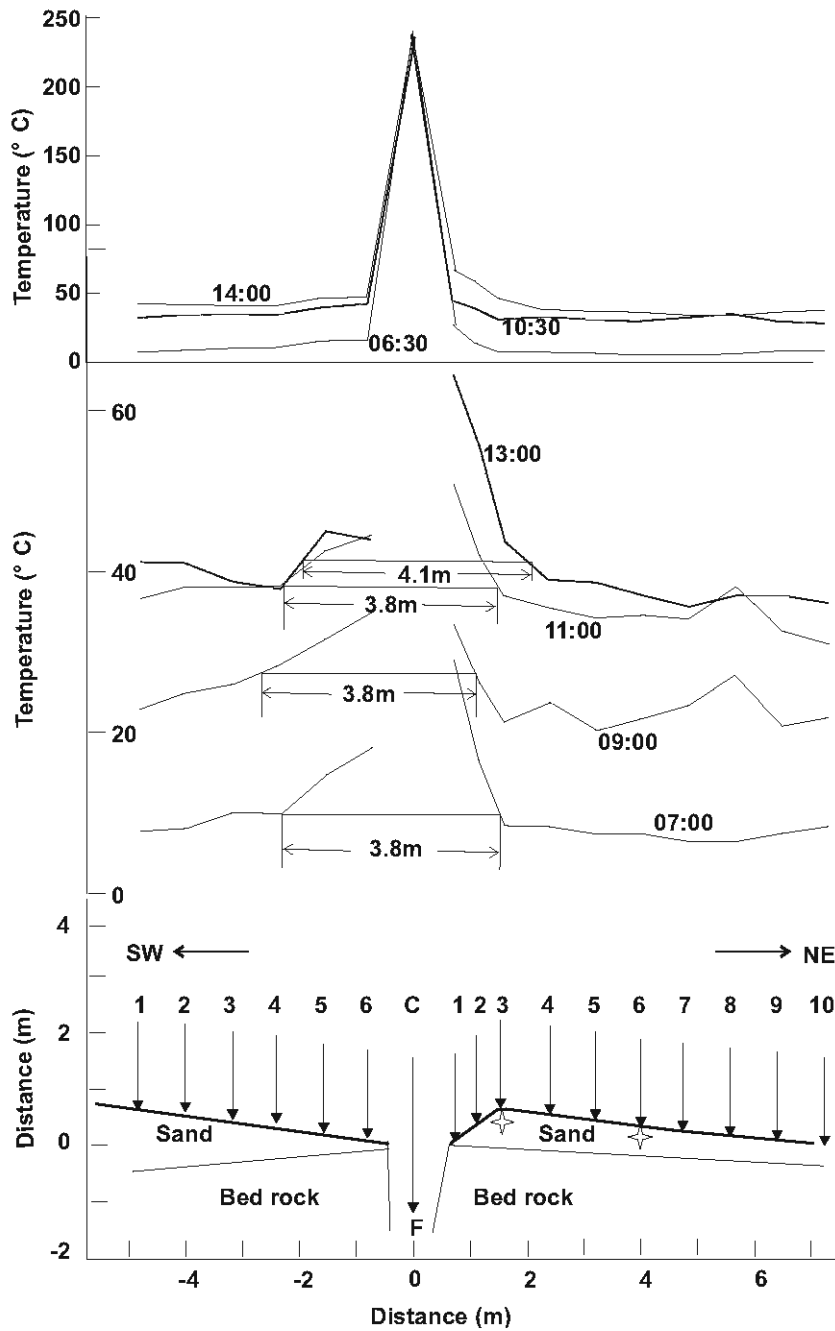


Figure 6.14 Surface temperatures for a crack in Wuda coal mine area. Lower: setting of measuring points; middle and upper: temperature profile. Temperature for the crack fire is relatively stable during the day. The thermal anomaly does not extend more than 3m from the crack. The width of the surface thermal anomaly does not decline as the background temperature increases.

Temperatures at different depths for measuring point NE3 and NE6 have been measured using a contact thermometer three times at 07:30, 09:30, and 11:30. The contact thermometer has a handle and a 12.8cm long probe looking like a screwdriver. It measures the temperature at the head of the probe. A mark was given at every quarter of the probe and then pressed into the sand until the mark. The readings on the handle represent temperatures below the surface at the depth correspondent to the mark. Measurements include the temperature on the surface, and 1cm, 3.2cm, 6.4cm, 9.6cm, 12.8cm below the surface as shown in Table 6.1 and Figure 6.15.

Measuring Point	NE3	NE6	NE3	NE6	NE3	NE6
Start Time	7:29	7:34		9:41		
Surface	10.1	12.7	26.2	28.7	38.3	35.7
-1cm	11.9	13.5	25.6	26.5	36	34.3
-3.2cm	19.5	16.7	24.6	22.5	32.1	28.7
-6.4cm	23.1	18.7	25	22	29.8	26.8
-9.6cm	26.0	21.0	26.7	22.2	29.9	25.9
-12.8cm	27.1	22.7	29.8	23.0	31.5	25.7
End Time		7:40	9:39		11:29	11:36

Table 6.1: Temperature (°C) for different depths at measuring points NE3 and NE6.

NE3 is about 1m away from the crack and NE6 is about 3.5m away from the crack as shown in Figure 6.14. Temperatures for 12.8cm below the surface at NE3 are 5-7 °C higher than that at NE6. The conduction of heat therefore does influence the near surface temperature. Its gradient is about 2.4 °C per meter.

At 07:30, temperatures from -12.8cm to the surface at both NE 3 and NE6 were decreasing. On the surface, according to the trend, temperature for NE6 is supposed to be lower than that for NE3, but the measurements show the opposite, which is due to uneven solar heating. The surface plane where NE3 is located is relatively flat. The surface plane where NE6 is located has a dip angle of 7 and dip direction of 50 (facing to NE). NE6 favoured to receive stronger solar heating in the morning. Only 1 hour past sunrise, a thermal anomaly formed 1m away from the coal fire crack was affected by solar uneven heating.

At 09:30, temperatures from -12.8cm to -3.2cm at NE3 decrease. Temperatures from -3.2cm to the surface increase. After 3 hours past sunrise, the heat from the sun reaches at least 3.2cm below the surface at NE3. Since NE6 receives more heat than NE3, heat reaches 6.4cm below the surface at the same time.

At 11:30, temperatures from -12.8cm to the surface at NE6 decrease. Heat from the sun at NE6 reaches at least 12.8cm below the surface. It reaches -6.4cm at NE3. On the surface, temperature for NE3 is higher than that for NE6, which is probably due to the SW wind, bringing the heat from the crack to NE3.

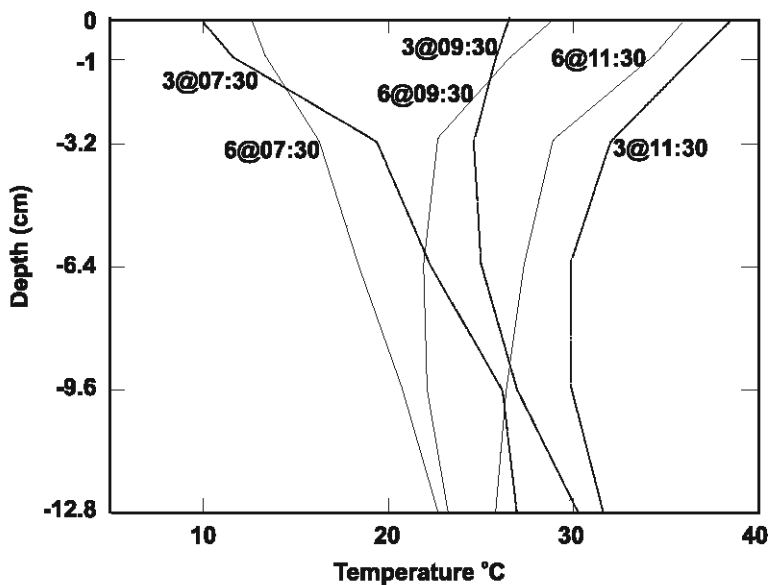


Figure 6.15 Underground temperature at measuring points NE3 and NE6. A@B: at measuring point A and time B. One hour after the sunrise, thermal anomaly to be formed 1m away from the coal fires crack was overprinted by the sun uneven heating. At NE3, heat from the sun reaches 3.2cm below the surface at 09:30 and 6.4cm at 11:30. At NE6, heat from the sun reaches 6.4cm below the surface at 09:30 and more than 12.8cm at 11:30.

Temperatures for another crack, located at coal fire No. 8 in Wuda coal mine area, were measured two times on September 10 and 14, 2002. Figure 6.16 shows that the crack is located in a brownish yellow sand stone layer. Its width is about 1m. The wide crack enabled to use a radiant thermometer to measure temperatures from the surface to the underground coal fire. Here a coal fire was burning 3m below the surface. A

vertical temperature profile for the crack is shown in Figure 6.16. The measuring points for the vertical profile were taken from the edge of the crack at spots: surface, 0.02, 0.5, 1, 2m below the surface, and the coal fire itself. The measurements for the coal fire were 850°C on Sep.10 and 854°C on Sep.14. Temperatures at 0.02m below the surface were 139°C on Sep.10 and 132°C on Sep.14. At 0.02m on the edge of the surface, temperatures dropped rapidly to 60 and 66°C. A horizontal temperature profile for the crack is shown in Figure 6.16. From the measuring point A to B, it was found that after 30cm the temperature measurements dropped to the normal background temperature.

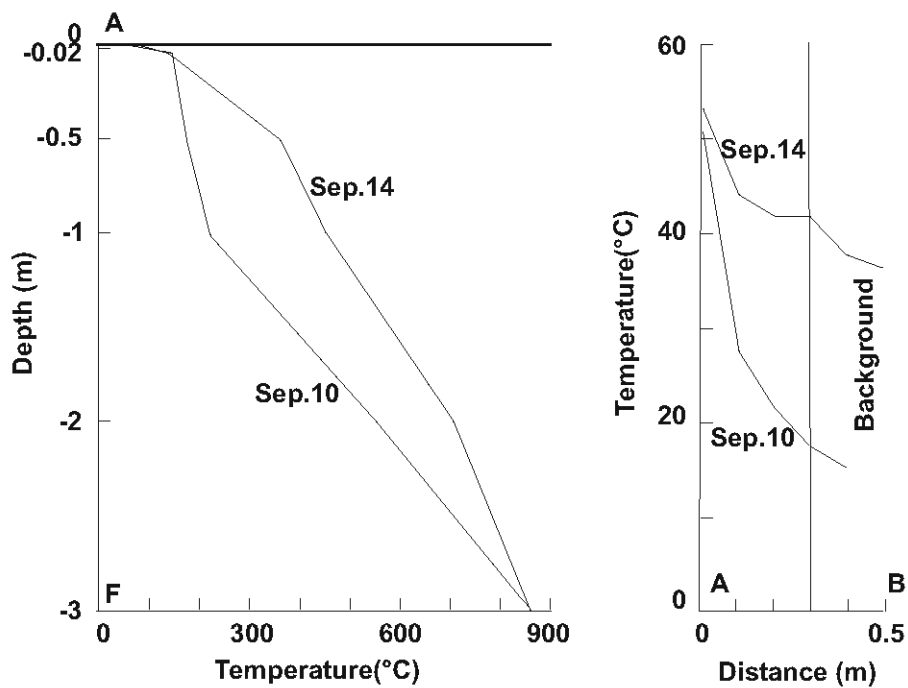
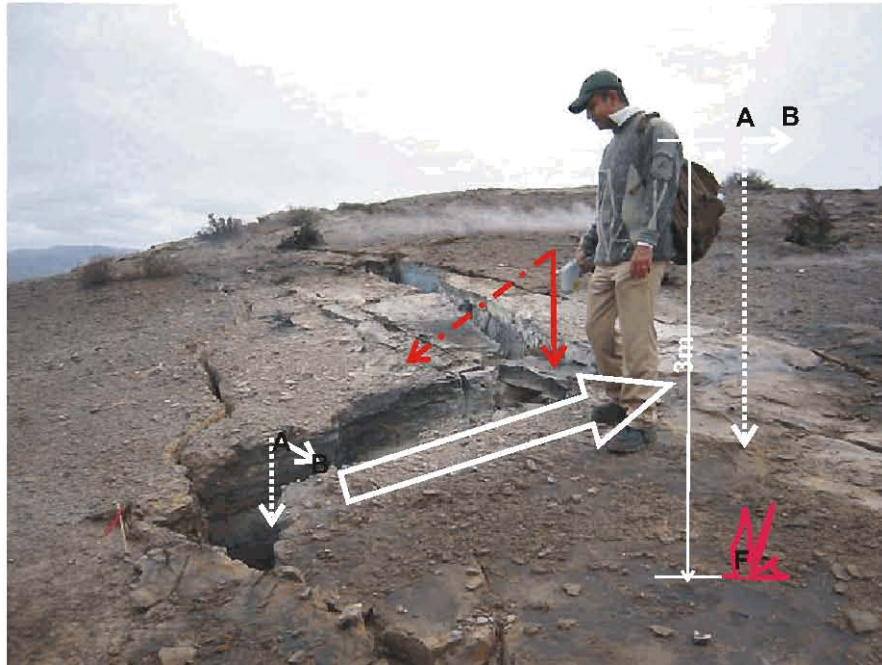


Figure 6.16 Temperature profile for a crack at coal fire No. 8, Wuda coal mine area (measured on September 10 and 14, 2002). From -2cm to the surface, temperature drops rapidly. On the surface 30cm away from the crack temperatures dropped to the normal background level.

6.2.4 A night-time temperature profile on coal fire No.12

Figure 6.17 shows a temperature profile on coal fire No.12, whose coordinates are 640894, 4371674. The measurements were taken at 21:55 on 12th September 2002. The fire was burning 2m below the surface in the marked area (F) with a temperature of 550°C. There is a crack in 5m distance from the coal fire. Temperature for the bottom of the crack was 206°C, for surface 46.2°C. Surface temperature for the spot in 10cm distance from the edge of the crack is 30.2°C. It can be seen that the underground coal fire does form a thermal anomaly above the covering rocks on the surface as shown by the dotted line in Figure 6.17, which means that heat can be transferred by conduction from the source of the fire. Zhang (2003) mentioned that heat conduction is a slow process compared to convection. Hence whether or not the heat can reach the surface of the covering bedrock and cause a thermal anomaly depends on the depth and the age of the coal fire in question. If the coal fires are very shallow, they may cause thermal anomalies on the surface of the covering bedrock areas. If the coal fires are old enough, the heat can be transferred to the surface by conduction. In addition, heat can also transfer laterally from the cracks of higher temperatures to the covering bedrock. In this case the thermal anomalies will increase in size when a coal fire grows older. This observation is consistent with the thermal modelling results of Rozema (2001). In our case, the background temperature is about 12°C and the thermal anomaly could reach about 20°C. The temperature difference reaches 8°C. It should be mentioned here that during the daytime, this thermal anomaly will disappear due to the high temperature of the background and the high temperature variance of the background as discussed in 6.2.1 and 6.2.2.

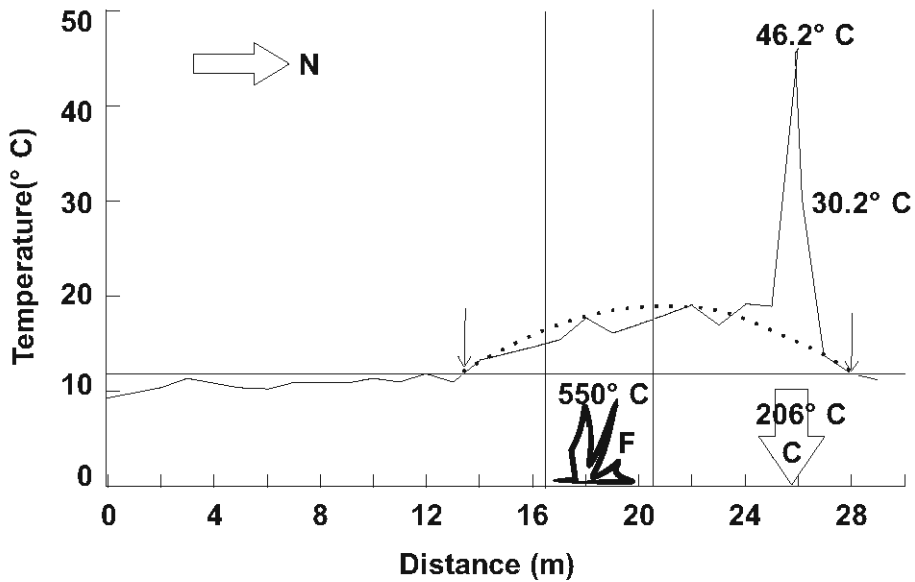


Figure 6.17 A temperature profile on coal fire No.12, Wuda coal mine area (measured at 21:55 on 12 September 2002). Underground coal fire forms a thermal anomaly above the covering bedrocks on the surface as shown by the dotted line.

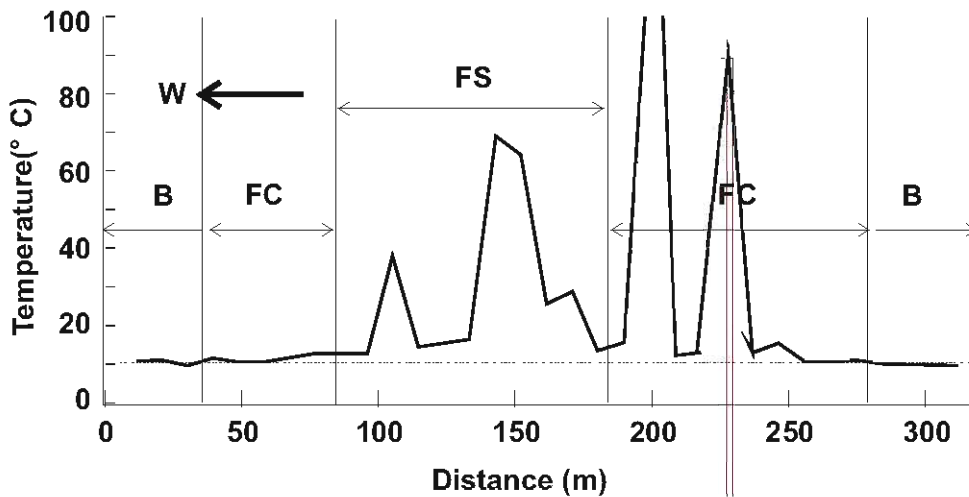


Figure 6.18 A temperature profile on coal fire No.8. B: background; FC: fire area with cracks; FS: fire area with surface subsidence. High surface temperature for an underground coal fire can be measured only on cracks or close to cracks (within 30cm).

6.2.5 A temperature profile on coal fire No.8

Figure 6.18 shows a temperature profile on coal fire No.8 measured at 10:00 on September 12. It crosses the background and a coal fire area. Coal fire No.8 includes two parts. One is the area with cracks but not subsided. The other is the area with collapsed overlaying rocks. Overlaying rocks subside due to the loss of volume underground when the coal has been burnt out by coal fires. There are a lot of cracks in the collapsed area. They form a kind of ventilation system for the fire, through which heat is released. A clear thermal anomaly can be seen. In the area with cracks which is not subsided, cracks are not so dense. Temperatures for the covering bedrock in this area show normal values. High surface temperatures for the underground coal fire can be measured only on cracks or close to cracks (within 30cm as mentioned in the last paragraph).

6.2.6 Discussion

Surface temperatures on a sand dune can vary 28°C within the sand dune. In a coal dump pile, temperature for a slope facing Southeast could be 20°C higher than that for a slope facing North between 10:00 to 14:00. The temperature variance caused by uneven solar heating can mask thermal anomalies related to coal fires.

Underground temperature profiles showed that one hour past sunrise, a thermal anomaly 1m away from the coal fire crack was overprinted by the effects of uneven solar heating. After two hours heat from the sun can reach 3.2cm below the surface.

Underground coal fires can form thermal anomalies above the covering bedrock layers. This can be observed during night-time only. Predawn is the best time for coal fire detection using thermal remote sensing techniques.

Thermal anomalies did not extend for more than 3m from the crack. The width of the thermal anomaly does not decline as the background temperature increases. Thus, the thermal pattern in remote sensing as well as field data above a coal fire actually is the pattern of cracks/vents.

6.3 Thermal Characteristics of Coal Fires on ETM+ Images

In this paragraph, the characteristics for coal fire areas, their thermal anomalous areas, and their background areas on ETM+ images are studied using a statistical method. Statistical characteristics of coal fire thermal anomalies on ETM+ images are not only the basis for developing an automatic method to extract coal fire thermal anomalies in large areas, but also programs developed in this study are helpful for verification and evaluation of the final results at a later stage.

6.3.1 Data input

1. Field coal fire distribution maps in the study areas: During the field work in 2002, all coal fires have been investigated in the study areas. The field coal fire distribution maps in study areas, referred to FieldFire2002, are shown in Figure 4.2.

2. ETM+ band 6 images: Five scenes of Landsat-7 ETM+ band 6 data (1G product) were used in the study as shown in table 6.2. The data include three daytime scenes and two night time scenes, named Night2002, Night2001, Day2002, Day2001, and Day1999. They cover all the Wuda, Ruqigou, Gulaben study areas.

Name	Pass	Row	Time	Date
Night2002	226	211	Night	28 September 2002
Day2002	129	33	Day	21 September 2002
Night2001	226	211	Night	25 September 2001
Day2001	129	33	Day	04 October 2001
Day1999	129	33	Day	12 August 1999

Table 6.2: ETM+ band 6 data used in the study

6.3.2 Methodology and image processing

1. Numbering coal fires on the field coal fire distribution maps: Each coal fire in the study areas has been assigned an index number. As shown in Figure 4.2 coal fires in Wuda area have been numbered from 1-17. Coal fires in Gulaben area have been numbered from 21-25, and coal fires in Ruqigou are from 31-45.

2. Interpreting thermal anomalous pixels on ETM+ images: When displaying the field coal fire distribution map on top of ETM+ band 6 images, it is found that not all the pixels of the coal fires can be detected as anomalous pixels due to the limitation of the detection capability. The ones detected by the images have been interpreted manually from the five input ETM+ images: Night2002, Night2001, Day2002, Day2001, and Day1999 respectively. The results, the thermal anomaly maps, are referred to AnoNight2002, AnoNight2001, AnoDay2002, AnoDay2001, and AnoDay1999, which are byte maps (0-background, 1-45: thermal anomalies correspondent to coal fire number 1-45). In Figure 4.2 thermal anomalous pixels interpreted from the Night2002 are shown in green colour.

3. Extracting background pixels from different spatial extends: When we have a thermal anomalous (coal fire) pixel or a cluster of pixels, we take its (their) neighbour non-anomalous (coal fire) pixels as its (their) background pixels.

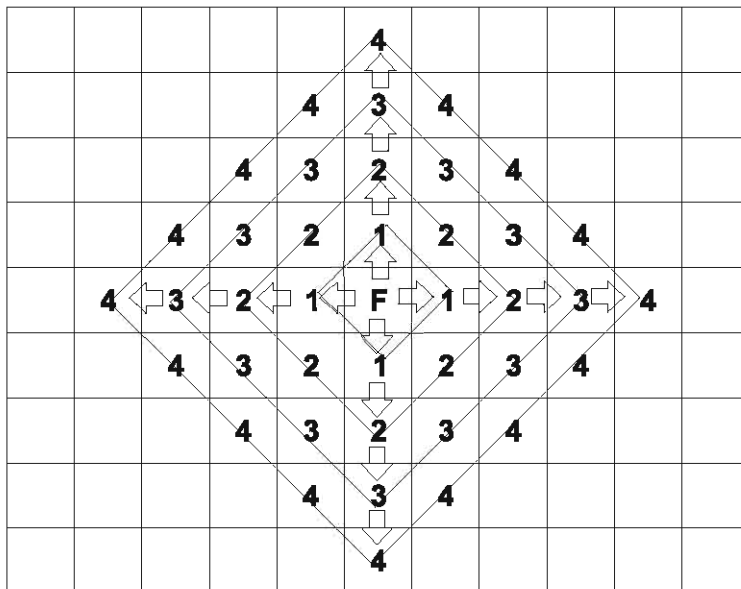


Figure 6.19 Illustration of neighbourhood pixels with different spatial extends.

During the process, firstly, a fire or a thermal anomalous pixel is located as F shown in Figure 6.19. Secondly, its four nearest neighbourhood pixels as 1 in the figure are searched. Thirdly, a neighbourhood pixel is chosen as the background pixel if it is not an anomalous pixel. This procedure can be applied iteratively and background pixels

will be extracted as pixels numbered 2, 3, and 4 in the figure. During the study, the neighbourhood technique was applied for 1, 6, 11 and 16 times, respectively. The results are named as Background neighbourhood 1, Background neighbourhood 6, Background neighbourhood 11, and Background neighbourhood 16 as shown in Figure 6.20. They represent the background pixels in an increasing buffer area around the anomalous pixel as illustrated in Figure 6.19.

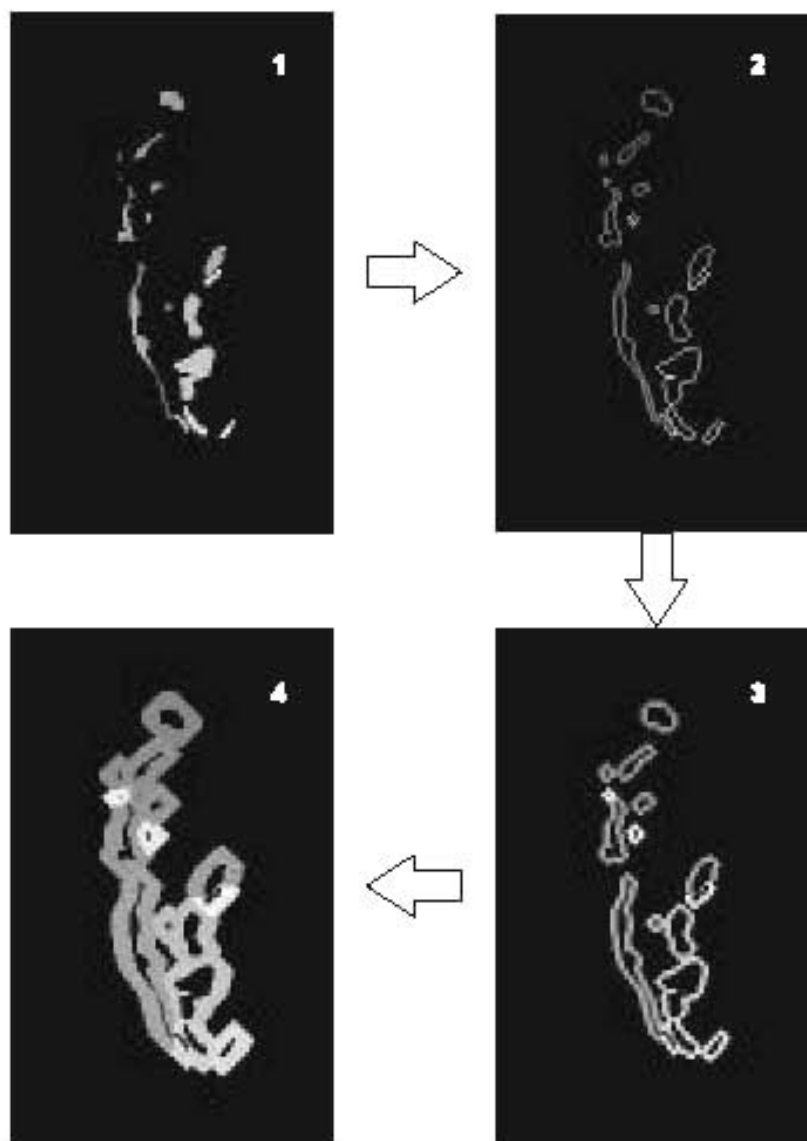


Figure 6.20: Determination of background pixels in the Wuda area. 1: Thermal anomalous pixels; 2: Pixels for background neighborhood 1; 3: Pixels for background neighborhood 6; 4: Pixels for background neighborhood 16.

4. Calculating statistics: Pixels of a coal fire can be extracted from an ETM+ band 6 image to form a numeric vector:

$$X = (x_0, x_1, x_2, \dots, x_{N-1})$$

Where,

$x_0, x_1, x_2, \dots, x_{N-1}$: DN value of the pixels in the coal fire area on an image

Then statistical characteristics of the numeric vector X can be calculated. Here statistical characteristics include: number of pixels, maximum, minimum, mean, median, standard deviation (STD), and histogram. Formulas for the calculation are given below:

$$Mean = \bar{x} = \frac{1}{N} \sum_{j=0}^{N-1} x_j$$

$$STD = \sqrt{\frac{1}{N-1} \sum_{j=0}^{N-1} (x_j - \bar{x})^2}$$

6.3.3 Results

1. Statistical characteristics of thermal anomalies and their backgrounds on ETM+ band 6 images: During the study, statistical characteristics of the thermal anomalies on the five input images are calculated. The results for the Night2002, and the Day2002 are shown in Appendix 6.6 and Appendix 6.7. The following observations can be made:

The maximum, minimum, median, and mean DN values of all the thermal anomalies are higher than those of the backgrounds both in day time and night-time images. At the same time, the minimum, median, and mean DN values of the thermal anomalies, except the maximum, decrease with the increase of the buffer zone of the backgrounds (Background neighbourhood 1- Background neighbourhood 6 - Background neighbourhood 11 - Background neighbourhood 16). Figure 6.21 shows the maximum, mean, and minimum value of each coal fire area on the Night2002 scene. The X axis is

the coal fire number as shown in Figure 4.2, ordered in a decline sequence of number of pixels.

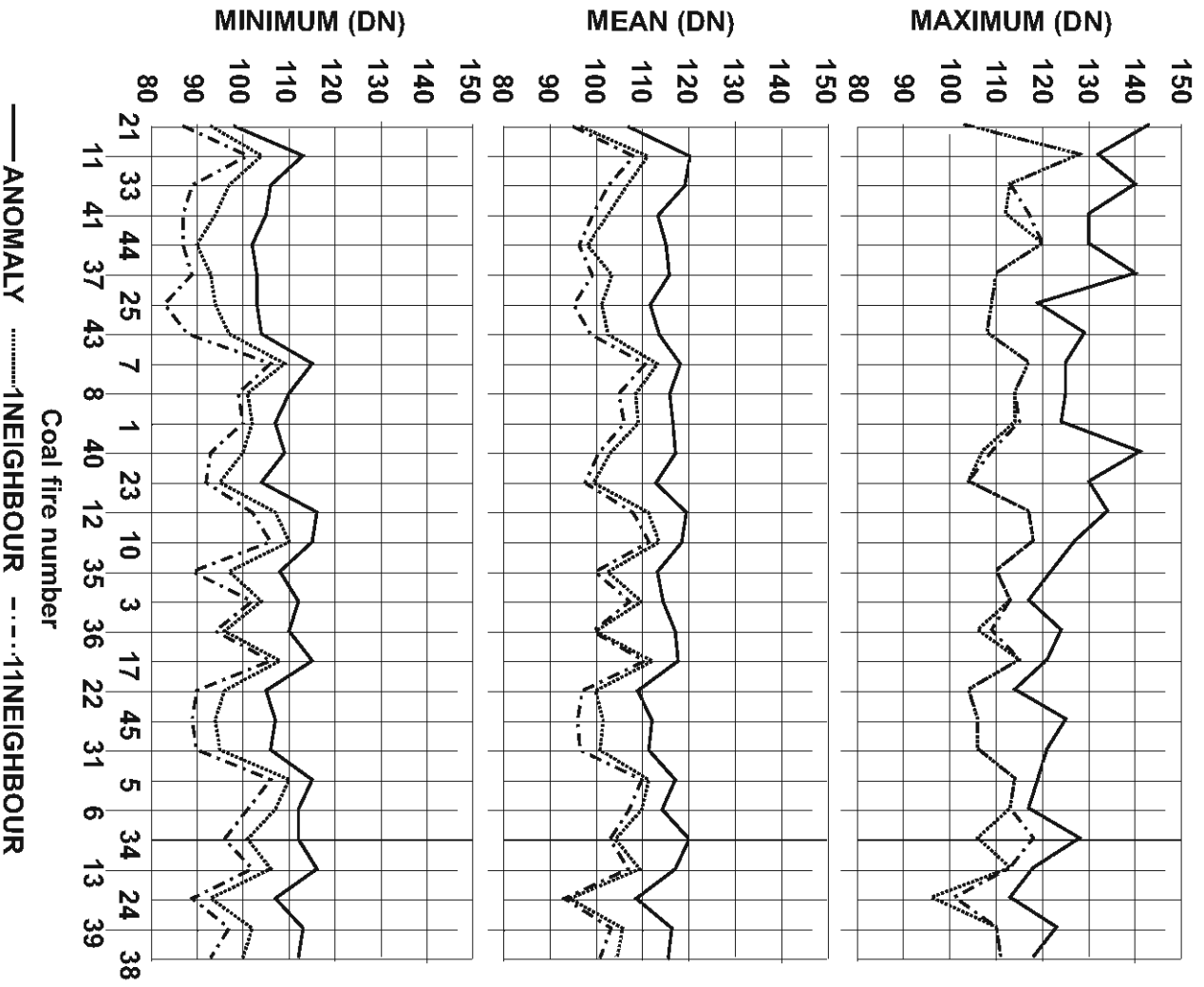


Figure 6.21: Maximum, mean and minimum values of thermal anomalies on a night-time ETM+ image acquired in 2002. Maximum, mean and minimum values of a thermal anomaly are higher than its background. Mean and minimum decrease with the increase of the spatial extends of the backgrounds.

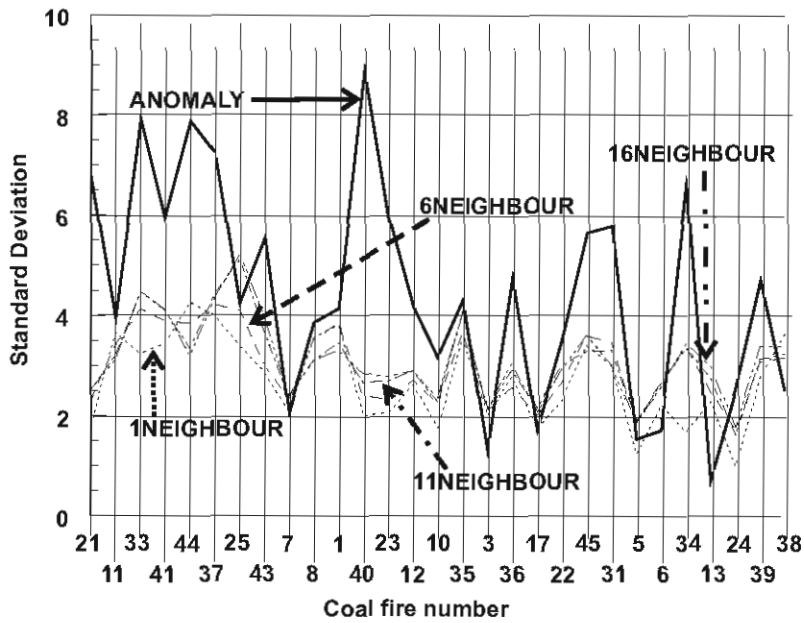


Figure 6.22: Standard deviation of thermal anomalies on a night-time ETM+ image received in 2002. Standard deviation of a thermal anomaly is higher than its background on a night-time thermal image.

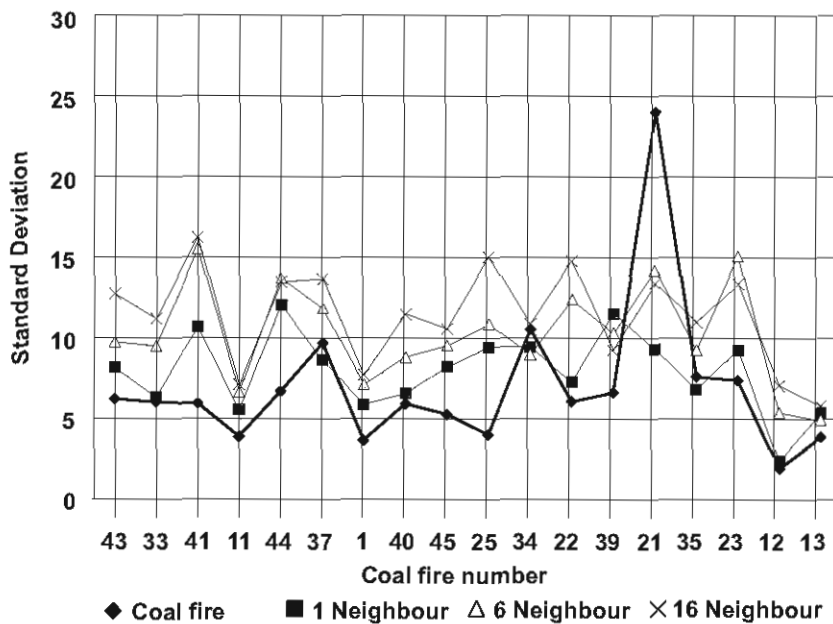


Figure 6.23: Standard deviation for thermal anomalous areas on a daytime ETM+ image acquired in 2002. Standard deviation of a thermal anomalous area is smaller than its background on a daytime thermal image.

About 80% of the thermal anomalies on night-time images (Night2002 and Night2001) have higher values of the standard deviation than their backgrounds. Figure 6.22 shows the standard deviation of each thermal anomalous area on Night2002. But on the day time images (Day2002, Day2001, and Day1999), about 70% of the thermal anomalies have lower values of the standard deviation than their background. Figure 6.23 shows standard deviation of each thermal anomalous area on Day2002.

2. Histogram of coal fire (thermal anomalous) areas and their background areas on ETM+ images: Histograms of each coal fire or thermal anomaly and their background were plotted during the study. Here coal fire No. 8 in Wuda, coal fire No. 41 in Ruqigou, and coal fire No. 21 in Gulaben are taken as representatives. Figure 6.25 shows the histograms for these three coal fires and their 6-neighborhood background on Night2002. The coal fire areas were taken from the field coal fire distribution map, which represents the fire areas demarcated in the field. It can be seen that parts of the histogram for coal fire areas is overlapping with their background. This means that most parts of the coal fire areas surveyed in the field show no difference from their background, and they can not be detected using ETM+ band 6 night-time image. Figure 6.26 shows the histograms for thermal anomalies (coal fire No. 8, coal fire No. 41, coal fire No. 21) and their 6-neighborhood background on Night2002. Their anomalous areas were taken from AnoNight2002, which represents the anomalous areas that can be detected on Night2002. It can be seen that most parts of the histogram for thermal anomalous areas are separable from their background and within the high DN value range. Histograms of the coal fire thermal anomalous areas or coal fire areas on night-time images show multi-separated peaks. Histograms of the background areas on night-time images show no separated peaks and are located within the low digital number range. Figure 6.27 shows the histograms for two thermal anomalies (coal fire No. 41, coal fire No. 21) and their 6-neighborhood background on Day2002. Their anomalous areas were taken from AnoDay2002, which represent the anomalous areas that can be detected on Day2002. The histogram for coal fire No.8 on Day2002 is not shown on the figure, because it has only one pixel that can be interpreted as a thermal anomaly on the Day2002. Histograms of the background areas on daytime images (Day2002, Day2001, and Day1999) show many separated peaks

which are located within the low digital number range. Less thermal anomalous pixels are detected by daytime images than in night-time images. From the histogram, it is known that every coal fire (thermal anomaly) has its own distinct start and end DN value. This can be interpreted as the fact that each coal fire forms a thermal anomaly with a different temperature range. Therefore it can be concluded that it is not accurate to use a single threshold to separate coal fire thermal anomalous areas from their backgrounds.

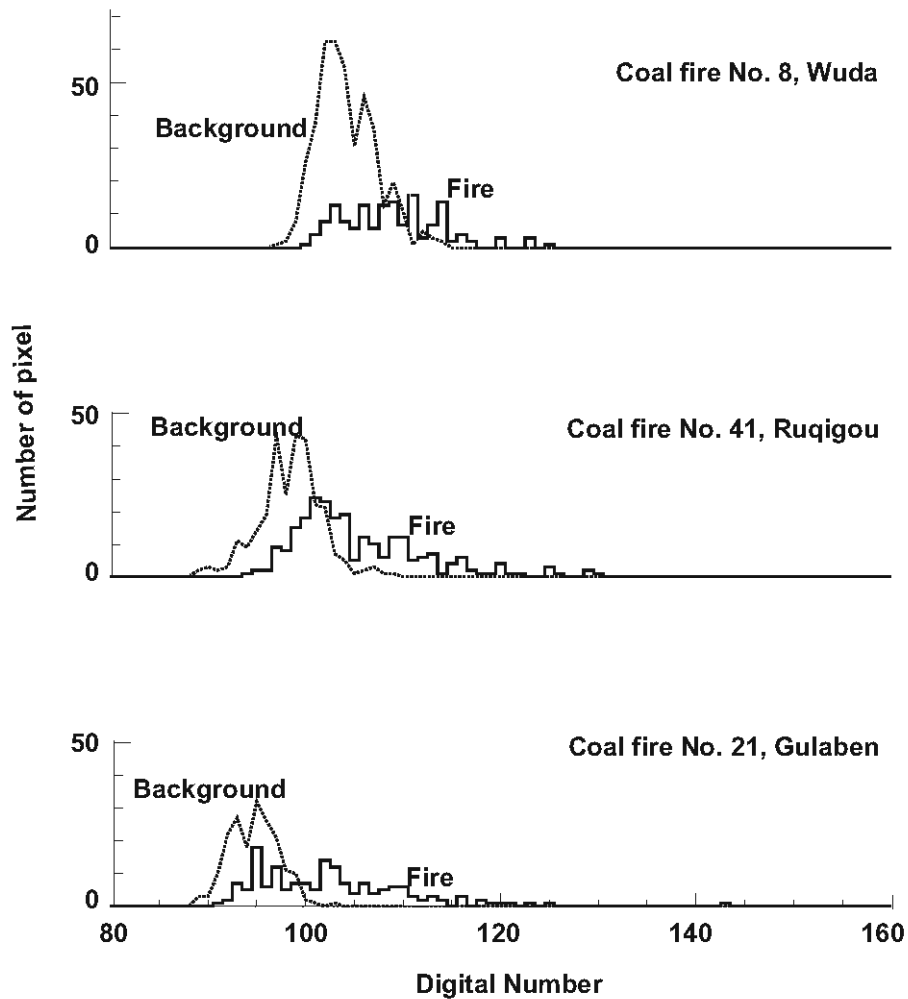


Figure 6.25: Histogram for field coal fire areas on a night time ETM+ image acquired in 2002. Parts of the histogram for coal fire areas surveyed in the field overlap with background histogram. They can not be detected using an ETM+ band 6 night-time image.

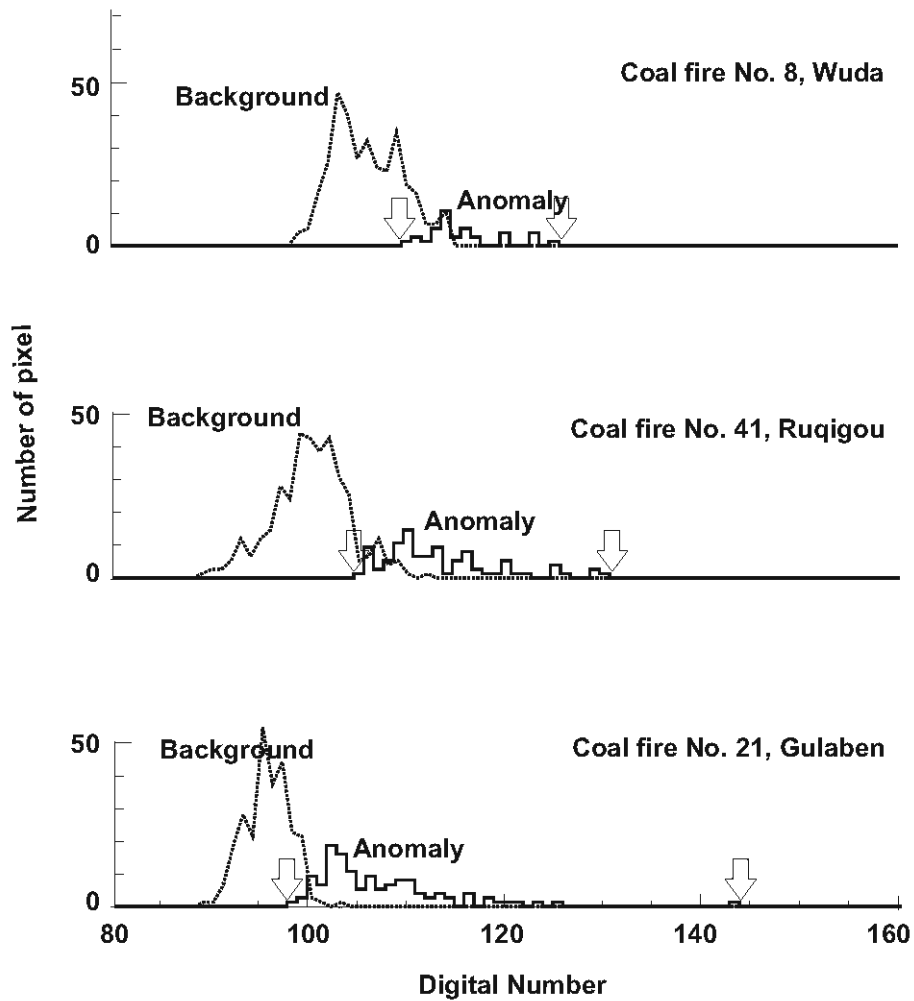


Figure 6.26: Histogram for thermal anomalous areas on a night-time ETM+ image acquired in 2002. Different thermal anomalies related to coal fires have different start and end DN values.

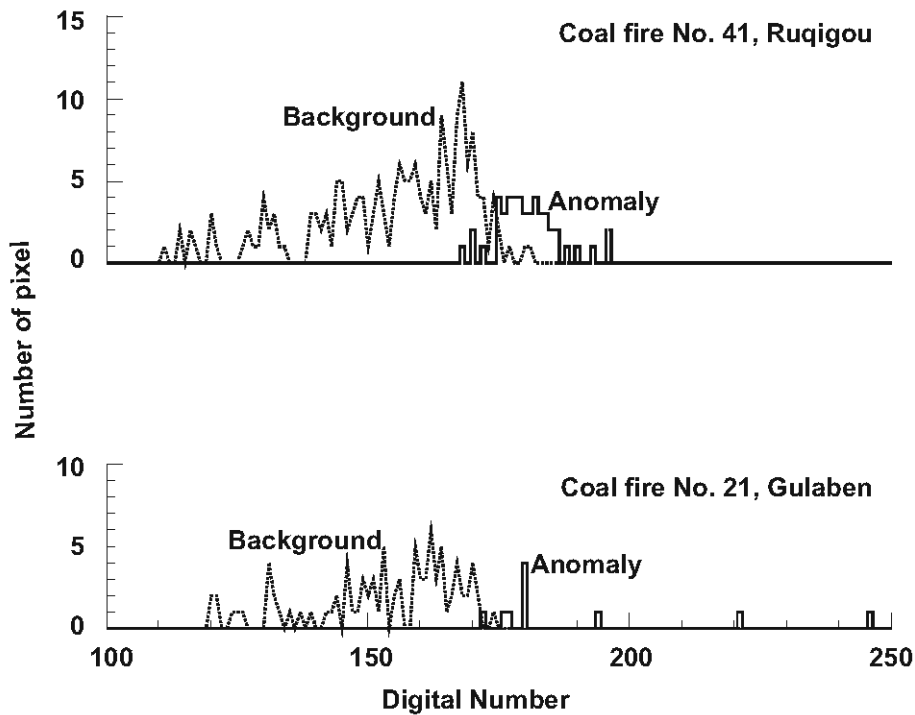


Figure 6.27: Histogram for thermal anomalous areas on a daytime ETM+ image acquired in 2002. Less thermal anomalous pixels detected in daytime images than in night-time images.

3. Field coal fire areas, their correspondent thermal anomalous areas on the night-time image and the daytime image: Table 6.3 shows the number of pixels for the field coal fire areas and their thermal anomalies interpreted on AnoNight2002 and AnoDay2002. In the study areas there are a total of 37 separate coal fires surveyed in the field. On the image AnoNight2002 there are 30 correspondent thermal anomalies. 81% of the coal fires surveyed from the field can be detected on Night2002. There are 7 field coal fires that can not be seen in the image (19%). This is because these coal fires are too small. All together they occupy less than 12 pixels. On the image AnoDay2002 there are 24 correspondent thermal anomalies. 65% of the coal fires surveyed in the field can be detected in Day2002. This is because of uneven solar heating influence. The 37 coal fires surveyed in the field occupy from 1 pixel to 242 pixels, and a total of 2511 pixels. The correspondent thermal anomalies on AnoNight2002 occupy from 1 pixel to 101 pixels, and a total of 818 pixels, among which 744 pixels are inside the field coal fire area, and 74 pixels are outside the field

coal fire area. One third (30%) of the total field coal fire areas can be detected by Night2002. For AnoDay2002, they occupy from 1 pixel to 76 pixels, and a total of 488. Only 19% of total field coal fire areas can be detected by Day2002. It should be mentioned here that coal fire No.43 was 8 pixels over interpreted on Day2002.

FN	Pixel Number					Ni/F	D/F	FN	Pixel number					Ni/F	D/F
	F	N	Ni	No	D				F	N	Ni	No	D		
1	63	27	27	0	31	43%	49%	23	72	22	21	1	9	29%	12%
2	4	0	0	0		0%	0%	24	9	5	5	0	2	56%	22%
3	33	13	8	5	2	24%	5%	25	198	39	38	1	22	19%	11%
4	8	0	0	0		0%	0%	31	25	7	7	0	2	28%	8%
5	14	6	5	1		36%	0%	32	7	0	0	0		0%	0%
6	55	6	4	2		7%	0%	33	219	80	79	1	53	36%	24%
7	65	42	30	12	2	46%	3%	34	26	6	6	0	17	23%	65%
8	142	31	25	6	1	18%	1%	35	97	13	13	0	9	13%	9%
9	6	0	0	0	1	0%	17%	36	37	11	11	0		30%	0%
10	100	21	13	8	46	13%	43%	37	181	51	51	0	35	28%	19%
11	203	86	75	11	6	37%	3%	38	30	4	4	0		13%	0%
12	46	23	19	4	4	41%	8%	39	34	4	4	0	11	12%	32%
13	14	2	1	1		7%	0%	40	104	24	24	0	25	23%	24%
14	20	2	0	2		0%	0%	41	241	78	77	1	48	32%	20%
15	5	0	0	0		0%	0%	42	11	0	0	0		0%	0%
16	1	0	0	0		0%	0%	43	68	36	36	0	76	53%	100%
17	19	5	0	5		0%	0%	44	115	54	54	0	39	47%	34%
21	148	101	88	13	10	59%	6%	45	24	8	8	0	23	33%	96%
22	67	11	11	0	14	16%	21%	T	2511	818	744	74	488	30%	19%

Table 6.3 Number of pixels for field coal fire areas and their thermal anomalies on night-time and daytime ETM+ images acquired in 2002. FN: Fire name number; F: Field coal fire distribution map; N: AnoNight2002; D: AnoDay2002; Ni: Pixels in both AnoNight2002 and FieldFire2002; No: Pixels in AnoNight2002 but FieldFire2002; T: Total.

6.3.4 Conclusion

1. The minimum, median, and mean DN values of the thermal anomalies decrease with the increase of the buffer zone of the backgrounds.

2. The maximum and the standard deviation of a thermal anomaly on night-time ETM+ images are higher than its background. On day time ETM+ images, the standard deviation is smaller than its backgrounds.
3. Coal fires form thermal anomalies on images with their distinct start and end DN values. It is not accurate to use a single threshold to separate coal fire thermal anomalous areas from their backgrounds.
4. ETM+ night-time images are suitable for general survey of coal fires in large areas. About eighty percent of coal fires can be detected. For daytime images, less coal fires can be detected. It is expected that daytime images acquired in winter time can improve the performance.
5. For detailed coal fire area mapping, ETM+ images with 60m spatial resolution of the thermal band are too coarse. They can only map about one third of the total coal fire areas.
6. Comparing the interpreted thermal anomalous image AnoNight2002 with the field coal fire distribution map FieldFire2002, it is found that there are 74 anomalous pixels in AnoNight2002 located one or 3 pixels outside of the field coal fire areas. This mismatch originates probably from one or more of the following points: 1) the error of the field coal fire investigation; 2) The error of the geometric registration; 3) The error of the thermal anomaly interpretation. AnoNight2002 can not be used to correct the FieldFire2002, even though the anomalies are outstanding in the image.

CHAPTER 7 ALGORITHM DEVELOPMENT FOR THE EXTRACTION OF COAL FIRE RELATED THERMAL ANOMALIES

It is known from paragraph 6.1 that coal fires have high temperatures and form thermal anomalous clusters on thermal images when images have a high spatial resolution. For example, the simulated underground coal fire with a dimension of 1m*1m forms an outstanding thermal anomalous cluster in MP 50 line scanner images, whose spatial resolution is 5cm. The simulated surface coal fire can heat the surroundings through radiation and convection in a proximate distance of 2m and form a 1°C difference thermal anomaly. It is hard for a coal fire to heat an area beyond a distance of 4.5m. In reality, a surface coal fire covers an area of only a few square meters. From paragraph 6.2 it is known that thermal anomalies do not extend more than 3m from a crack related to an underground coal fire. The thermal pattern in remote sensing images as well as field data above an underground coal fire actually is the pattern of cracks. In the Northwest of China, the cracks are typically 5-500m long and 0.1 to 1m wide. The longest cracks can extend to over 1 km, and the widest can reach 2.5 m. Thermal anomalies related to coal fires are not outstanding in a scene of ETM+ band 6 image, since the spatial resolution of the image is 60m * 60m and thermal anomalies are only the local maxima. About eighty percent of coal fires can be manually detected by using ETM+ band 6 night-time images as mentioned in paragraph 6.3. In the following chapter, we are going to discuss how to automatically extract thermal anomalies related to coal fires from their background. Landsat-7 ETM+ band 6 night-time image 226-211 (path-row) acquired on 25 September 2001 is chosen for the algorithm development and is shown in Figure 7.1. The correspondent daytime image acquired on 4 October 2001 is used for supporting the interpretation and presenting the results.

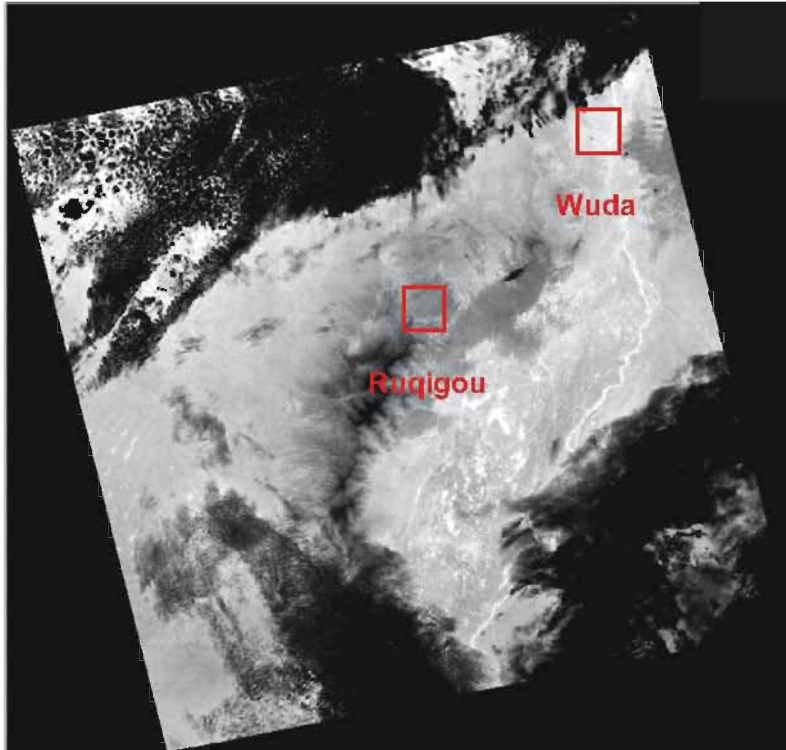


Figure 7.1: Landsat-7 ETM+ band 6 night-time image 226-211 (path-row) acquired on 25 September 2001. It has 3778 columns by 3589 lines, covering an area of 185km by 185km. High DN values are related to the water body. Coal fire thermal anomalies in Wuda and Ruqigou area are not outstanding in this large-scale view.

7.1 Review of the Previous Algorithms for Anomaly Extraction

Anomaly extraction may be regarded as a branch of image processing, as image processing involves the manipulation of images to extract information; to emphasize or de-emphasize certain aspects of the information contained in the image; or to perform statistical or other analyses to extract non-image information (Cracknell & Hayes 1991). There are many ways of processing images and we are particularly attracted to three of them. They are spatial filtering, image classification, and anomaly detection.

7.1.1 Spatial filtering

Filtering provides a means of improving images by suppressing or enhancing certain spatial frequencies, directions and textures (Rosenfeld & Kak 1976). Filtering is a process in which each pixel value in a raster map is replaced with a new value. The

new value is obtained by applying a certain function to each input pixel and its direct neighbours. These neighbours are usually the 8 adjacent pixels (in a 3 x 3 filter) or the 24 surrounding pixels (in a 5 x 5 filter). For example, a low pass filter replaces the central pixel in the array with the mean of the total array as it passes over the image. It has proved to be particularly useful for reducing noise in an image prior to a multi-band image classification when classifying rather large areas.

7.1.2 Image classification

The two most popular methods of doing image classification are a density slice of one band or a supervised classification of several bands. Density slicing involves the grouping of image regions with similar DN, either automatically or interactively. Ranges of values of the input map are grouped together into one output class. A preferable method is to choose thresholds on the basis of breaks or troughs in the scene histogram. Supervised classification involves the careful choice of bands, the location of small but representative training areas, the determination of the relationship between object type and DN in the chosen bands, the extrapolation of these relationships to the whole image data set and accuracy assessment of the resultant image (Curran 1985). There are several classifier that can be used to extrapolate the results of training over the whole data set (Lee et al 1977, Hixson et al 1980). The three most popular are, the minimum distance to means classifier, the parallelepiped classifier and the maximum likelihood classifier (Lillesand & Kiefer 1979). The minimum distance to means classifier is the simplest classifier to compute as it comprises just three simple tasks. First, the mean DN of a class in the training data is calculated for all bands, this is termed the mean vector. Second, the pixels to be classified in the whole data set are allotted the class of their nearest mean vector. Third, a data boundary is located around the mean vectors such that if a pixel falls outside of this boundary, then it will be classified as 'unknown'. The parallelepiped or 'box' classifier operates in the same way as a simultaneous density slice in all bands. The maximum likelihood classifier works by first, calculating the mean vector, variance and correlation for each land cover class in the training data, on the usually valid assumption that the data for each class are normally distributed (Castleman 1979). With this information the spread of pixels around each mean vector can be described using a probability function. Pixels

from the whole data set are allocated to the class with which they have the highest probability of membership. As every spectral response has a probability, however low, of representing a class, no pixels are left out in the cold.

7.1.3 Anomaly detection

Target detection in remotely sensed images can be conducted spatially, spectrally, or both. The difficulty with using spatial image analysis for target detection in remotely sensed imagery arises from the fact that often the sensor footprint is generally larger than the size of targets of interest. In this case, targets are embedded in a single pixel and cannot be detected spatially. Under such circumstances, target detection must be carried out at subpixel level. An anomaly detector enables one to detect targets whose signatures are spectrally distinct from their surroundings. In this section, an anomaly detector, named RX detector (RXD), is of interest and described.

The RXD was developed by Reed & Yu (1990) to detect targets whose signatures are distinct from their surroundings. Suppose that L is the number of spectral bands and r is an $L \times 1$ -column pixel vector in a multispectral or hyperspectral image. Then the RXD implements a filter specified by

$$\delta_{RXD(r)} = (r - \mu)^T K_{L \times L}^{-1} (r - \mu)$$

Where μ is the global sample mean and $K_{L \times L}$ is the sample covariance matrix of the image. The Form of $\delta_{RXD(r)}$ in the formula is actually the well-known Mahalanobis distance. In order to see how the RXD can detect anomalous targets, an exploration of how the RXD works is worthwhile.

It is known that principal components analysis (PCA) decorrelates the data matrix in such a manner that different amounts of the image information can be preserved in separate components images, each of which represents a different piece of uncorrelated information. So, PCA has been widely used to compress image information into a few major principal components specified by the eigenvectors of $K_{L \times L}$ that correspond to large eigenvalues, but it is not designed to be used for detection or classification. However, if the image data contain interesting target pixels which occur with low

probabilities in the data, it is obvious that these targets will not be shown in major principal components, but rather in minor components specified by the eifenvectors of $K_{L \times L}$ that are associated with small eigenvalues. It is interesting to note that the RXD can be considered to be an inverse operation of the PCA which seaches for targets in minor components. This provides explanation of why the RXD works for anomaly detection (Chang & Chiang 2002). But the RXD works only in a multispectral or hyperspectral image. It does not work in a single band image, such as ETM+ band 6. image.

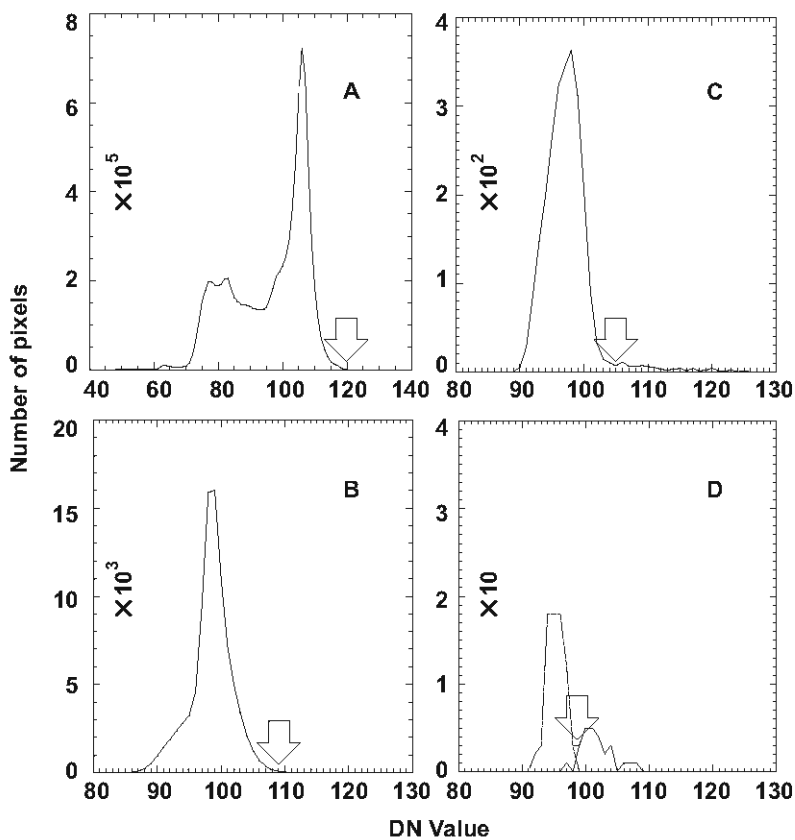


Figure 7.2: Histograms of Landsat-7 ETM+ band 6 data. A: whole scene (3778 * 3589); B: Ruqigou area (300*300); C: Gulaben coal fire area (50*50); D: One coal fire in Gulaben (10*10). In D, Line: histogram of coal fire thermal anomalies; Dot line: histogram of the total pixels; Line-dot-line: histogram of the background. In a small subset of an image, coal fire thermal anomalies are easier to be separated from their background.

7.2 Algorithm Development for the Extraction of Coal Fire Related Thermal Anomalies

7.2.1 Dividing a night-time ETM+ image into subsets using a moving window

Figure 7.1 shows that coal fire thermal anomalous pixels in Wuda and Ruqigou areas are not necessarily the pixels with highest DN values in the whole image. Most obvious pixels with high DN values in the image are water bodies. Actually, thermal anomalous pixels related to coal fires are pixels with local high DN values (local maxima). Therefore the only means of detecting coal fires is by using local filtering techniques in small subareas.

Figure 7.2a shows the histogram of the whole image (3778 columns * 3589 lines). The histogram has several peaks representing several classes of materials with different thermal properties. There is no evidence signalling coal fire thermal anomalies. If thermal anomalous pixels have to be defined in the image, they might be located at the part larger than DN value 120. Figure 7.2b shows the histogram of a 300*300 window, which covers the whole Rujigou coal field (See Figure 6.19). The histogram has only one peak, it is suggested that coal fire thermal anomalies form the part larger than DN value 108. Figure 1c shows the histogram of a 50*50 window, which includes three known coal fires (coal fire No. 21, 22 and 23) in Gulaben mining area. According to the field data, the coal fire thermal anomalous pixels with a total number of 157 have been picked out manually within this window. The histogram shows a clear turning point at DN value 105, which suggests that background pixels have DN values lower than 105. Actually in the window there are 77 pixels, about 49% of the total anomalous pixels, with larger DN values than 105. They are all verified as coal fire induced thermal anomalies. Figure 7.2d shows the histogram of a 10*10 window, which includes part of coal fire No. 21 with 26 pixels. The coal fire thermal anomalous cluster and background cluster are clearly separable. Their boundary is located at DN value of 97/98. In this window, there are 28 pixels with the DN value equal or higher than 97, among which 25 pixels, 96% of total anomalous pixels, are verified as coal fire induced thermal anomalies. This indicates that coal fire induced thermal anomalous pixels can be extracted successfully within a suitable subset of an image.

Now the question is how a suitable subset can be found within an image when the coal fire area is not known. This can be solved through a moving window method: For a given image with M columns and N rows, a small moving window with $M1$ columns and $N1$ rows can be selected ($M1 \leq M, N1 \leq N$). Subsegment subsets of an image can be defined with the help of the window by moving it over the image with the step X ($X \leq M - M1$) in the column direction and step Y ($Y \leq N - N1$) in the row direction. When the window passes the whole image, a pixel in the image will be sampled in $(M1 * N1) / (X * Y)$ subsets as shown in Figure 7.3.

7.2.2 Separation of thermal anomalies and their background based on histogram features

When a subset of the image is chosen, a threshold needs to be set within the subset to separate the thermal anomalies and the background. There are three ways to select the threshold. The first one is the trial and error method (Saraf et al. 1995; Prakash et al 1995). In this method, different thresholds have to be tested for a data set. The one that provided a reasonable and overall best match for discriminating non-fire areas from the fire areas would be finally chosen as the threshold for the data set. The second one is an exclusion method (Zhang 1998). It gives a threshold which excludes all pixels outside the coal-seam areas. These two methods are only working in a known area. The third one is a statistical method. In an unknown area, the statistical method is the only choice. Statistically speaking, coal fire thermal anomalous pixels and background pixels will form two clusters in the subset histogram. In Figure 7.4 curve 1 shows the histogram of 100 background pixels, which are chosen randomly from the known background in Gulaben area. Curve 2 shows the histogram of 100 known thermal anomalous pixels in the same area. Curve 3 is the sum of both histograms. A turning point, as pointed in the figure will be formed in most cases, although it is difficult to prove. Theoretically speaking, the threshold for distinguishing thermal anomalies and background could be set at three points indicated by the letters A, B and C in Figure 7.4. Point A is the histogram beginning of the thermal anomalous cluster, whose DN value is 97. This threshold can extract all the thermal anomalous pixels out of the subset. But the problem is that many background pixels will be misclassified as anomalous pixels. Point B is the histogram end of the background, whose DN value is

102. This threshold does not take any background pixels as thermal anomalous pixels. But some real thermal anomalous pixels are lost. Point C is the cross point of the two histograms, whose correspondent DN value is 101. In reality threshold A and B have a weak point, which is, that they are not known and hard to be defined. In the case shown in Figure 7.4, only C could be defined through looking for the first turning point after the maximum value of the histogram. In case a turning point is not formed at the cross point, the first turning point inside the coal fire histogram will be the substitute (See Figure 7.4 D), since histograms of the coal fire thermal anomalous areas or coal fire areas on night-time images show multi-separated peaks and a lot of turning points according to paragraph 6.1.3.

When C is set as the threshold of a subset, some thermal anomalous pixels related to coal fires will not be detected while some of the background pixels will be detected as thermal anomalous pixels. These false alarms from each subset will be propagated into the final result. Even a small number of false alarms from the subset can make the final result unacceptable.

It has to be considered that background histograms can form multiple peaks and turning points due to the diversity of the background materials. This means that the first turning point after the maximum value of the histogram is not necessarily the cross point of the coal fire cluster and background cluster. These two problems can be avoided by setting a starting point, which is defined as the mean plus standard deviation of the subset. The first turning point after the starting point will be taken as the threshold of the subset. The starting point ensures that the thermal anomalous pixels extracted from a subset are below a certain percentage of the total pixel number. For example, if the histogram of the subset follows a normal distribution, the thermal anomalous pixels extracted will not exceed 15.9% of the total pixel number.

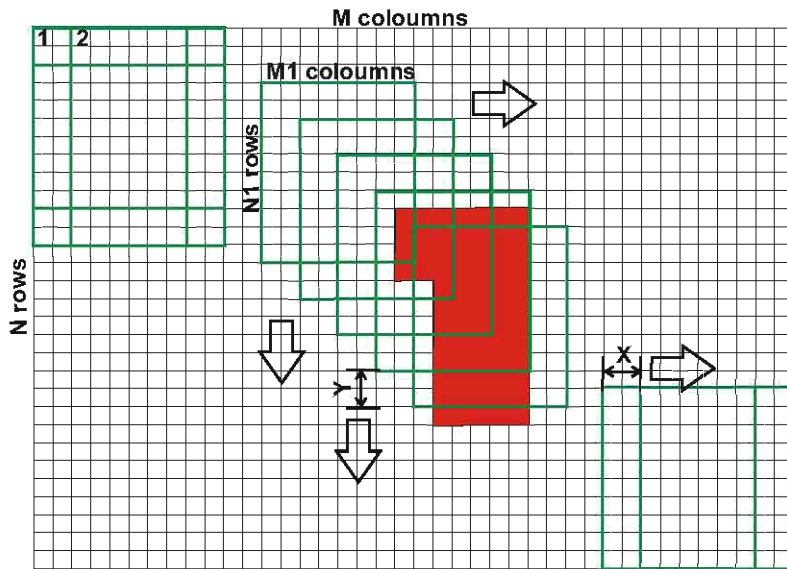


Figure 7.3: Moving window method. Subsets of an image can be derived through a window moving over it. A pixel on the image will be sampled $(M1 \cdot N1) / (X \cdot Y)$ times. A pixel in coal fire area will be sampled in different windows.

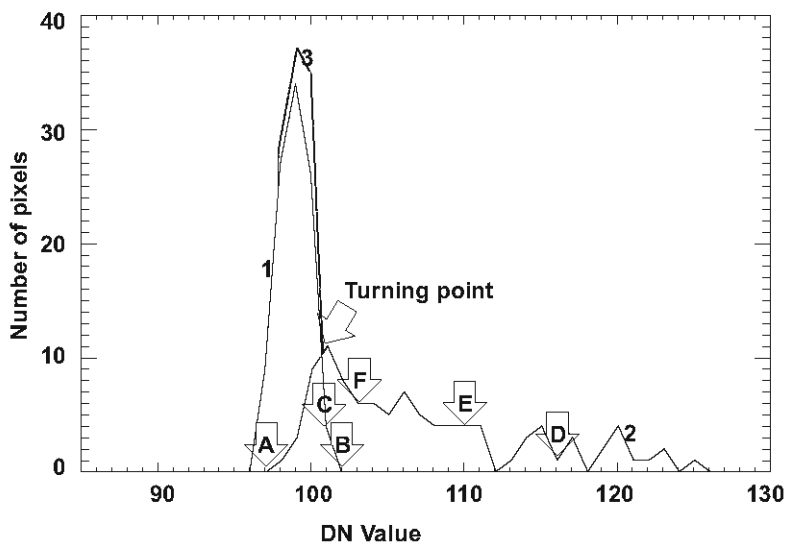


Figure 7.4: Histograms of the known coal fire thermal anomalies and the background. 1: Histogram of the background with 100 pixels, which are chosen randomly from the known area in Gulaben. 2: Histogram of 100 known thermal anomalous pixels in the same area. 3: Histogram of the combined 200 pixels. A, B, C, D, E, and F: thresholds for distinguishing background and thermal anomalies.

7.2.3 Presenting the output result retrieved from a suitable window size, moving steps and cut-off percentage

Let's consider the example presented in the Figure 7.4. Suppose there is a subset with dimensions of 10 columns by 10 rows, which consists only of background pixels (i.e. no coal fire presents). The mean and the standard deviation of the subset are calculated as 99 and 1 respectively. The turning point will be searched from the starting point 100. The turning point can be found at 102 (B) so that there will be no thermal anomalous pixels in the subset. The accuracy is 100%. Table 7.1 shows the extraction result for simulated subsets with different sizes.

Subset size	10*10	10*20	10*100	10*10
Fire pixels	100	100	100	0
Background pixels	0	100	900	100
Mean	107	103	99	99
Standard deviation	8	7	3.8	1
Starting point	115	110	102	100
Turning point	116 (D)	110 (E)	103 (F)	102 (B)
Detected pixels	15	31	62	0
Accuracy (%) of fire detection	15	31	62	100

Table 7.1 Extraction result for simulated subsets with different sizes

It can be seen from Table 7.1 that the increase of the subset size improves the extraction result. On the other hand, it is known from paragraph 6.1.3 that every coal fire (thermal anomaly) has its own distinct start and end DN value. This can be interpreted in a way that coal fires form thermal anomalies with different temperature ranges. It is not accurate to use a single threshold to separate coal fire thermal anomalous areas from their backgrounds. Every coal fire thermal anomalous cluster has to be extracted in a distinct subset of the image, which should be as small as possible. Then a new question comes up, which is how to choose a suitable window size to separate the image into proper subsets. This will be discussed in detail in the next chapter. Here, it can be stated that the coal fire's spatial dimension decides the best window size. At the mean time, due to the moving of the window, a pixel in the image will be counted many times and each time belonging to a different subset. This

compensates the importance of the window size. For example, when a 10 by 10 window passes a coal fire area with 1 by 1 steps, the first subset only includes 1 thermal anomalous pixel, equal to 1 percent of the subset. The next will include 2 pixels, and so forth. This ensures that a coal fire boundary could be detected even if the fire has a relative large thermal anomalous cluster.

The moving steps of the window decide how many times a pixel in the image will be sampled. A pixel in the image is sampled at maximum times when the steps are set at 1 by 1 in both column and row directions. At this time, a pixel has been calculated in the context with all the possible neighbourhood pixels. The result is more reliable than any other bigger steps.

After a suitable window size ($M1*N1$) is chosen, the window can move over the image with step 1 by 1 to derive subsets. When a pixel has a larger DN value than the threshold of the subset, it is considered as a thermal anomaly and counted once in the result matrix. A pixel will be checked ($M1*N1$) times in different subsets. The counting number in the result matrix will be summed up. The result matrix can be used to produce the binary output result with two digital numbers: 1 representing the thermal anomaly and 0 representing the background. Therefore we need to develop a computer-automated thresholding method that will automatically extract the anomalous target pixels and segment them from the background. In doing so, a threshold criterion is required. For a given value a in the result matrix ($0 \leq a \leq M1*N1$), we define a threshold α_0 , which is a cut-off percentage (γ) times the total counting numbers ($M1*N1$). When $a \geq \alpha_0$, then the pixel will be detected as a thermal anomaly. This cut-off percentage (γ) strongly influences the output result. Thermal anomalous pixels in the final map increase when the threshold γ decreases. This will be further discussed in the next chapter.

7.3 Removing False Alarms According to Texture Analysis Results

Figure 7.5 shows the result map of the Wuda mining area and its surroundings. The thermal anomalies on the map are extracted using a moving window with a size of 10 columns by 10 rows, steps of 1 by 1 in both column and row directions, and a cut-off percentage of 80%. In Figure 7.5, the red channel is filled with the extracted thermal

anomalies. The green and the blue channels are filled by Landsat ETM+ day time band 3 and band 2. The thermal anomalies extracted can be categorised into 4 types. The first type (type W) is caused by water bodies, such as the Yellow River east of Wuda, since water has a high temperature in the night-time image. The second one (type S) is caused by uneven solar heating, such as the white spots located in the north-west of Wuda in the sand dune area, and the magenta pixels located in the mountain area in the south-west and east of Wuda. The third type (type P) is the sparsely distributed red spots around Wuda. They are industrial plants, such as cement factory, electric plant, etc. The fourth type (type F) is the coal fire thermal anomalies. They are located in the central part of the image. The first and the second type of thermal anomalies are false alarms, which can be removed according to the knowledge of characteristics of coal fire thermal anomalies on night-time images gained in paragraph 6.3. The detailed procedure is as follows.

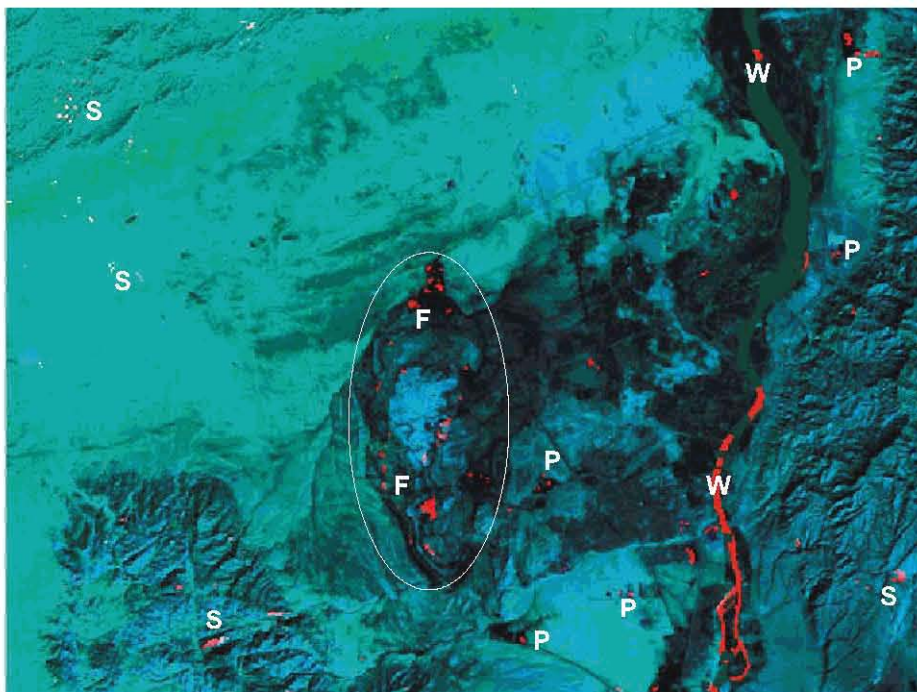


Figure 7.5: Colour Composite image of Wuda (Red: Thermal anomalies extracted from ETM+ night-time band 6; Green: ETM+ band 3; Blue: ETM+ band 2). W: thermal anomalies caused by the water body. S: thermal anomalies caused by solar uneven heating. P: thermal anomalies caused by industrial plants. F: thermal anomalies caused by coal fires.

1. Grouping thermal anomalous pixels into clusters: Thermal anomalous pixels are grouped into clusters according to the 8-connection neighbourhood and an index is given to each thermal cluster. For example, two thermal anomalous pixels will be grouped into one cluster if the two pixels are connected each other in the context of 8-neighbourhood. After this process, the result map becomes a long integer map. The background area is still 0, and every thermal cluster has a distinct digital number.

2. Getting background pixels for each thermal anomalous cluster: for each thermal anomalous cluster, it's surrounding non-anomalous pixels will be sampled as its background pixels. The details are referred to 6.3.

3. Calculation of statistics for each thermal cluster and its background: pixel number, standard deviation and mean for the cluster will be calculated. It should be mentioned here that standard deviation and mean do not apply on a cluster of less than 3 pixels.

4. Fine-tuning the anomaly map: there are three aspects taken into account. The first one is removing thermal clusters occupying a big area. It is known that coal fires in Northwest China will not exceed an area corresponding to 300 pixels in a Landsat-7 ETM+ band 6 image. If a thermal cluster has more than 300 pixels, it can be removed. Considering that normally such a big thermal anomalous cluster is caused by a water body, such as a river or a lake, this process becomes unnecessary, because a thermal anomalous cluster induced by a water body, even with a small pixel number, still can be removed through the next aspect. The second aspect is removing thermal clusters with a lower standard deviation than its background. Thermal anomalies caused by coal fires have a higher standard deviation than their background in a night-time Landsat-7 ETM+ band 6 image according to 6.3. When a thermal cluster has a smaller standard deviation than its background, it is probably formed by a water body or an illuminated slope, since they normally have a homogeneous surface. This kind of thermal cluster can be removed through this process. The third is removing thermal clusters whose mean values do not decrease when more neighbor background pixels join in. Sometimes, a thermal anomalous cluster formed by a water body or solar heating contains less than 3 pixels. Its standard deviation does not exist, so they can not

be deleted through the previous process. These kind of false thermal clusters can be tuned out by this process, which is based on the fact that the mean of a coal fire or a thermal anomaly on ETM+ images is higher than its background and decreases with the increase of number of pixels for background as discussed in 6.3. It should be mentioned here that care should be taken when the fine-tuning processes are applied to a thermal anomalous image. The first aspect is relatively problem free. It is true at least for the North of China, where there is no a single coal fire larger than 1km^2 (278 pixels on ETM+ band 6). The last two aspects should be applied according to the goal of the thermal anomaly extraction. When the extraction aims at the retrieval of the coal fires on a large scale to get a general view of coal fire distribution, these processes should be applied. When the delineation of the thermal anomalies aims on a detailed study of coal fires in a defined area, the last two aspects should be omitted, because the accuracy now becomes important. The false alarms can be removed through the last two steps of fine-tuning process, while a small part of the real anomalies is removed as well.

After the fine-tuning, the final output image only contains few thermal anomalies, having a high chance of being coal fire induced. Figure 7.6 shows the results of the fine-tuning process. In Figure 7.6, A is the original Landsat-7 ETM+ band 6 image. B is the indexed thermal anomalous cluster image. C shows that the river and illuminated slopes have been removed by the standard deviation characteristics. D shows that sparsely distributed small non-fire related thermal clusters have been removed by the mean characteristics.

The method for the automated extraction of coal fire related thermal anomalies in large areas can be formulated, as illustrated in Figure 7.7.

It should be mentioned here that the false alarms can be also removed through land cover information extracted from the multi-spectral channels based on the spectral signatures of the individual surfaces. The combined approach of thermal anomaly extraction and land cover information derivation is successful for coal fire detection in the north of China. The details are explained in the paragraph 8.3 'Detecting unknown coal fires in a previously non-studied area using Landsat-7 ETM+ data'.

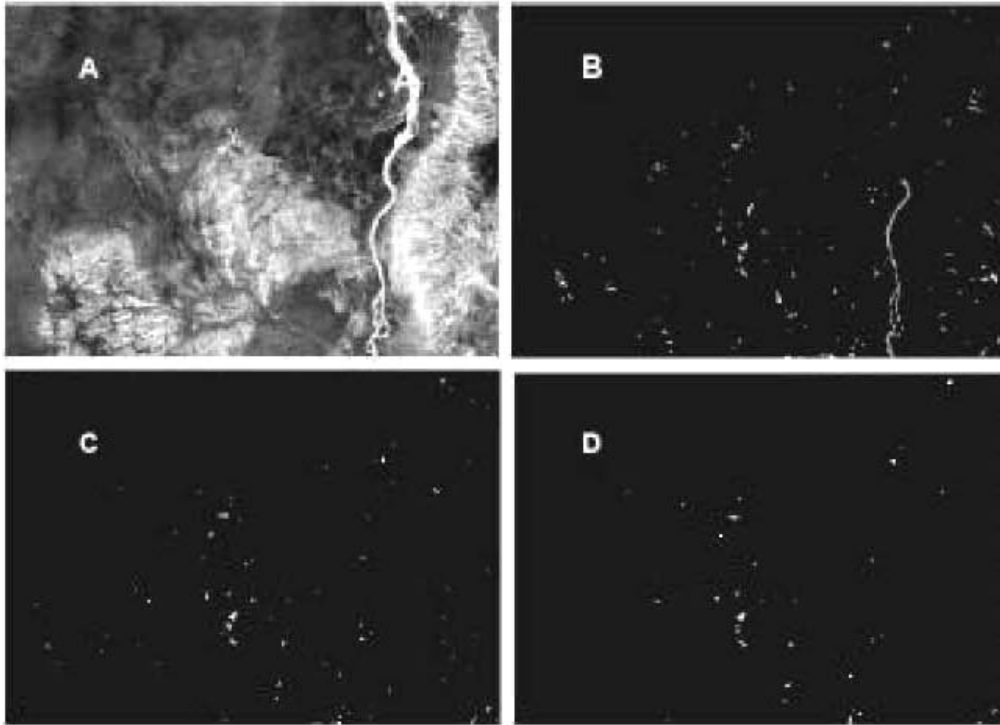


Figure 7.6: Thermal anomaly fine-tuning. A: Original Landsat-7 ETM+ band 6 image; B: Indexed thermal anomalous cluster image. C: Water body and illuminated slopes have been removed by using the standard deviation characteristics. D: Sparsely distributed small non-fire related thermal clusters have been removed by using the mean characteristics.

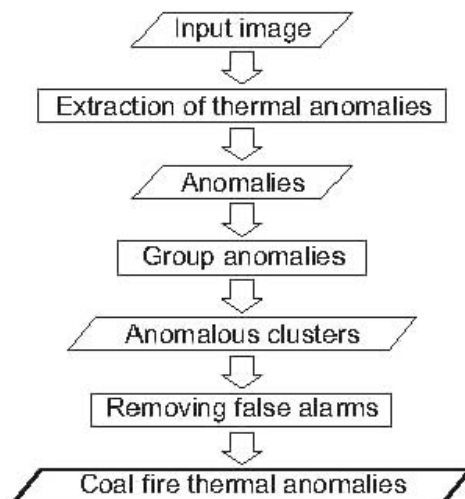


Figure 7.7 Flow chart for the extraction of coal fire related thermal anomalies

7.4 Discussion and Conclusion

Most thermal anomalies formed by coal fires on the surface are smaller than the pixel size of Landsat-7 ETM+ band 6. They form a weak and local thermal anomaly on the image. The thermal anomalies can be automatically extracted in a subset of the image locally. Subsets of an image can be acquired using a window with a small size moving over the image step by step. In such a window, thermal anomalies and their background can be separated through a threshold, which is the first histogram turning point after the mean plus the standard deviation of the window. The threshold keeps false alarms as low as possible. A result map records how many times a pixel in the image has been counted as a thermal anomaly. When a cut-off percentage is set, the result map can be sliced to a bit map for the output with 1 representing coal fire induced thermal anomalies and 0 representing the non-fire area. Furthermore, some false alarms, such as water bodies and slopes heated by the sun, can be removed according to texture analysis based on the known coal fires' texture characteristics.

The performance of the algorithm for the extraction of coal fire related thermal anomalies is dependent on the spatial resolution of the remote sensing sensors, while the result of the algorithm is dependent on the size of the moving window and the final cut-off percentage. What the proper size of the moving window is, and how to choose the right cut-off percentage to achieve the best output result still needs to be studied. This is discussed in the next chapter.

Chapter 8 RESULT EVALUATION AND VALIDATION

8.1 Assessment of the Algorithm for the Extraction of Coal Fire Related Thermal Anomalies

The algorithm for extracting thermal anomalies related to coal fires described in the previous chapter can run automatically over an image. Accurate results can be acquired only when the parameters are correctly set. These parameters include the size of the moving window and cut-off percentage for the result bit map. Before we continue to use the algorithm running on one or more scenes of Landsat-7 ETM+ band 6 images for detection of coal fires in a large area, or on a partial scene for quantifying characteristics of coal fires in a small area, an assessment of the algorithm performance including the influences from the parameters needs to be conducted.

8.1.1 Data input

1. Landsat-7 ETM+ band 6 image: night-time Landsat-7 ETM+ band 6 data in Wuda area with 1024 columns and 512 rows are used in the study (See Figure 8.1 A). The data are a subset of scene 226-211 (pass-row) acquired on the night of 28 September 2002 (Night2002 in 6.3). The best known area, Wuda area, covers 200 columns by 100 rows in the image.

2. Interpreted thermal anomaly image: this is a bit map (1-fire, 0-background), whose thermal anomalies are manually interpreted from the same night-time Landsat-7 ETM+ band 6 data based on field observations (AnoNight2002 in 6.3). It represents the known coal fire related thermal anomalies, which can be detected by the image.

8.1.2 Methodology and data processing

1. Extracting thermal anomalies using different moving window sizes: window sizes from 3*3, 5*5, 7*7, up to 51*51 (columns and rows) are used to extract thermal anomalies from the night-time Landsat-7 ETM+ band 6 data in Wuda. Keeping the window size in odd numbers defines a center pixel of the window, where the threshold of the window is recorded. The result is a 25-layer long integer image. Layers are

correspondent with window sizes. For example, the first layer represents the result for the 3*3 moving window, while the 25th layer represents the result for the 51*51 moving window. In the layer, the digital number is equal to the times the pixel has been counted as a thermal anomaly regarding to the moving window concept. For instance, a pixel with a digital number of 8 in the first layer means that the pixel has been sampled $3*3=9$ times and regarded as a thermal anomaly 8 times. Layer 1, 13 and 25, equal to window size 3*3, 27*27 and 51*51 are shown in Figure 8.1. Their threshold images are shown in Figure 8.2.

The maximum value in the first layer is 9, the second is 25, the third 49, and the 25th layer is 2601. Each layer is normalized to the same maximum value as the 25th layer through its DN value times 2601 divided by the maximum value of the layer. After the normalization, all 25 layers are summed up to produce the 26th layer as shown in Figure 8.3, which represents a kind of accumulation of the moving window results. Its simulated threshold image can be calculated as the mean of the 25 layers' threshold images. It is shown in Figure 8.3 B.

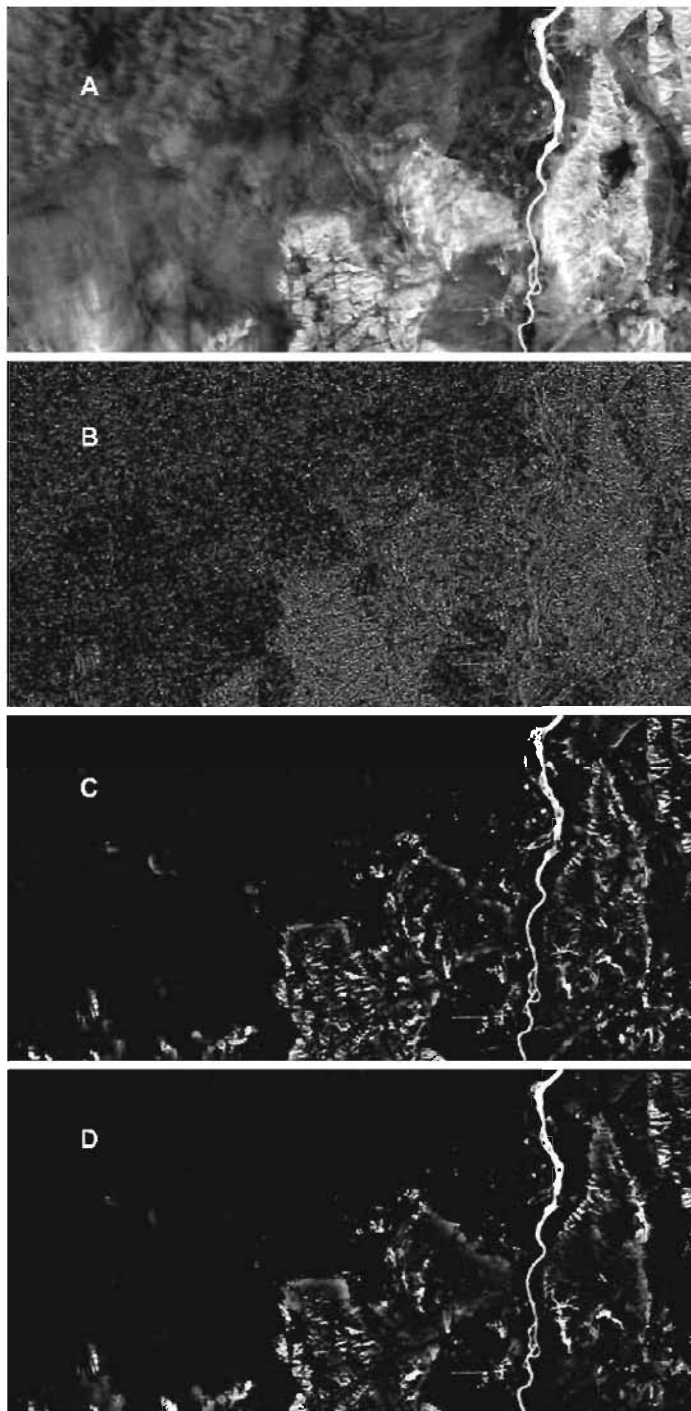


Figure 8.1 Thermal anomalies extracted using different moving window sizes. A: Input image; B: Thermal anomalies extracted by a 3*3 moving window; C: Thermal anomalies extracted by a 27*27 moving window; D: Thermal anomalies extracted by a 51*51 moving window.

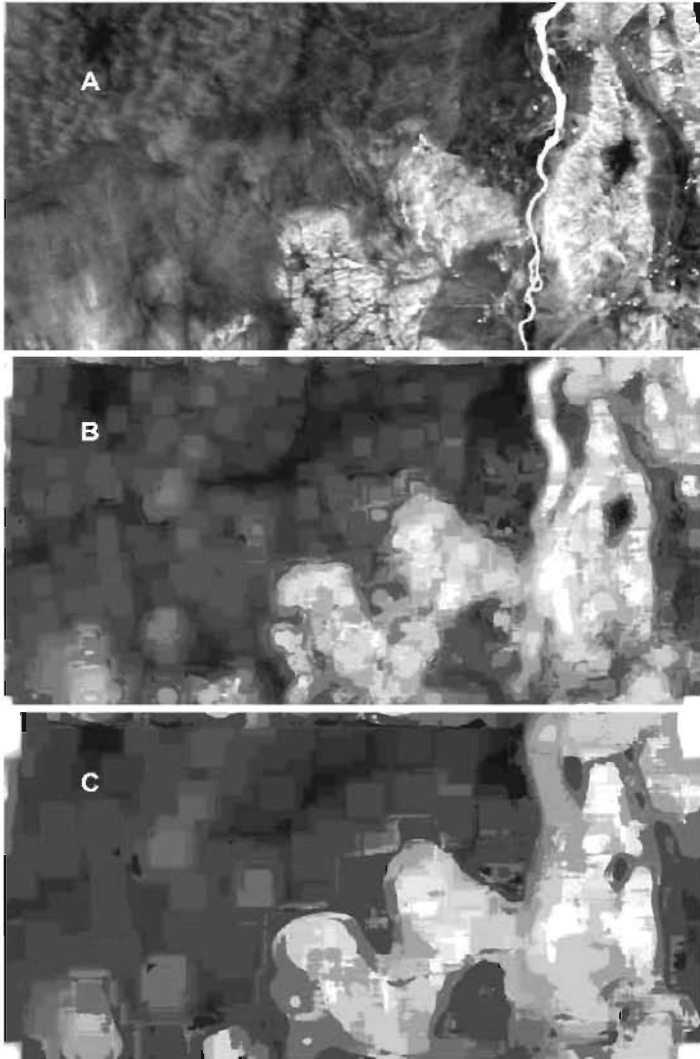


Figure 8.2 Threshold images for thermal anomaly extraction using different moving window sizes. **A:** Threshold image of the 3*3 moving window; **B:** Threshold image of the 27*27 moving window; **C:** Threshold image of the 51*51 moving window.

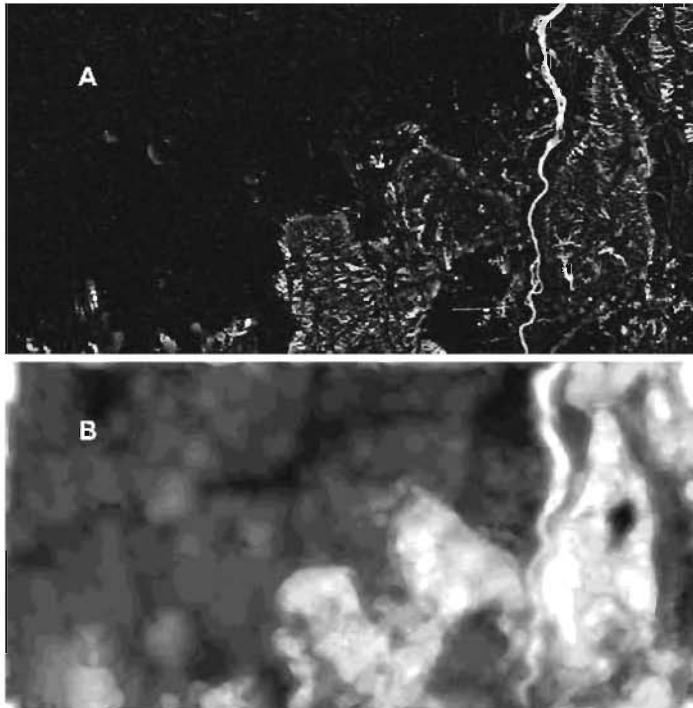


Figure 8.3 A thermal anomaly image and a threshold image. A: Sum of the normalized thermal anomaly images for window size 3*3 to 51*51 with an interval of 2*2. B: Mean of the threshold images for window size 3*3 to 51*51 with interval of 2*2.

2. Producing result bit maps using different cut-off percentages: for the total 26 thermal anomaly layers, cut-off percentages of 50%, 55%, 60%, 65%, 70%, 75%, 80%, 85%, 90%, and 95% are used to produce the result bit maps (total 260 maps). When the cut-off percentage is set low, for example, as 50%, there will be more thermal anomalous pixels extracted by the moving window method assigned as 1 in the output image. The result image will include more thermal anomalies. When it set high, such as 90%, there will be less thermal anomalies in the output image. The result looks 'clean'. Figure 8.4 shows the result map for the 13th layer (window size 27*27) by using cut-off percentage of 50%, 70% and 90% respectively.

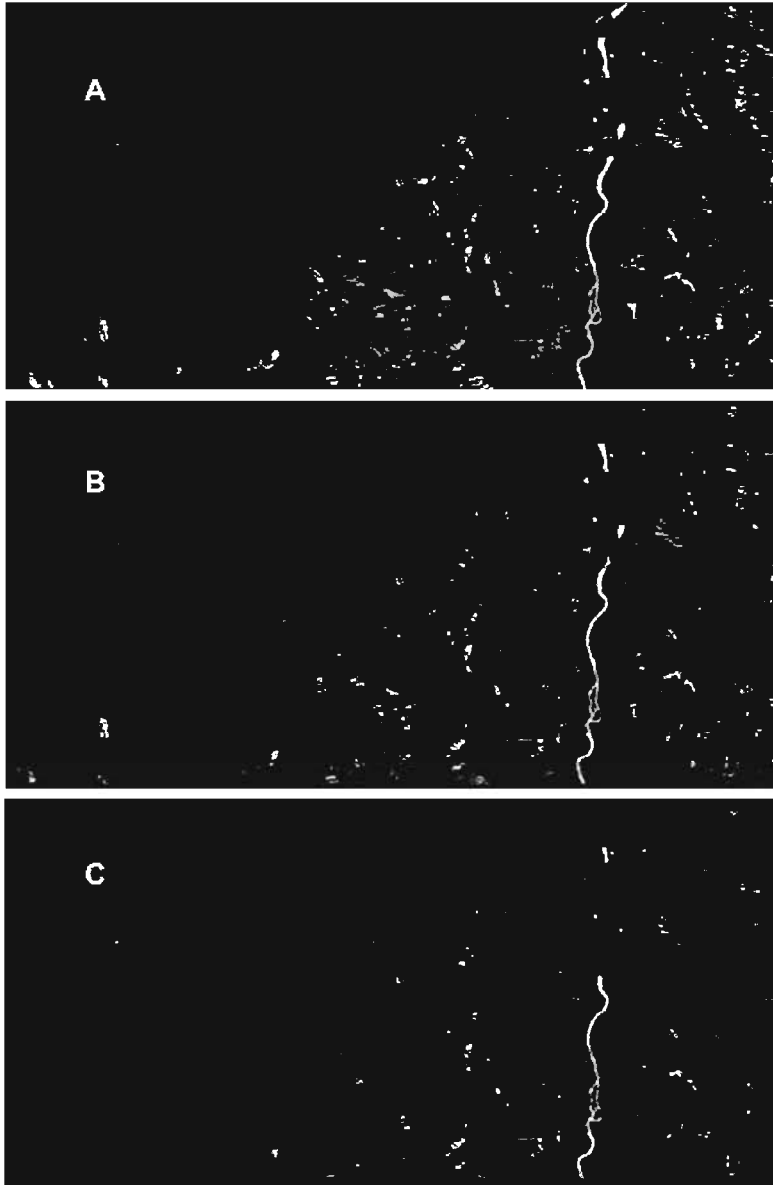


Figure 8.4 Result maps for different cut-off percentages. A: cut-off percentage 50%; B: cut-off percentage 70%; C: cut-off percentage 90%.

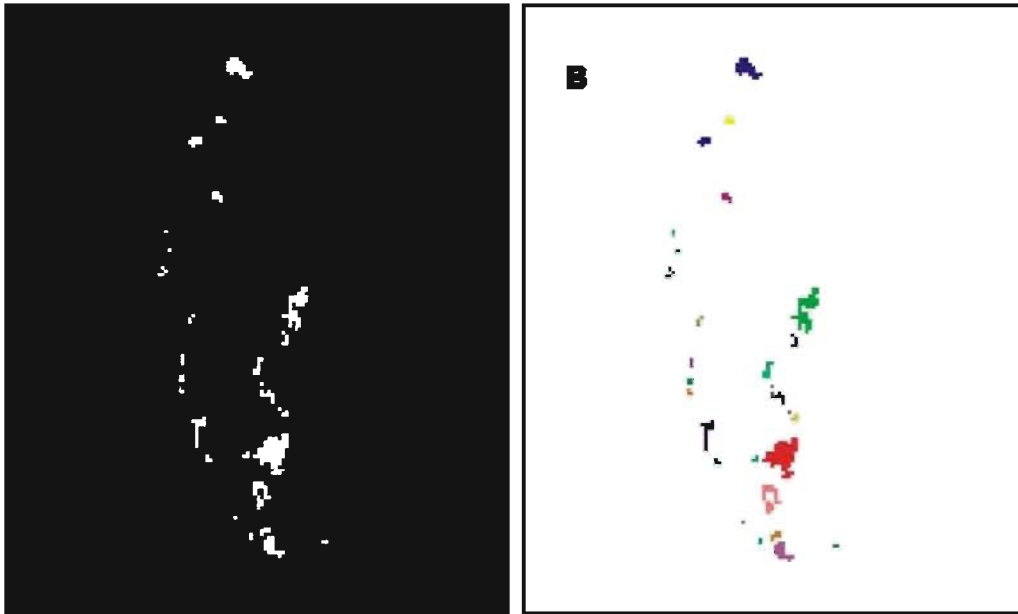


Figure 8.5 Interpreted thermal anomaly image in Wuda. A: Bit map. B: Clustered map.

3. **Grouping the interpreted thermal anomaly image into clusters:** the interpreted thermal anomaly image in Wuda (See Figure 8.5A) has 264 thermal anomalous pixels. They are grouped into 28 clusters according to the 8-connection neighborhood and a distinct index is given to each cluster (See Figure 8.5B). The number of pixels for each cluster is indicated in table 7.1.

C. Index	1	2	3	4	5	6	7	8	9	10	11	12	13	14	15
P. Number	27	5	8	6	1	1	4	42	3	5	3	8	4	1	3
C. Index	16	17	18	19	20	21	22	23	24	25	26	27	28	Total	
P. Number	8	1	3	14	64	3	3	19	1	6	2	17	2	264	

Table 7.1 Pixel number of clusters for the interpreted thermal anomaly image in Wuda.

C. Index: Cluster Index; P. Number: Pixel Number.

4. **Calculating parameters for evaluation of the performance of the algorithm:** To evaluate the performance of the 260 result bit maps, 5 parameters are defined. The first one is the number of the correctly detected pixels (D), which answers how many pixels in each cluster in the interpreted thermal anomaly image are shown in the result bit map. The second parameter is the number of the total detected pixels (T), which is the

number of the total thermal anomalous pixels in the result bit map in Wuda area (1024 columns * 512 rows). The third one is the number of false alarms (F):

$$F = T - D$$

The fourth one is the percentage of the correct detection (DP):

$$DP = \frac{D}{C}$$

where C is the total pixel number of the fire cluster listed in table 7.1.

The fifth parameter is an integrated index (I):

$$I = \frac{D}{C} \times \frac{D}{T}$$

A high value of I represents a high number of pixels in the result bit map which are correctly detected, while there is a low number of false alarms.

8.1.3 Results and discussions

1 Assessment of the algorithm performing at different window sizes and cut-off percentages for the extraction of coal fire related thermal anomalies in Wuda area: the percentage of the correct detection (parameter DP) of each result bit map (total 260) has been plotted for each cluster listed in Table 7.1. In Figure 8.6, the upper map shows the DP of each result bit map for the detection of the known cluster (Index 8) with 42 pixels. The Y-axis represents the number of DP in percent. When it equals to 0, none of the known 42 thermal anomalous pixels of the cluster (Index 8) have been detected on the result bit map. When it equals to 100, all of the known pixels of the cluster have been detected. The X-axis represents the 260 result bit maps. Marks are given from 3, 5, 7, and so forth, up to 51 and A. The numbers represent the window size. For example, 3 means the size of the moving window is 3*3. The last one, 'A', means the accumulation size of the moving window. Within each window, ten points are plotted. They represent the cut-off percentages. The first point in the left corresponds with the cut-off percentage of 50%, and the last one is 95%. As shown in

the figure, these ten points always decline from the first to the last. If we only consider the result bit maps with both the cut-off percentage and the DP higher or equal to 70%, it is found that all these result bit maps are located within the window size from 17*17 to 41*41. This window range is suitable for extracting thermal anomalous clusters with about forty pixels in Wuda area. Furthermore, the best window size for the extraction is 19*19. When it is used, the cut-off percentage can be set as high as 90%, with still 90% of the known pixels detected. The center map in Figure 8.6 shows the average DP of the 260 result bit maps for extracting thermal anomalous pixels from 3 known clusters with 8 pixels. The suitable window sizes range from 9*9 to 41*41. The best window size is 15*15. To detect thermal anomalous cluster with only one pixel, the best window size is 11*11. Suitable sizes for the moving window are from 3*3 to 37*37, as shown in the lower map in Figure 8.6, which shows the average DP for the detection of 5 known anomalous clusters with 1 pixel.

2 Selection of the suitable size of the moving window for the detection of coal fire related thermal anomalies in Northwest of China: the integrated index (the fifth parameter I) of each result bit map (total 260) for the detection of the whole 28 clusters in Wuda area has been plotted in the same way as the DP and is shown in Figure 8.7. The black line and the arrow in black represent the cut-off percentage of 70%, in red 80% and in green 90%. In the window among 11*11 to 43*43, the value of I is higher than the other window sizes. When they are used to detect coal fire thermal anomalies in Wuda area, the result bit maps have relatively high accuracy and a low number of false alarms. Out of this window range, the values of I do not increase with an increase of cut-off percentage, which means that the cut-off percentage does not play a key role in the result bit map any more. At the end part of the figure, it is found that after the accumulation of the window sizes, I has a high value, especially at the result bit map for the cut-off percentage 70.

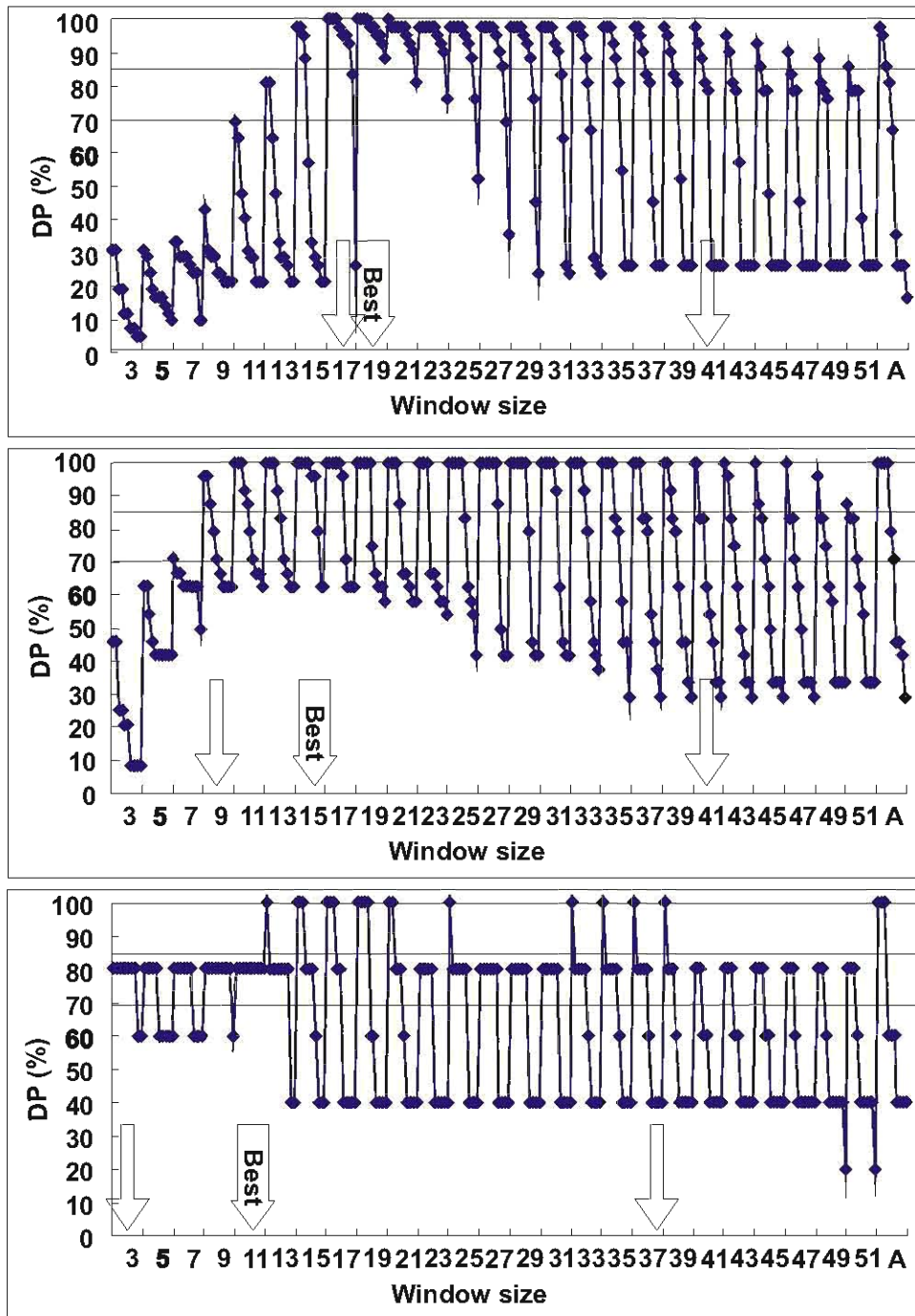


Figure 8.6 Evaluation of window size and cut-off percentage for the extraction of thermal anomalous pixels in the clusters with different amounts of pixels; Upper: Cluster 8 with 42 known thermal anomalous pixels; Middle: Average of 3 clusters with 8 known thermal anomalous pixels; Lower: Average of 5 clusters with 1 known thermal anomalous pixel.

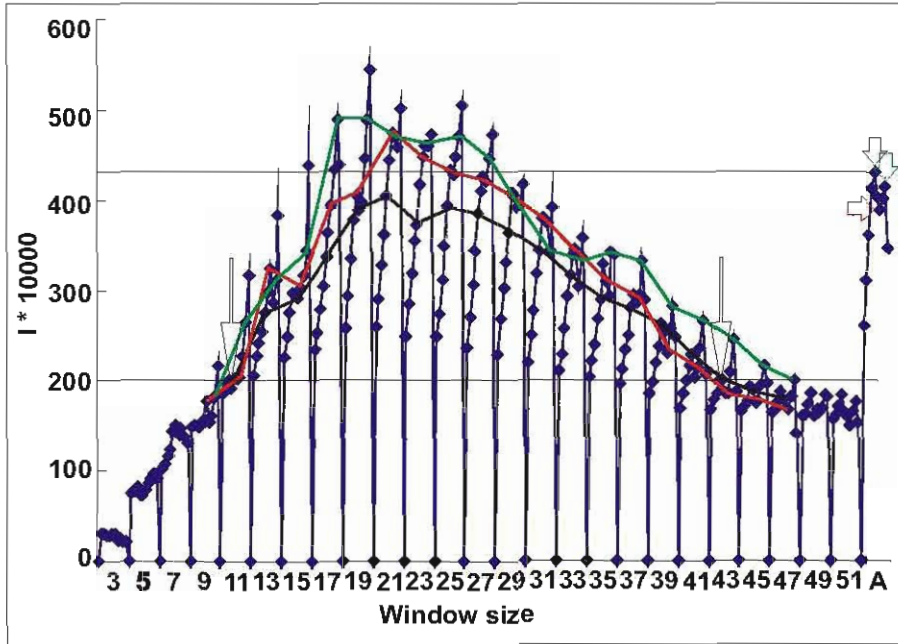


Figure 8.7 Evaluation of window size and cut-off percentage for the extraction of thermal anomalous pixels vs. false alarms in the Wuda area. Black: cut-off percentage 70%; Red: cut-off percentage 80%; Green: cut-off percentage 90%.

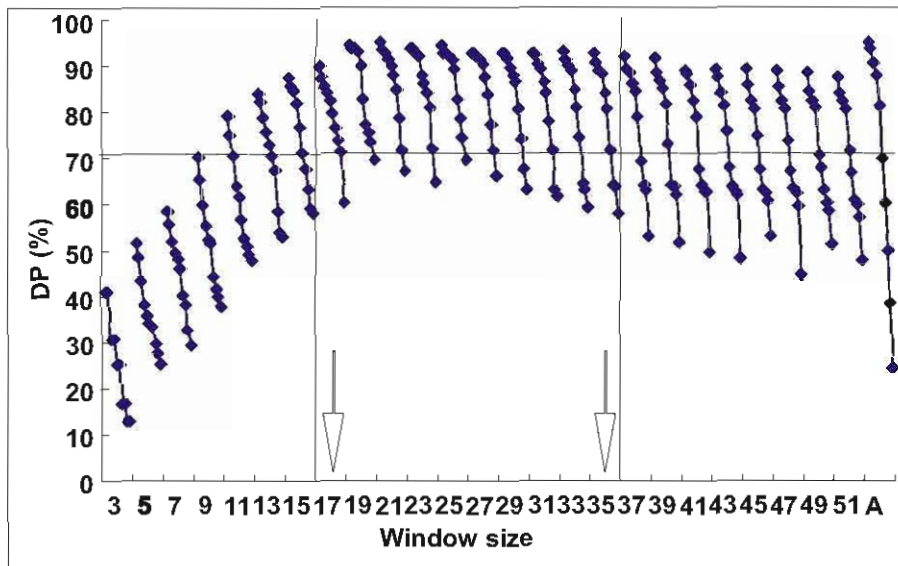


Figure 8.8 Accuracy evaluation of window size and cut-off percentage for the extraction of thermal anomalous pixels in the Wuda area. Accurate result can be acquired by using the 17*17 to 35*35 moving windows.

Figure 8.8 shows the DP value of the 260 result bit maps for detecting the total 264 known thermal anomalous pixels in the Wuda area. It is found that some result bit maps do have a good performance for detecting the known thermal anomalous pixels in the area, especially the result bit maps in the window range between 17*17 and 35*35. Over 70% of the known thermal anomalous pixels can be detected by the result bit maps with a cut-off percentage of 80%. The result bit maps with lower cut-off percentage can even extract over 90% of the total anomalous pixels.

The number of thermal anomalous pixels related to coal fires detected by the algorithm is dependent on three factors. The first two are the size of the moving window and the cut-off percentage, which have already been discussed. The other one is the contrast between the coal fire and its background. If the contrast is high, the pixel will be definitely detected. Most coal fires, especially at the start stage, can not form such a strong thermal anomalous pixel due to the spatial extension of the fires and the spatial resolution of the image. Then the detection of the low contrast thermal anomalous pixels becomes important. The first two factors need to be taken into account.

Coal fires in Wuda are quite diverse. They form strong thermal anomalies as well as weak thermal anomalies. They have big spatial extents as well as small extents. They include new coal fires as well as fires that have been burning for decades. The suitable size of the moving window for Wuda can be used as a representative for the North of China. The suitable size of the moving window for the detection of coal fires in Wuda are between 17*17 and 35*35. The best window size for the extraction of one pixel thermal cluster is 11*11. Window accumulation gives good results. It can be concluded here that the suitable size of the moving window for the detection of coal fires in northern China is the accumulation window from 11*11 to 35*35.

3 Use of the multi-cut-off percentage in the final output image: a high setting of the cut-off percentage detects less thermal anomalous pixels related to coal fires, as well as false alarms, but the pixels detected have a high chance of representing coal fires. On the contrary, a low setting detects more thermal anomalous pixels related to coal fires. It gives a more accurate result for the spatial extension of the coal fire, but false alarms detected increase. To detect unknown coal fires in a previously not studied area or for

detecting coal fires in a large area, we prefer to use a higher setting of the cut-off percentage to produce a relatively simple final output. For the quantity of coal fires in the known coal fire area, we prefer to use a lower setting to make a more accurate result, for the false alarms will not divert our attention from the real coal fires. These two kinds of results can be presented in a single final output image if we do not keep the final output image as a 0-1 bit map. For example, the final result map can include three classes: background, a class from the result by using a low cut-off percentage of 70%, and a class from the result by using a high cut-off percentage of 85%.

8.1.4 Conclusions

1. Thermal anomalous clusters with different pixel numbers (0 to 64 in the Wuda area) can be well extracted by the algorithm using different moving window sizes. Sometimes 100% of the thermal anomalous pixels in a cluster can be delineated.
2. The best size of the moving window for extracting thermal anomalies related to coal fires in the Wuda area is ranging from 17*17 to 35*35. Above 70% of the known thermal anomalous pixels can be extracted. At the mean time, the false alarms are minimized.
3. The best size of the moving window for detecting coal fires in a large area of China is the accumulation window ranging from 11*11 to 35*35.

8.2 Validation of Results for Applying the Algorithm to Other ETM+ Images

The algorithm for extracting thermal anomalies related to coal fires has been evaluated in the last paragraph. It was developed based on the scene acquired in 2001, and it has a good performance for the scene in 2002. Both scenes are acquired during night-time and cover the same study area. In this paragraph, the algorithm is applied to a day time scene in the Wuda area, and a night-time scene covering an area in Xinjiang Uygur Autonomous Region, China.

8.2.1 Validation of the result for the extraction of thermal anomalies related to coal fires in Xinjiang

A scene of the Landsat-7 ETM+ (path/row: 3/215) band 6 data acquired during night-time on 1 January 2000 is used as the input image. It has 3300 columns and 3000 rows, covering an area of about 180km*180km in the northeast of the Urumqi, the capital city of the Xinjiang Uygur Autonomous Region.

The algorithm developed in the previous chapter is used to detect thermal anomalous pixels related to coal fires from the data. During the process, the size for the moving window was set at 11*11, 19*19, 27*27 and 35*35. The result bit maps were normalized and accumulated. Two cut-off percentages are set at 70% and 85%.

In Figure 8.9 the upper image shows a subset of the input scene of the band 6 (high gain) data. It has a dimension of 1024 columns and 512 rows, covering an area of about 60km* 30km. The area is located 100km away from Urumqi in the Northeast and about 2500km away from the Wuda area. It is the only mountainous area in the scene. The rest of the scene is a desert area. The lower map in Figure 8.9 shows the output result map for the extraction of coal fire related thermal anomalies using the algorithm. In the map, the background area is in white color. The red pixels are related to the cut-off percentage of 85%, and the green ones are correspondent to the cut-off percentage of 70%.

The image shows that there are only 11 clusters (pixels in red colour) with a high possibility to be coal fires. Two of them, as pointed by the arrows, were coal fires, which were investigated during a field campaign in 1996. They were most probably still burning in the year 2000 when the image was acquired. Four thermal clusters marked by letter 'F' in the result map are located in the area close to the coal seam outcrops. These are probably coal fires also. The other five thermal anomalous clusters marked by letter 'P' are probably caused by industrial plants, because they are located in the alluvial fan area, which is normally are the most common place for settlement and industry. The performance of the algorithm is acceptable.

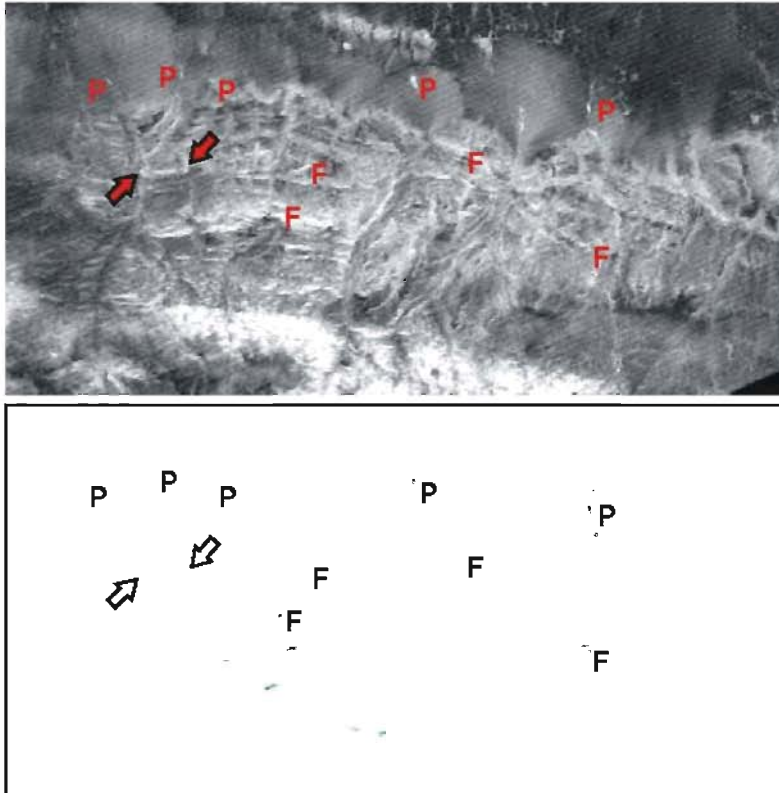


Figure 8.9 Extraction of thermal anomalies in Xinjiang, China. Top: The original Landsat-7 ETM+ band 6 data. Bottom: Result map of thermal anomalies extracted by the algorithm. Red: thermal anomalous pixels with a high possibility to be caused by coal fires. Green: thermal anomalous pixels possibly caused by coal fires.

8.2.2 Validation of result for the extraction of thermal anomalies related to coal fires using day time ETM+ band 6 data in the Wuda area

A day time Landsat-7 ETM+ band 6 image acquired on 21 September 2002 of path/row 129/33 (Day2002 in 6.3) is used as the input. Thermal anomalies are delineated using the algorithm as described before.

Figure 8.10A shows the original image in the Wuda area with 1024 columns and 512 rows. The red pixels in Figure 8.10B are thermal anomalous pixels extracted using the cut-off percentage of 85%. They are concentrated in the Wuda syncline area, as well as in the mountainous area in the East of the Yellow River. Most of the thermal anomalous pixels are interpreted as false alarms formed by heated slopes. When the threshold of the moving window is changed from the first turning point after the mean plus two times standard deviation, false alarms caused by solar uneven heating in the mountainous area are removed, as shown in Figure 8.10C, where the red pixels are related to a cut-off percentage of 85%, magenta 70% and cyan 50%. Only a few of red pixels exist in the map as marked by the arrows. The day time image detects few coal fires in the Wuda area. This is mainly because the scene is acquired during summer. During day time in summer, the temperature contrast between coal fires and background is low, so less coal fires can be detected. It is expected that a day time image received in winter time will improve the result.

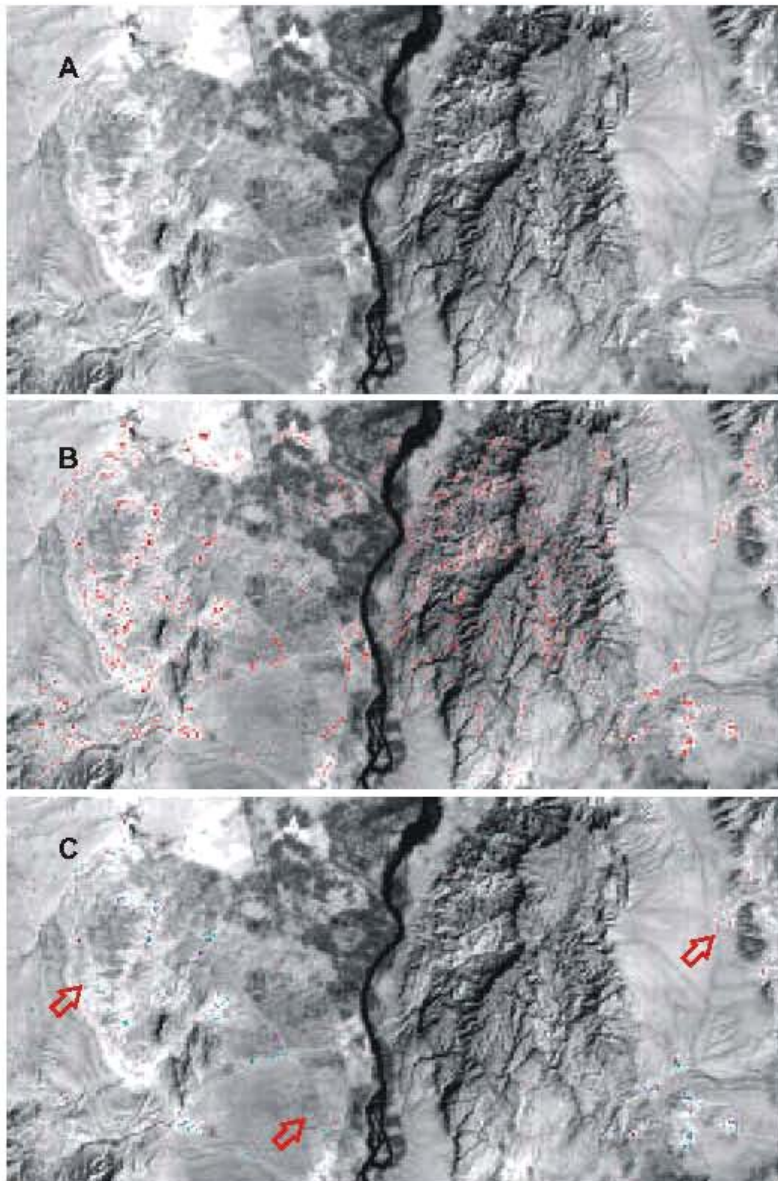


Figure 8.10 Extraction of thermal anomalies in a day time image in the Wuda area. **A:** The original Landsat-7 ETM+ band 6 data. **B:** Thermal anomalies extracted by the algorithm using the starting point at mean plus standard deviation. Red: thermal anomalous pixels; **C:** Thermal anomalies extracted by the algorithm using the starting point at the mean plus two times the standard deviation. Red: cut-off percentage: 85%; Magenta: cut-off percentage: 70%; Cyan: cut-off percentage: 50%.

8.3 Detecting Unknown Coal Fires in a Previously Non-studied Area using Landsat-7 ETM+ Data

8.3.1 Methodology

A Landsat-7 ETM+ scene of path 226, row 211 acquired on September 29th 2002 was used for thermal anomaly extraction. A correspondent day time scene of path 133, row 129 from September 21st 2002 was used for multi spectral analysis. The study area covers an area of 8100 km².

Both scenes were georeferenced based on very precise GPS-derived vector data from a field campaign in September 2002. The data was also orthorectified to minimize terrain induced displacements based on digital elevation models produced from 25m resolution ERS-2 SAR data. The multispectral data was furthermore atmospherically corrected using ATCOR-3 (Richter 1998), to suppress atmospheric and topography induced illumination effects.

Coal fire related thermal anomalies were automatically extracted from the input night-time image using the algorithm mentioned in the above paragraph. During the process, the size of the moving window was chosen as the accumulated window from 11*11, 19*19, 27*27, and 35*35. The cut-off percentage was chosen as 70%. The thermal anomaly result is shown in magenta colour in Figure 8.11.

From the multi-spectral ETM+ channels land cover information can be extracted based on the spectral signatures of the individual surfaces. To understand the spectral behaviour of the surfaces, characterizing the areas studied, surface and laboratory spectra were collected with a GER3700 field spectrometer during a ground truthing campaign in September 2002. The different land cover classes derived from the image can be seen in the legend of Figure 8.11. For coal fire area demarcation it is assumed, that the signature 'coal' plays a major role. At risk for coal fires are abandoned and active mines, coal seams, coal waste piles, coal storage piles or coal washery discard. Coal fires can therefore only occur in the vicinity of outcropping coal seams, coal waste or coal storage piles and related coal accumulations. Hence, the detection of the signature 'coal' and knowledge of the distribution of coal is crucial for the demarcation

of possible coal fire and coal fire risk areas. Even though coal fires occur underground and the thermal anomalies may not be located directly related to the coal signature (e.g. a sandstone layer, which is overlaying a burning coal seam) coal fires are restricted to a certain depth. In general, coal fires occur no deeper than approximately 150 m underground. Taking this fact, a buffer zone around the detected coal signature demarcating the area, in which coal fires are possible at all, can be generated (Kuenzer et al. 2003).

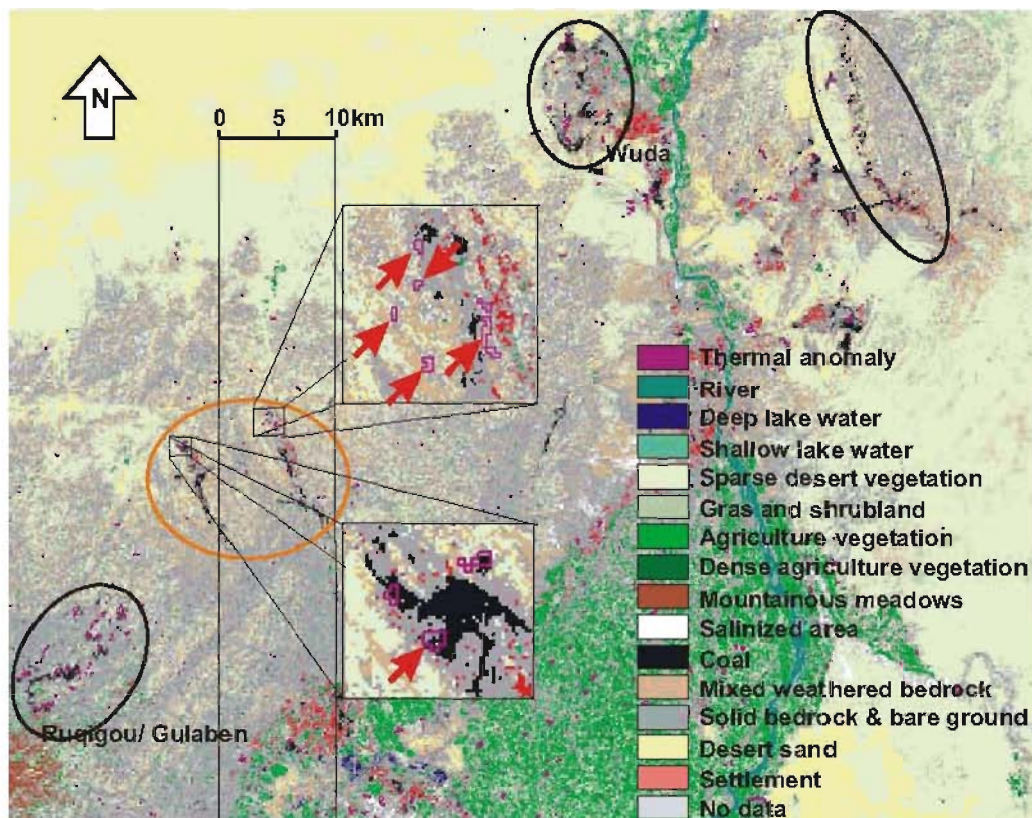


Figure 8.11: Combination map of thermal anomalies and land cover characteristics. Thermal anomalies are automatically derived from night-time Landsat 7 ETM+ thermal band. Land cover information is extracted based on the spectral signatures using daytime non-thermal bands. Four circled areas are interpreted as favourable places for coal fire occurrence. The area marked in orange is the newly detected coal fire area. In the upper amplified window the red arrows point at the five thermal anomalies that have been verified in the field as coal seam fires, while in the lower one the arrow points on the thermal anomalies formed by coal waste pile fires.

This buffer zone can also help to exclude thermal anomalies detected by the automated thermal extraction, which show a similar behaviour like coal fires (thermal anomalies from industry, settlements etc.) but are not located within possible coal fire areas (Kuenzer et al. 2003).

8.3.2 Results

The combination of the information automatically extracted from thermal as well as non-thermal multispectral data can support the demarcation of areas with a high potential for coal fire occurrence. As it can be seen in Figure 8.11, four major areas for coal fire occurrence were located. The northernmost area close to the city of Wuda hosts several coal fires already well known. The same applies for the westernmost area Ruqigou and Gulaben being well studied and also containing several well known coal fires. Areas never investigated so far are the north south striking coal outcrops east of the Yellow River and the coal outcrops in two valleys, running parallel to each other from Northwest to Southeast, approximately 50km southwest of Wuda. This area is marked in orange. In Figure 8.11 it can be seen that all four areas contain several thermal anomalies. The ones in the Wuda and Ruqigou / Gulaben areas were expected to show up, since the location of coal fires there is well known. The other areas, where coal signatures and thermal anomalies matched spatially, were inspected during the field campaign in 2003.

On September 13th 2003 a field trip was organized to the very remote area marked in orange. The coal fire fighting team of Wuda, joining on the survey, did not know about the area visited beforehand, nor did they have any information on possible coal fires in that region. Once arrived in the area, which is only accessible via dirt roads and very sparsely settled, we could receive information from the local inhabitants. The region once was a prospering coal mining area but production has been decreased drastically due to financial problems.

With the help of GPS, the six thermal anomalies, extracted from the satellite data, were located within an area of very rugged terrain of former coal waste piles, abandoned mines and heavily disturbed coal outcrops. Five of the thermal anomalies proved to be coal fires in an actual coal seam, while the other anomaly resulted from fires in a coal

waste pile. Therefore all six anomalies could be verified as coal fire anomalies. In this coal fire area, the fire temperatures range from 170 to 340 °C. At the mean time, pyro-metamorphic rocks, and fumarolic minerals such as sulphur (S) and salmiac (NH_4Cl) can be seen on the surface (See Figure 8.12).



Figure 8.12: A newly detected coal fire in a previously non-studied area. The arrow points at the location where a fire is burning underground.

8.3.3 Discussion and Conclusion

The discovery of formerly unknown coal fires from remote sensing data exclusively shows that the combined approach of thermal anomaly extraction and land cover information derivation is successful.

The algorithm could work on the data from different sensors. Thermal and land cover information can also be derived from Landsat-5 TM, ASTER, ALI, or MODIS data.

Chapter 9 CONCLUSIONS & OUTLOOK

A practical approach for the extraction of coal fire related thermal anomalies in a large area has been developed. The algorithm runs automatically, is able to investigate unknown areas, and results are transferable to different images. This makes it possible to set up an operational detection and monitoring system for coal fires in larger areas, such as the North of China.

9.1 Conclusions

With respect to objective 1 'Analysis of thermal characteristics for coal fires and their background', the following conclusions can be drawn:

1. The interior temperature for the simulated surface coal fire is about 1000°C, which can heat the surroundings through mainly convection in the proximity of 2 meters and form a thermal anomaly of 1°C difference. It is hard for the coal fire to heat an area in over 4.5m distance. For the simulated underground coal fire, the interior temperature could reach above 1200°C. The surface radiant temperature for the simulated coal fires range from 300 to 900°C. Within 1 hour heat could be transported through a 0.5 meter high sand cone to the surface to form a thermal anomaly with a temperature about 3°C higher than background.
2. Diurnal radiant temperature variations for different surface types showed the same trend: High radiant temperatures during daytime and low temperatures during night-time. When using thermal remote sensing data to detect coal fires, the factors of relief, vegetation, soil moisture, etc. often produce anomalies on imagery which for our purpose are noise and needs to be recognized or eliminated. Surface temperature in a sand dune could vary 28°C within the sand dune. In a coal dump pile, temperature for a slope facing Southeast could be 20°C higher than that for a slope facing North between 10:00 to 14:00. The temperature variance caused by uneven solar heating can mask thermal anomalies related to coal fires.
3. Underground coal fires can form thermal anomalies above the covering bedrocks on the surface. These anomalies can be observed during night-time only. Predawn is the

best time for coal fire detection using thermal remote sensing techniques. Underground temperature profiles showed that one hour past sunrise, a thermal anomaly expected to exist 1m away from the coal fire's crack was covered by the effects of solar uneven heating. Heat from the sun can reach 3.2cm below the sand surface two hours after sunrise. Thermal anomalies did not extend for more than 3m from the crack. The width of the thermal anomaly does not decline with increasing background temperature. The thermal pattern in remote sensing as well as field data above a coal fire actually is the pattern of cracks.

4. The minimum, median and mean values of a coal fire cluster or a thermal anomaly cluster on ETM+ images are not only higher than for the correspondent background, but also decrease with the increase of the accounted background area. Standard deviation of a coal fire cluster or a thermal anomaly cluster on night-time ETM+ images is higher than of the background. On daytime ETM+ images the standard deviation is smaller than that for the background.

Coal fires form thermal anomalies on images with their distinct start and end DN values. During the detection, every coal fire should be analysed individually. ETM+ night-time images are suitable for a general survey of coal fires in large areas. About eighty percent of the known coal fires can be detected.

With respect to objective 2 'Development of a practical approach for the extraction of coal fire related thermal anomalies in a large area', the following conclusions can be drawn:

1. A practical approach for the extraction of coal fire related thermal anomalies in a large area using Landsat-7 band 6 data has been developed. Most of coal fire formed thermal anomalies on the surface are smaller than one pixel of Landsat-7 ETM+ band 6. They form a kind of weak and local thermal anomaly on the image. The thermal anomalies can be extracted in a subset of the image locally. Subsets of an image can be acquired using a moving window of a small size moving over the image step by step. In a window, thermal anomalies and their background can be separated through a threshold, which is the first histogram turning point after the mean plus the standard deviation of the window. The threshold keeps the false alarms as low as possible. A

result map records how many times a pixel in the image has been counted as a thermal anomaly. When a threshold is set, the result map can be sliced to a bit map for the output with 1 representing coal fire induced thermal anomalies and 0 representing the non-fire area. Furthermore, some false alarms, such as water bodies and slopes heated by the sun, can be removed according to texture analysis based on the known coal fires' texture characteristics.

2. The background temperature, the quality of the thermal remote sensing data, and the magnitude of the coal fires are the factors which determine the detection capability of coal fires. The performance of the algorithm for the extraction of coal fire related thermal anomalies is independent on these factors, while the result of the algorithm is dependent on the size of the moving window and the cut-off percentage. Thermal anomalous clusters with different pixel numbers (0 to 64 in the Wuda area) can be extracted well by the algorithm using different sizes of the moving window. Sometimes 100% of the thermal anomalous pixels in a cluster can be delineated. The best size of the moving window for detecting coal fire in a large area in the North of China is the accumulation window ranging from 11*11 to 35*35 for Landsat-7 ETM+ band 6 data.

9.2 Outlook

1. Coal fire detection includes isolating coal fire areas, locating the front of coal fires, calculating the depth and the age of coal fires. Thermal anomalies on the surface, as well as in an image, are direct indicators for active coal fires. Surface temperature of these thermal anomalies could be calculated according to Plank's formula. The front, depth, and age of a fire can be obtained from coal fire thermal models (Cassells & van Genderen, 1995; Cassells et al., 1996).

2. The current development of the partial failure of Landsat-7 is a worry for future thermal research, nevertheless, the algorithm presented could work for other sensors. Thermal anomalies could also be derived from Landsat-5 TM, or ASTER data, showing the robustness of the algorithm on different spatial and spectral scales.

3. The discovery of formerly unknown coal fires from remote sensing data exclusively proves that the combined approach of thermal anomaly extraction and land cover information derivation is successful. It is an important step towards the setting up of an operational detection and monitoring system for coal fires in the large area of northern China.

REFERENCES

- Abbott W. E. (1918) Mount Wingen and the Wingen Coal Measures. Angus and Robertson, Sydney, N.S.W. Australia.
- Abrams M., Glaze L., Sheridan M. (1991) Monitoring Colima Volcano, Mexico, Using satellite data. *Bulletin Volcanology*, **53**, 571-574.
- Andres R.J. & Rose W.I. (1995) Description of thermal anomalies on two active Guatemalan volcanoes using Landsat thematic Mapper imagery. *Photogrammetric Engineering and Remote Sensing*, **61**, 775-782.
- Bhattacharya A., Reddy S., and Mukherjee, T. (1991) Multi-tier remote sensing data analysis for coal fire mapping in Jharia coal field of Bihar, India. *Asian Conference on Remote Sensing, Singapore*, Vol.I, pp.P-22-1 to P-22-6.
- Bhattacharya A. & Reddy S. (1994) Underground and surface coal mine fire detection in India's Jharia coal field using airborne thermal infrared data. *Asian-Pacific Remote Sensing Journal*, **7**, 59-73.
- Bhattacharya A., Reddy S., and Dangwal M. (1996) Coal mine fire inventory and monitoring in Jharia coal field, Bihar, India, Using thematic mapper thermal IR data. *Proceedings of the Eleventh Thematic Conference and Workshops on Applied Geologic Remote Sensing*, Las Vegas, USA, 27-29 February 1996.
- Banerjee S.C. (1982) A theoretical design to the determination of risk index of spontaneous fires in coal mines. *Journal of Mines, Metals and Fuels*, 399-406.
- Banerjee S.C. (1985) Spontaneous Combustion of Coal and Mine Fires. A. A. Balkema, Rotterdam, ISBN 90 6191 574 0.
- Banerjee S.C., Banerjee B.D. and Chakravorty R.N. (1970) Rate studies of aerial oxidation of coal at low temperature (30°C-170°C). *Fuel*, **49**, 324-331.
- Banerjee S.C., Nandy D.K., Banerjee, D.D. and Chakravorty R.N. (1972) Classification of coal with respect to their susceptibility to spontaneous combustion. *Transactions of the Mining and Metallurgical Institute of India*, **59**(2), 15-31.
- Barthelmy D. (1999a) Mineralogy Database –Apjohnite Mineral Data, [www: http://web.net/%/Edaba/Mineral/data/Apjohnite.html](http://web.net/%/Edaba/Mineral/data/Apjohnite.html).
- Barthelmy, D. (1999b) Mineralogy Database –Tschermitgite Mineral Data, [www: http://web.net/%/Edaba/Mineral/data/Tschermitgite.html](http://web.net/%/Edaba/Mineral/data/Tschermitgite.html).
- Bartolucci L.A., Chang M., Anuta P.E. and Graves M.R. (1988) Atmospheric effects on Landsat TM thermal IR data. *IEEE Transactions on Geoscience and Remote Sensing*, **26**, 171-175.
- Becker F. (1987) The impact of spectral emissivity on the measurement of land surface temperature from a satellite. *International Journal of Remote Sensing*, **8**, 1509-1522.
- Becker F. & Raffy M. (1987) Problems related to the determination of land surface parameters and fluxes over heterogeneous media from satellite data. *Advanced Space Research*, **7**(11), 45-57.
- Becker F. & Li Z.L. (1990a) Temperature-independent spectral indices in thermal infrared bands. *Remote Sensing of Environment*, **32**, 17-33.

- Becker F. & Li Z.L. (1990b) Towards a local split window method over land surfaces. *International Journal of Remote Sensing*, **11**, 369-393.
- Belward A.S., Kennedy P.J. and Gr,goire J.-M. (1994) The limitations and potentials of AVHRR GAC data for continental scale fire studies. *International Journal of Remote Sensing*, **15**, 2215-2234.
- Bhattacharya A., Reddy S. and Mukherjee T. K. (1991) Multi-tier remote sensing data analyses for coal fire mapping in Jharia coalfield of Bihar, India. *Proceedings of the 12th Asian Conference on Remote Sensing*. Singapore, 30 Oct. – 5 Nov. pp. P221-P226.
- Bhattacharya A., Reddy C.S.S. and Srivastav S.K. (1993) Remote sensing for active volcano monitoring in Barren Island, India. *Photogrammetric Engineering and Remote Sensing*, **59**, 1293-1297.
- Bhattacharya A. & Reddy C.S.S. (1994) Underground and surface coal mine fire detection in India's Jharia coalfield using airborne thermal infra-red data. *Asian Pacific Remote Sensing Journal*. **7**, 59-73.
- Bhattacharya A., Reddy C.S.S. and Manoj Dangwal (1996) Coal mine fire inventory and monitoring in Jharia coalfield, Bihar, India, Using thematic mapper thermal IR data. *Proceedings of the Eleventh Thematic Conference and Workshops on Applied Geologic Remote Sensing*, Las Vegas, USA, 27-29 February 1996.
- Bustin R.M. & Mathews W.H. (1982) In situ gasification of coal, a natural example: history, petrology, and mechanics of combustion. *Canadian Journal of Earth Sciences*. **19**, 514-523
- Bustin, R.M. & Mathews, W.H. (1985) In situ gasification of coal, a natural example: additional data on the Aldridge Creek coal fire, South-eastern British Columbia. *Canadian Journal of Earth Sciences*. **22**, 1858-1864.
- Castleman K.R. (1979) Digital Image processing. Prentice Hall, New Jersey.
- Cassells C.J.S. & van Gendroeren J.L. (1995) Thermal modelling of underground coal fires in northern China. Remote Sensing in Action, *Proceedings of the 21st Annual Conference of the Remote Sensing Society*, 11-14 September 1995, pp.544-551.
- Cassells C.J.S., van Genderen, J.L. and Zhang X.M. (1996) Detection and measuring underground coal fires by remote sensing. *Proceedings of the 8th Australian Remote Sensing Conference*, Canberra, March, 1996. Volume II, Thursday 28-3-96, pp.90-101.
- Chaiken R. F., Brennan R. J., Heisey B. S., Kim A. G., Malenka W. T., and Schimmel J. T. (1998) Problems in the Control of Anthracite Mine Fires: A Case Study of the Centralia Mine Fire. Report of Investigations 8799 of the United States Department of the Interior. Pittsburgh, USA.
- Chang C. & Chiang S. (2002) anomaly detection and classification for hyperspectral imagery. *IEEE transactions on geoscience and remote sensing*. **40**(6), 1315-1325.
- Charles E. (1987) Introduction to the physics and techniques of remote sensing, John Wiley & Sons, Inc.
- Chen Liding (1997) Subsidence assessment in the Ruqigou coalfield, Ningxia, China, Using a geomorphological approach. MSc thesis, International Institute for Aerospace Survey and Earth Sciences. Enschede.
- Chen W. (1992) Digital image processing application for coal fire remote sensing investigation, *Remote Sensing for Land & Resources*, **12**, 21-24 (in Chinese).

- Chuvienco E. & Martin M.P. (1994a) A simple method for fire growth mapping using AVHRR channel 3 data. *International Journal of Remote Sensing*, **15**, 3141-3146.
- Chuvienco E. & Martin M.P. (1994b) Global fire mapping and fire danger estimation using AVHRR images, *Photogrammetric Engineering & Remote Sensing*, **60**(5), 563-570.
- Chuvienco E. & Salas J. (1996) Mapping the spatial distribution of forest fire danger using GIS. *International Journal of Geographical Information Systems*, **10**, 333-345.
- Coll C., Caselles V. and Schmugge T.J. (1994) Estimation of land surface emissivity differences in the split-window channels of AVHRR. *Remote Sensing of Environment*, **48**, 127-134.
- Cooper D.I. & Asrar G. (1989) Evaluating atmospheric correction models for retrieving surface temperatures from the AVHRR over a tall grass prairie. *Remote Sensing of Environment*, **27**, 93-102.
- Cracknell A.P. & Hayes L.W.B. (1991) Introduction to Remote Sensing. Taylor & Francis. London. ISBN 0-85066-409-8.
- Cracknell A. P., & Mansor S.B. (1992) Detection of sub-surface coal fires using Landsat Thematic Mapper data. *International Archives of Photogrammetry and Remote Sensing*, **29**(B7), 750-753.
- Curran P.J. (1985) Principles of remote sensing. Longman Scientific & Technical. ISBN 0-582-30097-5.
- Daniel M. (1994) Chinese coal prospects to 2010. International Energy Agency, IEA on Coal Research, London.
- Dave J.V. & Bernstein R. (1982) Effect of terrain orientation and solar position on satellite-level luminance observations. *Remote Sensing of Environment*, **12**, 331-348.
- Deng W., Wan Y., and Zhao R. (2001) Detecting coal fires with a neural network to reduce the effect of solar radiation on Landsat Thematic Mapper thermal infrared images, *International Journal of Remote Sensing*, **22**, 933-944.
- De Boer, C.B., van Hoof, A.A.M., Zhang X.M., Kroonenberg, S.b., Dekkers M.J. (1997) Native iron in baked sediments due to spontaneous underground combustion of coal seams. Annual General Assembly of European Geophysical Society, 1997, 23-25, April Vienna Suppl. I to vol 15, C111.
- Desjardins R., Gray J. and Ferdinand B. (1990) Atmospheric corrections for remotely-sensed thermal data in a cool humid temperature zone. *International Journal of Remote Sensing*, **11**, 1369-1389.
- DLR-DFD (2003) Reception and project specific processing of remote sensing data for the support of current and future projects within the Chinese-German environmental research cooperation (Midterm report). FKZ: 03 399 79A. German Remote Sensing Data Center (DLR-DFD), Germany
- Dozier J., 1981, A method for satellite identification of surface temperature fields of subpixel resolution. *Remote Sensing of Environment*, **11**, 221-229.
- Driessen P.M. & Dudal R. (1991) The major soils of the world. Leuven
- Ellyett C.D. & Fleming A.W. (1974) Thermal infrared imagery of the Burning Mountain coal fire. *Remote Sensing of Environment*, **3**, 79-86.

- Eymard L. & Taconet O. (1995) The methods for inferring surface fluxes from satellite data and their use for atmosphere model validation. *International Journal of Remote Sensing*, **16**, 1907-1930.
- Feng F. (1990) Boundary identification for burnt coal seams in Xinmin spontaneous combustion district of Shenfu coal field, Shaanxi, *Proceeding of 11th Asian Conference on Remote Sensing*, No. 15-21, 1990, Guangzhou, China.
- Feng K.K., Chakravorty R.N. and Cochrane T.S. (1973) Spontaneous combustion - A coal mining hazard. *CIM Bulletin*, 66(738), 75-84.
- Fisher W., & Knuth W. K. JR (1968) Detection and delineation of subsurface coal fires by aerial infrared scanning. Geological Society America, Special Paper, 115, p. 67-68.
- Francis P.W. & de Silva S.L. (1989) Application of the Landsat Thematic Mapper to the identification of potentially active volcanoes in the Central Andes. *Remote Sensing of Environment*, **28**, 245-255.
- Gabriel A.K., Goldstein R.M. and Zebker H.A. (1989) Mapping small elevation changes over large areas: Differential radar interferometry. *Journal of Geophysical Research*, **94**(B7), 9183-9191.
- Gaikovich K.P. (1994) Simultaneous solution of emission transfer and thermal conductivity equations in the problems of atmosphere and subsurface radiothermometry. *IEEE Transactions on Geoscience and Remote Sensing*, **32**, 885-889.
- Gens R. & van Genderen J.L. (1996) SAR interferometry- issues, techniques, applications. *International Journal of Remote Sensing*, **17** (10), 1803-1835.
- Gijbels M.R. & Bruining J. (1982) Spontaneous ignition time of underground coal. *Erdöl und Kohle - Erdgas - Petrochemie vereinigt mit Brennstoff-Chemie*, **35**, 376-379.
- Glover L. (1998) Burning Beneath the Surface, *TRIBUNE-REVIEW*, May 3, 1998.
- Goetz A.F.H. & Rowan L.C. (1981) Geologic remote sensing. *Science*, **211**, 781-791.
- Greene G. W., Moxham R.M. (1968) Additional infrared surveys of coal mine fires in the anthracite and bituminous fields, Pennsylvania, U.S. Geological Survey, Interagency Report BM-4 April 1968 (Washington, D.C.: United States Department of Interior, Bureau of Mines).
- Greene G. W., Moxham R.M., and Harvey, A.H. (1969) Aerial infrared surveys and borehole temperature measurements of coal mine fires in Pennsylvania, *Proceedings of the 6th Symposium on Remote Sensing of Environment*, University of Michigan, 13-16 October (Ann Arbor, Michigan: Institute of Science and Technology, University of Michigan), pp.517-525
- Guan H. (1963) The Yaojie burnt rocks. *Proceedings of Shaanxi Young scientists Conference*, China. 212-226 (in Chinese).
- Guan H. (1984) The research of coal bed thermal IR radiation. *Proceedings of the Seminars on Remote Sensing for Geological Applications*. pp.535-547.
- Guan H. (1989) Applications of remote sensing techniques in coal geology. *Acta Geologica Sinica*, **2**, 253-269.
- Guan H., van Genderen J.L., and Schalke H. J. W.G. (1996) Study and survey on the geological hazards of coal fire in North China. *Abstracts 30th International Geological Congress*. vol 1, 458. Beijing, China, 4-14 August, 1996.

- Guan H., & van Genderen J. L. (1997) Report on environment monitoring of spontaneous combustion in the coal fields of North China (in Chinese). Aerophotogrammetry and Remote Sensing Bureau of China Coal, Xi'an, China, and International Institute for Aerospace Survey and Earth Sciences, Enschede, The Netherlands.
- Gupta R.K. & Badrinath K.V.S. (1993) Volcano monitoring using remote sensing data. *International Journal of Remote Sensing*, **14**, 2907-2918.
- Gupta R. P. (1991) Remote Sensing Geology, Springer-Verlag, Berlin.
- Gupta R. P., & Prakash A. (1998) Reflection aureoles associated with thermal anomalies due to subsurface mine fires in the Jharia Coalfield, India. *International Journal of Remote Sensing*, **19**, 2619-2622.
- Hamilton M. S. (2001) Not Burning Down the House [www : www.orangutan.com/coalfiresuppression.shtml](http://www.orangutan.com/coalfiresuppression.shtml).
- Harris A.J.L., Vaughan R.A. and Rothery D.A. (1995) Volcano detection and monitoring using AVHRR data: the Krafla eruption, 1984. *International Journal of Remote Sensing*, **16**, 1001-1020.
- Hixson M., Schulz D., Nancy F. and Akiyama T. (1980) Evaluation of several schemes for classification of remotely sensed data. *Photogrammetric Engineering and Remote Sensing*, **46**, 1547-1553.
- Holben B.N. & Justice C.O. (1981) an examination of spectral band ratioing to reduce the topographic effect on remotely sensed data. *International Journal of Remote Sensing*, **2**, 115.
- Hook S.J., Gabell A.R., Green A.A. and Kealy P.S. (1992) A comparison of techniques for extracting emissivity information from thermal infrared data for geologic studies. *Remote Sensing of Environment*, **42**, 123-135.
- Huang Y., Huang H., Chen W., and Li Y. (1991) Remote sensing approaches for underground coal fire detection. *Proceedings of the International Conference on Reducing of Geological Hazards*, Beijing, pp.634-641.
- Hunt G. R. & Salisbury J. W. (1970) Visible and near infrared spectra of minerals and rocks: I Silicate minerals. *Modern Geology*, **1**, 283-300.
- Hunt, G. R., & Salisbury J. W. (1971a) Visible and near infrared spectra of minerals and rocks: II Carbonates. *Modern Geology*, **2**, 23-30.
- Hunt G. R., Salisbury J. W., Lenhoff C.J. (1971b) Visible and near infrared spectra of minerals and rocks: III Oxides and Hydroxides. *Modern Geology*, **2**, 195-205.
- Hunt G. R., Salisbury J. W., Lenhoff C.J. (1971c) Visible and near infrared spectra of minerals and rocks: IV Sulphides and Sulphates. *Modern Geology*, **3**, 1-14.
- Hunt G. R. & Salisbury J. W. (1973a) Visible and near infrared spectra of minerals and rocks: VI Additional Silicates. *Modern Geology*, **4**, 85-106.
- Hunt G. R., Salisbury J. W., Lenhoff C.J. (1973b) Visible and near infrared spectra of minerals and rocks: VII Acidic Igneous Rocks. *Modern Geology*, **4**, 217-224.
- Hunt G. R., Salisbury J. W., Lenhoff C.J. (1976) Visible and near infrared spectra of minerals and rocks: XI Sedimentary Rocks. *Modern Geology*, **5**, 211-217.
- Jia Y. (2002) Personal interviews during the fieldwork campaigns in September 2002 (Y. Jia is the chief engineer of the coal fire fighting team Wuda).

- Justice C.O., Wharton S.W. and Holben B.N. (1981) Application of digital terrain data to quantify and reduce the topographic effect on Landsat data. *International Journal of Remote Sensing*, **2**, 213-230.
- Kahle A.B. (1980) Surface thermal properties. Remote Sensing in Geology, edited by B.S. Siegal and A.R.Gillespie, Wiley, New York, pp.257-273.
- Kahle A.B., Palluconi F.D., Hook S.J., Realmuto V.J. and Bothwell G. (1996) The advanced spaceborne thermal emission and reflectance radiometer (ASTER). *International Journal of Imaging Systems and Technology*, **3**, 144-156.
- Kang G. (1991) Study on the application of techniques of aerial remote sensing to Shenfu coal field of Jurassic system, *Proceeding of the Eighth Conference on Geologic Remote Sensing*, Denver, Colorado, USA, April 29-May 2, 1991, pp.719-727.
- Kaufman, Y.Z., Setzer A., Ward D., Taner D., Holban B.N., Menzel P., Pereira M.C., and Rasmussen R. (1992) Biomass burning airborne and spaceborne experiment in the amazons (base-a). *Journal of Geophysical Research*, **97**:14581-14599.
- Kawata Y., Ueno S. and Kusaka T. (1988) Radiometric corrections for atmospheric and topographic effects on Landsat MSS images. *International Journal of Remote Sensing*, **9**, 729-748.
- Kennedy P.J., Belward A.S., Gregoire J.M. (1994) An improved approach to fire monitoring in west Africa using AVHRR data. *International Journal of Remote Sensing*, **15**, 2235-2255.
- Knuth W.M., Fisher W.Jr. and Stingelin R.W. (1968) Detection, delineation and monitoring of subsurface coal fires by aerial infrared scanning. Geographer HRB-Singer, Inc., a subsidiary of the Singer Company, state Collee, Pennsylvania, pp. 877-881.
- Kuenzer C., Zhang J., Tetzlaff A., Voigt S., van Dijk P., Wagner W., Mehl H. (2003) Uncontrolled coal fires and their environmental impacts: Investigating two arid mining regions in north-central China. *Applied Geography*. Submitted.
- Kuenzer C., Zhang J., Voigt S. (2003) Set up of a spectral data base for unmixing approaches in mining environments in North-central China: Demarcating coal fire risk areas. Proceedings of the 3rd EARSEL workshop on imaging spectroscopy, Oberpfaffenhofen.
- Landsat Project Science Office (1998) Landsat 7 Science Data Users Handbook, Chapter 11-Data Products, http://ltpwww.gsfc.nasa.gov/LAS/handbook/handbook_toc.html.
- Lee Y. J., Tower E., Brodatsch H. and Findings S. (1977) Computer assisted forest land classification by means of several classification methods on the CCRS Image-100. *Proceedings of the 4th Canadian Symposium on Remote Sensing*. Canadian Aeronautical and Space Institute, Ottawa, pp.37-46.
- Li D. X. (1985) Applied study of airborne remote sensing in Taiyuan coalfield, China, Internal Report (Xi'an, China: Remote sensing centre of ministry of coal industry), pp3-10 (in Chinses).
- Li Z.R. & McDonnell M.J. (1988) Atmospheric correction of thermal infrared images. *International Journal of Remote Sensing*, **9**, 107-121.
- Lillesand T. M. & Kiefer R. W. (1979) Remote Sensing and Image Interpretation. Wiley, New York.

- Liu J. & Moore, J.M. (1997) Simulated higher spatial resolution Land sat thermal image, *Proceedings of the Twelfth International Conference and workshop on Applied Geologic Remote Sensing*, Denver, Colorado, 17-19, November 1997, vol I, pp182-189.
- Livingood M., Winiacities J., Stein J. (1999) Centralia Mine Fire Analysis: Presence of sulfur-bearing mineral deposits at thermal vents. ESL201- fundamental techniques in geology. www: www.cdc.gov/niosh/mining/comp2000/sfs.html
- Lowenstern J. (1999) USGS-Alid Volcanic Center in Eritrea, NW Africa. www: wrgis.wr.usgs.gov/lowenstern/alid/alidphotos.html.
- Lopez S., Gonz lez F., Llop R. and Cuevas J.M. (1991) An evaluation of the utility of NOAA AVHRR imagery for monitoring forest fire risk in Spain. *International Journal of Remote Sensing*, **12**, 1841-1851.
- Ma J. (2002). Personal interviews during the fieldwork campaigns in September 2002. (J. Ma is a coal fire fighting expert in Beijing Remote Sensing Center).
- Mansor S.B., Cracknell A.P., Shilin B.V. and Gornyi V.I. (1994) Monitoring of underground coal fires using thermal infrared data. *International Journal of Remote Sensing*, **15**, 1675-1685.
- Markham B. L., & Barker J. L. (1986) Landsat MSS and TM post calibration dynamic ranges, exoatmospheric reflectances and at-satellite temperatures. In EOSAT Landsat Technical Notes 1 August 1986 (Lanham, Maryland : Earth Observation Satellite Co), pp3-8.
- Matson M. & Dozier J. (1981) Identification of sub-resolution high temperature sources using a thermal IR sensor, *Photogrammetric Engineering and Remote Sensing*, **47**. 1311-1318.
- Mitchell T. L. (1839) Three Expeditions into the Interior of Eastern Australia with Descriptions of the Recently explored Region of Australia Felix and the Present Colony of N.S.W., vol.1 Eastern Australia, T. and W. Boone, London, 1938.
- Moxham R.M. & Greene G.W. (1967) Infrared surveys of coal mine fires in the anthracite and bituminous fields, Pennsylvania. U.S. Geological Survey Inter-Agency Report BM-2, U.S. Bureau of Mines, July, 1967
- Mukherjee T. K., Bandyopadhyay T.K. and Pande S.K. (1991) Detection and delineation of depth of subsurface coalmine fires based on an airborne multispectral scanner survey in a part of the Jharia Coalfield, India. *Photogrammetric Engineering and Remote Sensing*, **57**, 1203-1207.
- Nerry F., Labeled J. and Stoll M.P. (1990) Spectral properties of land surfaces in the thermal infrared 1. Laboratory measurements of absolute spectral emissivity signatures. *Journal of Geophysical Research*, **95**, 7027-7044.
- Oetl H., Briess K., Lorenz E., Oertel D., Shrbek W., Walter I., and Zhukov B. (2003) The disaster, 'fires', its detection and means to improve information. *Space Technology*, **23**(4), 249-256
- Oppenheimer C., Rothery D.A., Pieri D.C., Abrams M.J. and Carrere V. (1993) Analysis of airborne visible/infrared spectrometer (AVIRIS) data of volcanic hot spots. *International Journal of Remote Sensing*, **14**, 2919-2934.
- Ouaidrari H., Imbernon J. and Dedieu G. (1994) Use of a meteorology model to correct atmospheric effects in NOAA-AVHRR data. *International Journal of Remote Sensing*, **15**, 2257-2271.

- Pereira Jr. A.C. & Setzer A.W. (1996) Comparison of fire detection in Savannas using AVHRR's channel 3 and TM images. *International Journal of Remote Sensing*, **17**, 1925-1937.
- Pereira M.C. & Setzer A.W. (1993) Spectral characteristics of deforestation fires in NOAA/AVHRR images. *International Journal of Remote Sensing*, **14**, 583-597.
- Pieri D.C., Glaze L.S. and Abrams M.J. (1990) Thermal radiance observations of an active lava flow during the June 1984 eruption of Mount Etna. *Geology*, **18**, 1018-1022.
- Prakash A., Saraf A.K., Gupta R.P., Dutta M., Sundaram R.M. (1995a) Surface thermal anomalies with underground fires in Jhahra coal mine, India. *International Journal of Remote Sensing*, **16**, 2105-2109.
- Prakash A., Sastry R.G.S., Gupta R.P., Saraf, A.K. (1995b) Estimating the depth of buried hot feature from thermal IR remote sensing data: a conceptual approach. *International Journal of Remote Sensing*, **16**, 2503-2510.
- Prakash A., Gupta R.P. and Saraf A.K. (1997) A landsat TM based comparative study of surface and subsurface fires in the Jharia Coalfield, India. *International Journal of Remote Sensing*, **18**, 2463-2469.
- Prakash A., Gens R. and Vekerdy Z. (1999) Monitoring coal fires using multi-temporal night-time thermal images in a coalfield in North-west China. *International Journal of Remote Sensing*, **20**, 2883-2888.
- Prakash A. & Gupta R.P. (1999) Surface fires in Jharia Coalfield, India - their distribution and estimation of area and temperature from TM data. *International Journal of Remote Sensing*, **20**, 1935-1946.
- Prakash A., Fielding E.J., Gen, R., van Genderen J.L. and Evans D.L. (2001) Data fusion for investigating land subsidence and coalfire hazards in a coal mining area. *International Journal of Remote Sensing*, **22**, 921-932.
- Rabchevsky G.A. (1972) Determination from available satellite and aircraft imagery of the applicability of remote sensing techniques to the detection of fires burning in abandoned coal mines and unmined coal deposits located in North Central Wyoming and Southern Montana. U.S. Department of Interior, Bureau of Mines, Prepared by Allied Research Associates Inc., Contract No. SO 211087, Final Report No. 8G86-F.
- Rathore C.S. & Wright R. (1993) Monitoring environmental impacts of surface coal mining. *International Journal of Remote Sensing*, **14**, 1021-1042.
- Reddy C.S.S., Srivastav S.K. and Bhattacharya A. (1993) Application of thematic mapper short wavelength infrared data for the detection and monitoring of high temperature related geo-environmental features. *International Journal of Remote Sensing*, **14**, 3125-3132.
- Reddy C.S.S. & Bhattacharya A., 1995, Use of GPS for ground truth data collection and its integration with RS and GIS: A case study with reference to the mine fire mapping in Jharia, Bihar state, India. *Asian-Pacific Remote Sensing Journal*, **7**, 155-158.
- Reed I.S. & Yu X. (1990) adaptive multiple-bad CFAR detection of an optical pattern with unknown spectral distribution. *IEEE trans. Acoust., Speech, Signal Processing*, vol. 38, pp 1760-1770, Oct. 1990
- Rosema A., van Genderen J.L., and Schalke H.J.W.G. (1993) Environmental monitoring of coal fires in north China. Project Identification Mission Report, BCRS 93-29, ISBN 90 5411 1054, 24 p.

- Rosema A., Guan H., Vekerdy Z., Katen Z.A., and Prakash A. (1999) Manual of coal fire detection and monitoring. Utrecht.
- Rosenfeld A. & Kak A.C. (1976) Digital picture precessing. Academic press, New York.
- Rothery D.A., Francis P.W. and Wood C.A. (1988) Volcano monitoring using short wavelength infrared data from satellites. *Journal of Geophysical Research*, **93**, 7993-8008.
- Rothery D.A. & Francis P.W. (1990) Short wavelength infrared images for volcano monitoring. *International Journal of Remote Sensing*, **10**, 1665-1667.
- Sabins F.F. (1996) Remote Sensing: Principles and Interpretation, Third Edition. Freeman, New York.
- Salisbury J.W. & D'Aria D.M. (1992) Emissivity of terrestrial materials in the 8-14um atmospheric window. *Remote Sensing of Environment*, **42**, 83-106.
- Saraf A.K., Gupta R.P., and Anishkumar (1992) Remote sensing technique in underground fire detection in coal mines of Jharia. *Proceedings of ICORG-92 on Remote Sensing Application & GIS: Recent Trends*.
- Saraf A.K., Prakash A., Sengupta S., and Gupta P. (1995) Landsat-TM data for estimating ground temperature and depth of subsurface coal fire in the Jharia coal field, India. *International Journal of Remote Sensing*, **16**, 2111-2124.
- Schmal D. (1987) A model for the spontaneous heating of stored coal. Ph.D thesis, Technology University of Delft, Delft, The Netherlands.
- Schneider W. (1996) The coal-bearing Jurassic at the southern margin of the Junggar basin, Xinjiang. *Geowissenschaften* **14**: 285-287.
- Singh S.M., (1994), Effect of surface wind speed and sensor view zenith angle dependence of emissivity on SST retrieval from thermal infrared data: ATSR. *International Journal of Remote Sensing*, **15**, 2615-2625.
- Singh S.M. (1984) Removal of atmospheric effects on a pixel by pixel basis from the thermal infrared data from instruments on satellite. The advanced very high resolution radiometer (AVHRR). *International Journal of Remote Sensing*, **5**, 161-183.
- Sinha P.R. (1989) Mine fires in Indian coal fields. *Energy*, **11**, 1147-1154.
- Slavecki R. J. (1964) Detection and location of subsurface coal fires. *Proceedings of the Third Symposium on Remote Sensing of Environment*. 14-16 October 1964, Institute of Science and Technology, University of Michigan, Michigan (Ann Arbor: ERIM). PP537-547.
- Sobrino J.A., Coll C. and Caselles V. (1991) Atmospheric correction for land surface temperatures using NOAA-11 AVHRR channels 4 and 5. *Remote Sensing of Environment*, **38**, 19-34.
- Sun Y. (2002) Personal interviews during the fieldwork campaigns in September 2002 (Y. Sun is an engineer of the coal fire fighting team Wuda).
- Tetzlaff A. (2004) Fire radiative energy for quantitative study of coal fires: derivation from ETM imagery and comparison to BIRD experimental satellite data. Submitted to *International Journal of Remote Sensing*.
- URL1 : <http://features.learningkingdom.com/fact/archive/1999/04/13.html>.
- van der Meer F. (1995) Imaging spectrometry and the Ronda peridotites. Ph.D thesis, Wageningen University, the Netherlands.

- van Genderen J.L. & Guan H. (1997) Environmental monitoring of spontaneous combustion in the North China coalfields. Final report to European Commission under contract No. C11*-CT93-0008 (DG-HSMV).
- van Genderen J.L., Cassells C. J. S. and Zhang X., (1996) The synergistic use of remotely sensed data for the detection of underground fires. *International Archives of Photogrammetry and Remote Sensing*, Vienna, 9-19 July 1996, vol.XXXI, Part B7, Volume 1 of 3, pp. 722-727 (RICS books; Coventry, UK), ISSN 0256-1840.
- Vekerdy Z. & van Genderen J.L. (1999) CoalMan-information system for the monitoring of subsurface coal fires and the management of fire fighting in coal mining areas, *Proceedings of the Geoinformatics: Beyond 2000*, 9-11 March,1999, IIRS, India, pp:179-184.
- Vekerdy Z., Prakash A., and Gens, R. (1999) Data integration for the study and visualisation of subsurface coal fires, *Proceedings of the 13th international Conference on applied Remote Sensing*, 1-3 March,1999. Vancouver, Canada, pp:II-150-151.
- Vidal A. (1991) Atmospheric and emissivity correction of land surface temperature measured from satellite using ground measurements or satellite data. *International Journal of Remote Sensing*, **12**, 2449-2460.
- Voigt S., Tetzlaff A., Zhang J., Kuenzer C., Zhukov B., Strunz G., Oertel D., Roth A., van Dijk P., Mehl H. (2003) Integrating Satellite Remote Sensing Techniques for Detection and Analysis of Uncontrolled Coal Seam Fires in North China. *International Journal of Coal Geology*. In print.
- Wan Y. & Zhang X. (1996a) Using a DTM to reduce the effect of solar radiance on Landsat TM thermal IR images and detect coal fires. *Asian Pacific Remote Sensing and GIS Journal*, **8**, 65-72.
- Wan Y. & Zhang X. (1996b) Using DTM to improve the accuracy of detecting coal fires with thermal images, *Remote Sensing of the Environment China*, **11**(4), 248-254 (in Chinese).
- Wang, C., (2002) Detection of coal fires in Xinjiang (China) using remote sensing techniques. Master thesis. International Institute for Geo-Information Science and Earth Observation (ITC). Enschede.
- Weischet (1988) Einführung in die Allgemeine Klimatologie. Physikalische und meteorologische Grundlagen. 4th edition, Stuttgart
- Wu, W. & Zhang, W. (2003) Present land use and cover patterns and their development potential in North Ningxia, China. *Journal of Geographical Sciences*, **13**(1), 54-62
- Wukelic G.E., Gibbons D.E., Martucci L.M. and Foote H.P. (1989) Radiometric calibration of Landsat thematic mapper thermal band. *Remote Sensing of Environment*, **28**, 339-347.
- Xie Y. (2001) Einfluss der Weidewirtschaft auf die Vegetation und die ökologischen Bedingungen der Trockensteppe in Ningxia, China. Frankfurt
- Yang H. (1995) Detection of areas of spontaneous combustion of coal by using airborne and TM data in Xinjian, China. MSc thesis, International Institute for Aerospace Survey and Earth Sciences.
- Yang H., Koopmas B.N., Mao Y.B., Kang G.F. (1996) Detectability of coal fire areas from the airborne thermal data and Landsat TM data in Xinjiang, China. *30th International Geological Congress Abstracts*, 4-14 August, 1996, Beijing, China.

- Zhang J. (1996) SWIR spectra of rocks in areas affected by coal fires, Xinjiang Autonomous Region, P.R. of China. MSc thesis, International Institute for Aerospace Survey and Earth Sciences. Enschede.
- Zhang J., van Dijk P., and Yang H. (1996) Shortwave infrared spectra of rocks in areas affected by coal fires, Xinjiang, China. *30th International Geological Congress Abstracts*, 4-14 August, 1996, Beijing, China.
- Zhang J., Wagner W., Prakash A., Mehl H., and Voigt S. (2003) Detecting coal fires using remote sensing techniques. *International Journal of Remote Sensing*, In print.
- Zhang R. (2003) Personal Interviews during the fieldwork campaign in September 2003. (R. Zhang is the chief engineer of the Wuda mine).
- Zhang X., Koopmans B.N., and Wan Y. (1995) Detection of spontaneous combustion of coal in northern China, using thermal remote sensing data. *Proceedings of International Space Congress*, Bremen, Germany, May 23-25th, 1995, pp2-10.
- Zhang X., & Kroonenberg, S.B. (1996) Pleistocene coal fires in Xinjiang, northwest China. *Abstracts 30th International Geological Congress*, pp.457.
- Zhang X., van Genderen J. L. and Kroonenberg S. B. (1997a) A method to evaluate the capability of landsat-5 TM band 6 data for sub-pixel coal fire detection. *International Journal of Remote Sensing*, **18**, 3279-3288.
- Zhang X., Cassells C., and van Genderen, J.L. (1997b) Mapping underground coal fires using Remote Sensing and GIS techniques, *10th International Congress of the International Society for mine Surveying*, Fremantle, Western Australia, 2-6 November 1997.
- Zhang X. (1998) Coal fires in Northwest of China, Detection, monitoring, and prediction using remote sensing data. Ph.D thesis, ISBN 90-6164-144-6. ITC.
- Zhang X., Cassells C., and van Genderen J. L. (1998) Multi-sensor data fusion for the detection of underground coal fires, *Geologie & Mijnbouw*, **77**, 117-127.
- Zhang X. (1997) Regional geological mapping by using remote sensing and sedimentary characteristics of the Ruqigou basin, Ningxia, China. MSc. thesis at ITC Enschede.
- Zhang Y., & Tang X.(1994) Coal petrology application for liability of coal to spontaneous combustion, *Coal Geology and Exploration*, **22**, 21-24 (in Chinese).

Appendix 6.1: Ground Temperature Measurements of Coal Fire Experiment in DLR, Oberpfaffenhofen. 23 and 24 May 2002. Page: 1/4

Time	WS&D	OB	AT	FCS	FCU	FRS	FRU	B1	B2	B3	B4
10:58-11:15		Z	24	880		313					
12:00-12:15		Z	29.4								
12:45-12:52	L&N	Z	25.7			309					
13:50-13:55		Z	24.9	957		500					
14:20		T		920		600	820	23.6	29.9	22.6	25.3
14:28		T	30	994		650		23.4	26.5	24.1	22.8
14:38	L	T	26.3	937		680	700	23.7	25	22.8	28.5
14:47	M	T	26.3			49(NF)	690	23.6	27.8	24.9	22.9
14:50		Z									
14:59		T	28.8			33.8(NF)		23.1	24.2	22	24.2
15:05	M	T	24.4	1050		790	630	23.8	24	22.2	22.2
15:12	L	T	25.1	1050		600-850	600-650	22.6	24.5	23.4	24.7
16:36	M&W	T	25	1080		600-700	600-700				
17:50-17:59	L&N	Z	24.6	960		300-400	550				
18:45-18:55	L&N	Z	26	1005		670-780					
19:00		T					Sand Cover				
19:15		T	21		842		18.5				
19:50	0	T	19.5		1000	750	17.6				
20:50-20:58		T	16.9		1070	800-900	17.5				
21:45	0	T	14.5		890	360	15.7				
22:46		T	14.4		900	600-700	14.3				
23:45		T			870	600	14.3				
0:45		T	15		970	600-700	16.5				
1:45	L	T	15.7		950	400	16.3				
2:45	L	T	15.7			500	16.1				
3:45	M&N	Z	14.9		850	600	19.8				
4:45	M&W	T	15.5		1200+	17.8					
5:42	L	T	15.3			700-900	37.5	14.6	13.9	14.2	13.6
5:51		T	15.5				37.6	13.9	14.9	14.2	14.1
6:01	L	T	15.2			45(NF)	400(hole)	14.3	14	13.9	14.7
6:08	L	T	15.6			700-900	600(hole)	15.3	14.6	14	15
6:16	L	T	15.2			700		14.6	14.6	13.9	15.6
6:24	L	T	15.3			650-900		14	14.5	13.6	14.4
7:46	L	T	17.2			700-900	35	15.3	17	16	16.2
8:04	0	T	17.8			750-900	35	15.3	17.7	16	17
8:11	L	T	17.2			98(NF)	16.3	16.5	16.2	15.7	17.1
8:19	L	T	17.5			650-800	38	17.2	17.3	16.8	17.3
8:25	0	T	17.2			700-900	35	16.5	17.2	16.5	16.8
8:39	L	T	17.3			700-900	166	16.7	14.6	16.4	16.9
9:04	L&N	Z	17.4			600					
10:00-10:08	0	Z	18.2			600					
10:58-11:07	M&N	Z	19.6			550					
12:05	L&N	Z	19.8			500-600					
13:00-13:10	H&N	Z	20.8			860					

Notes: 1. WS&D: Wind speed (0, Low, Middle and High) and direction (North, East, South, and West). 2. OB: Observer (Anke Tetzlaff, Jianzhong Zhang). 3. AT: Air temperature.

Appendix 6.1: Ground Temperature Measurements of Coal Fire Experiment in DLR, Oberpfaffenhofen. 23 and 24 May 2002. Page: 2/4

Time	SC11	SC21	SC31	SC41	SC51	SC12	SC22	SC32	SC42	SC52	SC13	SC23	SC43	SC53
10:58-11:15	26	28	25	28	25	29	30	31	27	25	26	30	36	32
12:00-12:15	24.8	24	23	18.6	22.8	24	22.6	24.4	20.1	23	25.2	25	25	23
12:45-12:52	22.4	21	23.1	25.8	22.9	22.8	22.9	26.7	23	23	24.6	29.7	24.8	23.4
13:50-13:55	24.7	21.9	21.4	24.4	22.9	27.4	24.5	24.8	22.4	23.8	23	29.3	23.4	23.8
14:20														
14:28														
14:38														
14:47														
14:50	25.7	24.4	24.8	25	25.5	26.4	25.6				25.5	27.7		
14:59														
15:05														
15:12														
16:36	21.1	20.7	21.3	20.7	20.3	23	22.8	22.2	21.7	20.8	22.5	28.4	24.1	21.9
17:50-17:59	18.9	18.7	20.4	18.6	18.8	21	19.7	23.1	20	18.5	19.1	25.5	22.7	19.9
18:45-18:55	17.3	16.9	17.8	16.2	22	19.4	18.5	21	17.6	16.5	18.5	30	21.9	17
19:00														
19:15														
19:50	15.6	16	16.4	16.9	16.1	15.6	16.8	20.4	16.6	16.2	16.2	22.7	16.9	16.2
20:50-20:58	14.6	14.9	15.4	15.5	15.4	14	16.2	17.7	15.5	15	14.9	20.4	15.4	15.3
21:45	11.9	12.1	12	12.8	12.5	11.6	13.6	14.5	13.3	12.6	12.3	16.1	16.1	12.3
22:46	11.1	11.4	11.7	12.2	10.8	10.4	12.8	13	12.7	11.3	11.4	14	14.5	11.4
23:45	12.8	12.5	12.5	12.6	11.7	11.3	13.1	15.1	12.8	12	12.2	17.3	15.1	12
0:45	12.1	12.1	12.8	13	11.7	12.4	13.4	12.9	12.9	12.1	13	14.6	16	12.8
1:45	12.9	12.6	12.1	12.6	11.9	12.4	13.2	13.7	13.3	12.3	12.9	15.8	13.9	12.1
2:45	12.1	11.7	12.5	12.4	12.2	12	13.1	15.7	13.1	12.3	12.4	14.4	16.7	13.4
3:45	13.1	12.9	13.3	12.5	12.2	12.6	13.6	14.1	12.8	12.4	13.4	17	16.2	13.5
4:45	12.2	12.5	12.7	12.7	12.6	13.3	14.4	13.5	13.2	13.1	13.7	16.3	17.7	13.4
5:42														
5:51														
6:01														
6:08														
6:16														
6:24														
7:46														
8:04														
8:11														
8:19														
8:25														
8:39														
9:04	16	15.8	15.8	15.7	15.8	15.9	16.5	17.2	15.7	15.6	16.3	19.3	16.7	15.8
10:00-10:08	16.1	16	16	15.8	15.8	16.7	16.5	17.1	15.8	16	16.2	18.1	16	16
10:58-11:07	18.9	18.3	18.3	17.9	18.6	20.2	18.8	19.9	18	17.8	18.6	22.8	18.8	18.2
12:05	17.2	16.3	16.2	16.7	16.3	17.4	18	17.7	16.8	16.3	17.9	20.5	16.5	16.4
13:00-13:10	21.6	18.1	17.8	18.3	18.2	20.5	18.3	20.4	17.8	18.9	20.1	23.6	19	17.6

4. FCS: Contact temperature for simulated surface coal fire. 5. FCU : Contact temperature for simulated underground coal fire. 6. FRS : Surface radiant temperature for simulated surface coal fire (NF: No Fire). 7. FRU : Surface radiant temperature for simulated underground coal fire.

Appendix 6.1: Ground Temperature Measurements of Coal Fire Experiment in DLR, Oberpfaffenhofen. 23 and 24 May 2002. Page: 3/4

Time	SC14	SC24	SC34	SC44	SC54	SC15	SC25	SC35	SC45	SC55	HG1	HG2	HG3	HG4	HG5
10:58	26	27	30	28	26	25	25	26	27	30					
12:00	24.7	27	28.2	24	23.2	25.2	26.6	24	24	21.1					
12:45	23.6	23.3	25	22.9	23.4	23.2	22.3	23.4	23.1	23.6					
13:50	23.6	23.3	25.2	27	26	23.3	22.7	22.6	22.5	23					
14:20															
14:28															
14:38															
14:47															
14:50	25.3	26.8				25	25		27.1						
14:59															25
15:05															
15:12															26
16:36	21.5	22.4	25	21.7	19.9	22.1	22.1	23.4	21	21.2					
17:50	21.1	25.9	21.1	19.3	19	21.6	20.5	20.6	19	18	22.6	21.8	21.9	20	
18:45	18.1	20.9	21.2	17.7	18.7	18.4	17.3	19.4	16.6	16.3	19.5	19.6	18.7	18.4	
19:00															
19:15															
19:50	15.1	16.9	19.1	16.6	15.3	15.2	15.5	16.8	15.7	15.5	17.8	18.1	17.2	16.8	
20:50	14.1	15.2	18.4	15.7	14.4	13.7	15.1	16.2	15.5	14.5	14.6	15.4	14.1	14.2	
21:45	11.2	12.6	14.9	13.1	12	11.3	12	13.6	13.3	12.7	12.2	12	13	13	
22:46	10.5	11.8	14.9	11.8	10.7	10.5	10.7	12.7	12.2	11.5	10.8	10.3	11.3	11.7	
23:45	11.5	13.1	15.4	12.9	11	11.4	11.2	11.9	11.1	12.1	12	12.2	11.8	12	
0:45	12.3	12.9	14.5	12.8	12	11.8	12.7	12.8	12.2	12.5	12	12.5	12.5	13	
1:45	12.6	12.8	14.9	13.6	12.6	11.8	12.5	13.5	12.6	12.5	12.3	12.1	12.6	12.3	
2:45	12.9	13.3	15.2	13.2	12.5	12.8	12.8	13.6	13	13.1	12.5	12.6	13.1	13.2	
3:45	13.4	13.9	15	13.4	12.5	12.9	12.5	12.5	12.7	12.5	13.4	12.7	13.6	13.2	
4:45	12.9	15.5	15.6	12.7	13.3	12.6	13.1	12.6	12.9	13.6	13.6	13.4	14	13	
5:42															13.8
5:51															13.8
6:01															14.1
6:08															14
6:16															13.6
6:24															
7:46															16.6
8:04															16.3
8:11															15.6
8:19															16.2
8:25															16
8:39															15.6
9:04	16	16.8	17.8	16.3	15.9	16	15.6	15.7	15.8	15.5	16.2	16.1	15.6	16	
10:00	16.2	16.7	17	16	16.3	16.2	16.1	16.1	15.7	15.9	17.1	17.1	17.3	17.1	
10:58	18.7	19.2	19.2	18	18.2	18.7	19.1	18.2	18	17.8	18.7	19.7	19.5	18.5	
12:05	17.9	18.2	18.4	16.4	16.3	16.8	17.3	16.7	16.7	16.2	16.9	17.1	16.7	17.4	
13:00	21.1	21.2	20.1	17.6	18	18.7	20.7	18.2	17.9	17.9	19	19.7	19.2	19.8	

8. B1: located between SC31 and SC 32. 9. B2: located between SC13 and SC 23. 10. B3: located between SC43 and SC 53. 11. B4: located between SC34 and SC 35. 12. SC11-FRUN: measuring spots. See their locations in Figure 6.1.

Appendix 6.1: Ground Temperature Measurements of Coal Fire Experiment in DLR, Oberpfaffenhofen. 23 and 24 May 2002. Page: 4/4

Time	HG6	LG1	LG2	LG3	LG4	LG5	LG6	LG7	LG8	LG9	DG	FRUS	FRUE	FRUW	FRUN
10:58		24													
12:00															
12:45			30												
13:50															
14:20						29.5	28.6	30.1		37.5	34.3				
14:28						25.6	22.5	31	27.5	35.5	39.6				
14:38															
14:47								27.9	42.4	35.9					
14:50		32			30.5										
14:59						29.2	34				42				
15:05															
15:12						27.1	33	32.3	27.5	29.9	44.4				
16:36		27.6	26.1	27.8	24										
17:50		22	19.6	22	24.8										
18:45		25.1	19	22.2	21.6						28				
19:00															
19:15												32	43.5	22.8	19.3
19:50		19.3	18.5	19.2	17.3					17.7	23.6	51	21.7	20.5	
20:05		16.7	16.7	15.6	14.8					13.6	49	51.5	20	20.6	
21:45		13.5	14.2	14.3	12.4					10.8	18.2	38	17	20.1	
22:46		12	12.8	13.6	12.7					10.2	18.3	28	16.2	22.8	
23:45		12.3	14.2	13.6	12.8					12.5	20.3	25	17.4	21.5	
0:45		13	12.7	13.4	13.4						21.3	30.9	18	22	
1:45		13.1	13.3	13.7	13.6					12.4	20.6	32.3	20.2	27.3	
2:45		13.1	13.5	13.4	13.9					12.5	18.4	31.8	17.1	30	
3:45		13.2	13.2	13.5	13.6					12.8	18	collaps ed	17.6	33.9	
4:45		14	14.6	14.1	14.3					14	19		18.4		
5:42	13.2					15.4	14.6	14.4	15	14.8	13.2				
5:51	14.1					14.7	15.1	14.8		15.2	13.8				
6:01	13.8					14.8	15	15.8	15.5	15.5	13.6				
6:08	13.7					15.3	15.6	14	14.3	14.8	14.1				
6:16	13.2					14.8	15.4	14.5	15.3	14.8	13.6				
6:24						15.1	15.7	14.9	14.8	15	13.9				
7:46	15.7					16.2	17.2	16.9	16.8	17.7	17				
8:04	16.1					17	17.1	17	16.8	17.1	17				
8:11	16.1					17.2	17.4	17	17	17.3	17.8				
8:19	15.8					16.7	17.6	17.2	16.6	17	17.6				
8:25	16.4					17.4	16.9	17.2	17.1	17.8	17.5				
8:39	15.5					17	17	16.2	17.5		17.6				
9:04		16.1	16.5	16	16.3						16.7				
10:00		18	17.1	18.2	17						19.8				
10:58		18.9	18.4	22.8	22.7						24.5				
12:05		17.5	18.9	17.9	17.2						20.2				
13:00		20.4	19.4	21.6	19.4						28.4				

Appendix 6.2: Surface Temperature Measurements for a Sand Dune in Wuda Coal Mine Area, Inner Mongolia, China. 23rd September 2002

StartT	6:36	7:03	8:02	9:02	10:02	10:33	11:03	12:05	13:05	14:06	15:23	16:03	17:05	18:04	19:03
W1	7.8	8.6	9.5	16	23.2	30	32.9	35.1	38.5	40.1	36.9	36	28.1	20	15.3
W2	8.2	7.2	9.8	12.9	20.5	30.2	32.4	36.2	42.2	42.6	43.4	42.9	29.8	21.1	15.3
W3	6.6	8.8	10.5	13.3	16.8	21.6	24.5	31.5	36.5	42.5	42.8	40.7	33.9	24.6	18.2
W4	6.8	7.6	9	12.9	16.9	26.3	28.5	41	47	43.7	39.3	39	26.4	21.2	16
W5	6.3	6.7	8.1	12.8	18.6	26.3	32.6	42.6	46.4	47.6	40.7	39.5	30.4	21.8	16.3
W6	5.5	6	7.1	13.7	21.2	25.4	30.3	36.7	42.3	43.6	43.7	39.7	32.2	22	15.3
W7	6.4	6.6	9.3	14.3	22.9	30.8	33.4	38.6	42.6	44.6	41	37.6	30.5	21.8	15.5
T		4.8	7.3	14.2	20.4	25.9	29.5	34.6	40	38.2	34.2	31.7	26	18.9	13.8
E1	4.2	6.7	17.7	26.7	29.7	34.6	38.6	36.9	37.7	34.9	35.5	28.5	21.2	16.3	13.2
E2	4.5	8.3	23	34.1	37.3	39.7	38.1	40	38.5	42.6	29	24.1	18.9	16.8	13.4
E3	6	7.8	21.5	24.6	20.9	23.7	24.1	25.7	25.3	25.9	21.6	20.8	18.2	16.3	13.3
E4	6.7	6.6	19.8	29	33.3	34	33.5	30.3	33.9	28.1	21.1	20.1	17.5	15.7	11.6
E5	4.3	6.5	12	21.6	28.5	31.5	33	36.3	42.3	41.1	29.5	25.7	18.6	16.8	12.7
E6	5.3	7	17	27.7	34.6	40	39.6	43.4	43.7	35	32.8	27.5	18.8	15.8	12.8
EndT			8:09	9:07	10:08	10:34	11:07	12:08	13:09	14:02	15:25	16:05	17:08	18:06	
WDS				SE2	SE1	SE2	S	SE1	SE1	0		0			0
StartT	6:39	7:05	8:02	9:02	10:02	10:33	11:03	12:05	13:05	14:06	15:23	16:03	17:05	18:04	
N1	5	6.2	14.6	22.1	27.5	31.2	32.9	34.8	38.3	38.8	31.5	32	24.9	18.6	14.2
N2	5.2	5.8	11.4	20	27.5	31.1	34.3	36.5	40.7	42.3	36.5	34.1	26.1	19	14.5
N3	4	6	10.2	13	16	20.3	21.1	30.5	36.5	37.6	34	29.6	22.7	17.1	14.1
N4	4.8	6	8.7	12.1	17.4	20.8	23	25.4	29	27.5	25.2	25.5	20	16.6	13.6
N5	3.3	4.6	8	12.3	18.1	21	24.6	26.4	30.5	31.4	27.6	23.2	18.5	15.1	11.4
N6	4.2	5.1	7.9	11.7	16.9	19.8	24.8	27.5	34.2	36.5	33.2	30.6	25	17.6	13.9
N7	3.4	4.2	7.2	12.9	18.9	22.3	25.9	30	35.5	34.6	33.5	31.5	24.2	17.2	12.8
N8	3.7	4.4	7.9	13.9	18.9	22.2	29.6	34.2	36.8	41	36	34.5	25.3	16.9	12.2
T		4.8	7.9	16.8	23	26.9	26.2	30.7	33.8	38.8	34	32	26.1	17.5	13.3
S1	5.6	6.5	12	23	33.8	36.2	43.1	44.3	48.6	47.2	40.1	34.9	26.2	19.3	15.2
S2	5.2	6.5	12.6	17.9	25	27.7	30.1	38.5	46.2	44.4	39	36.3	27	18.9	15.2
S3	5.2	6	9	14.2	26	33.2	37.4	46.2	51.3	49.7	45.3	42.8	32.6	21.4	16.1
S4	6.9	7.4	10.4	14.6	23	24.5	35.6	34	38.3	50.7	49	47.2	35.6	23.6	17.6
S5	8.4	8.7	12.3	18.1	25.7	32	32.4	36	36.6	41	36.8	31.8	28.1	22	18.2
S6	7.3	8.2	12.1	16.5	24.5	28.2	34.3	36.9	41.9	48.1	42	39.5	31.8	23.6	19.2
S7	7	7.6	14.2	21.2	27.5	32.2	34.5	37.2	42.3	41.7	35.4	33.7	26.4	19.9	16.6
EndT	6:42	7:07	8:09	9:07	10:08	10:31	11:07	12:10	13:10	14:12	15:27	16:08	17:10	18:08	19:08
WDS				SE2	SE1	SE2	S	SE2	SE2	0		0			0

StartT: measuring start time

EndT: measuring end time

WDS: wind direction and speed

N1-N8, E1-E6, S1-S7, W1-W7, and T: measuring points

Appendix 6.3: Surface Temperature Measurements for A Coal Dump Pile in Wuda Coal Mine Area, Inner Mongolia, China. 23rd September 2002

StartT	6:50	7:12	8:12	9:11	10:11	10:39	11:10	12:14	13:13	14:16	15:31	16:11	17:17	18:12	19:11
NL	6.4	6.5	9.9	14.3	18.1	21.8	24.2	26.3	27	28.5	28.3	27.2	22.1	18.6	15.3
NM	6.1	6.7	10.1	12.2	13.4	15.7	17.8	19.4	20.3	22.2	20.5	20.2	20.6	17.6	14.2
NU	4.8	5.3	9.5	13.3	17	18.6	20.6	25.9	25.2	25.9	22.2	22.4	21.5	17	13.6
SEL	6.2	10.4	20.7	29.6	36.5	40.1	41.5	39.6	43	41.4	34.7	29.6	23.1	19.8	17
SEM	5.8	7.3	16.1	25.6	33	36	39.6	40.7	40	42.5	36.2	35.8	25.9	20.6	17
SEU	5.5	8.8	20.4	27.7	33.3	34.7	34.9	36.9	38.4	43.4	37.7	33.4	22.5	17.4	13.6
Diff	1.6	5.1	11.2	17.4	23.1	24.4	23.7	21.3	22.7	21.2	17.2	15.6	5.3	3.6	3.4
AirT			14.7		22.3	23.2	11.13	26.5	29.1	29.5			24.9		
WDS					SE2			SW2	SW1		WNW			21.2	18.1
EndT			8.17	9.13	10.17	10.44	23.9	12.16	13.1	14.19	15.32	16.13	17.2	18.1	19.12

StartT: measuring start time; EndT: measuring end time; WDS: wind direction and speed; NL, NM, NU, SEL, SEM, and SEU: measuring points; Diff: Max (NL, NM, NU, SEU, SEM, SEL) – Min (NL, NM, NU, SEU, SEM, SEL); AirT: air temperature

Appendix 6.4: Surface Temperature Measurements for A Crack in Wuda Coal Mine Area, Inner Mongolia, China. 23rd September 2002.

Start T		6:30	6:56	8:00	9:00	10:00	10:30	11:00	12:00	13:00	14:00	15:18	16:00	17:00	18:00	19:00
	DDA															
AirT						22.1	22.8	23.7	27	27.1	30.5		29	24.3	22.4	
SW1	20/10	7.9	7.6	14.6	22.7	28.4	33	36.5	40	41.1	43.3	40	35.5	28.3	21.6	17.3
SW2	30/12	8	8	15.6	24.7	29.6	34.5	38.2	40.3	40.8	42.9	38.7	33.9	27.7	21.4	17.3
SW3	30/18	10.3	9.9	16.3	25.9	30.5	34.5	38.1	39.3	38.5	41.4	37.6	33.3	27.5	22.8	18.8
SW4	35/19	10.5	10.2	18.9	28	31	34.8	38.1	38	37.5	41.1	37.9	33.5	28.5	24.8	21.1
SW5	30/18	15.9	15	21.8	31.2	36.5	39	42.5	44.4	44.7	46.5	47.5	45	41.5	33.4	28.6
SW6	30/18	16.5	18.2	26.4	34.9	38.5	42.6	44.3	43.8	43.9	47.5	59.9	54	52.3	39.9	33.4
C		239	239	238	239	236	235	235	234	233	237	238	237	237	236	235
NE1		24.8	28.5	28	33	37	45.2	50.6	61.5	64	69.2	75.7	73.5	70.6	49	44
NE2		14.2	16.2	18.4	25.9	30.3	35.9	41.6	51.1	54.8	58.7	66.9	67.7	63.6	42.6	44
NE3		7.4	7.9	12.5	20.8	27.2	31.7	36.9	40.3	43.4	46.9	48.2	45.5	39.6	25.6	32.8
NE4		7	8.2	14.4	23.4	26.5	33.1	35.4	35.6	38.5	39.9	42.5	38	30	21.8	20.2
NE5		6.5	7	12.1	19.9	23	30.3	33.8	36.8	38.1	38.1	36.5	33.4	25.3	19.5	18.4
NE6	50/7	6.7	7	13.5	21.3	25.5	31	34.2	36.5	36.9	36.8	34.3	30.4	22.6	19.2	15.8
NE7	56/19	5.8	6.2	14.2	22.9	27.8	32.5	33.8	35.8	35.1	35.1	33.6	31	21.2	17.6	14.4
NE8	70/23	6.2	6.2	15.9	26.5	30.8	35.4	37.5	38.6	36.8	34.9	31.5	28.2	20.6	17.1	14.8
NE9	50/9	8.5	7.2	14	20.4	25.3	30.7	32.5	36	36.5	37	36.3	31.3	23.4	18.9	16.9
NE10	310/11	8.2	8.3	13.7	21.6	23.2	28.7	31	34.8	35.8	37.7	38.4	33.2	25	19.3	16.5
EndT		6:34	7:02		9:02	10:02	10:32	11:02		13:04	14:05	15:22	16:02	17:04	18:04	19:02
WDS				SE2	SSE1	SE1	SE1	SE1		SE2	S2	W1	W1	W1	0	

StartT: measuring start time; EndT: measuring end time; WDS: wind direction and speed; AirT: air temperature; SW1 to SW6, C, NE1 to NE10: measuring points; DDA: Dip direction and dip angle for the plane that the measuring point located on.

Appendix 6.5: Statistical Characteristics of Thermal Anomalous Areas on ETM+ Night Image (28 September 2002). Page: 1/2

FN	Pixel Number					Maximum					Minimum					Mean				
	A	Background Neighborhood				A	Background Neighborhood				A	Background Neighborhood				A	Background Neighborhood			
		1	6	11	16		1	6	11	16		1	6	11	16		1	6	11	16
21	102	71	197	399	543	143	103	103	103	103	98	93	89	87	87	107	97	96	95	95
11	86	71	206	378	474	132	128	128	128	128	113	104	103	101	101	120	111	109	108	108
33	80	70	205	425	584	140	113	113	113	113	106	97	92	89	89	119	107	104	103	102
41	78	88	277	565	731	130	112	112	117	117	105	94	89	87	87	113	102	100	99	99
44	54	52	140	289	384	130	120	120	120	120	102	90	87	87	87	115	98	96	96	96
37	51	54	176	386	544	140	110	110	110	110	103	93	89	89	89	116	103	101	99	98
25	39	56	193	416	572	119	109	109	109	109	103	94	88	83	81	112	101	98	95	94
43	36	31	96	212	280	129	108	108	108	108	104	97	93	88	87	114	103	100	99	98
7	36	32	87	183	257	125	117	117	117	117	115	109	107	106	105	118	113	112	111	110
8	31	64	252	625	870	125	114	114	114	114	110	101	99	99	97	116	109	106	105	104
1	27	21	73	181	273	124	114	115	115	115	107	102	100	100	100	117	109	107	106	106
40	24	38	139	297	395	141	107	107	109	110	109	100	96	93	93	117	103	101	101	100
23	22	32	108	244	354	130	104	104	104	104	104	95	93	92	91	113	99	98	98	97
12	21	25	74	146	188	134	117	117	117	117	116	107	105	102	102	119	111	109	108	107
10	21	43	140	286	362	127	118	118	118	118	115	110	107	106	104	118	113	112	111	111
35	13	21	87	216	320	122	110	110	110	110	108	97	95	89	89	113	102	101	100	99
3	13	20	84	218	314	117	113	113	113	113	112	104	102	102	101	114	110	108	107	107
36	11	16	56	146	217	124	106	106	109	109	110	96	95	94	91	117	100	99	99	99
17	10	16	47	95	131	121	115	115	115	115	115	108	107	106	104	118	112	111	110	110
22	10	20	77	176	245	114	104	104	104	104	105	96	92	90	90	109	100	98	97	97
45	8	11	45	120	176	125	106	106	106	107	107	94	91	89	89	112	101	97	96	96
31	7	11	45	126	200	121	106	106	106	106	106	95	91	90	90	111	101	98	96	97
5	6	10	42	120	192	119	114	114	114	114	115	110	107	106	104	117	111	110	110	109
6	6	18	86	221	331	117	113	113	113	113	112	107	103	101	100	114	110	108	107	107
34	6	9	39	114	177	128	106	118	118	118	112	101	98	96	94	120	104	104	103	102
13	5	11	38	74	99	118	113	113	113	113	116	106	103	102	100	117	109	108	107	106
24	5	9	39	114	175	113	96	96	101	101	107	93	89	89	89	109	94	93	93	93
39	4	12	60	159	243	123	110	110	110	110	113	102	99	97	93	116	106	104	103	102
38	4	12	60	159	243	118	111	111	111	111	112	100	95	93	92	116	105	102	101	100
14	2	6	30	96	156	114	111	111	111	111	112	105	101	100	100					

FN: Fire name number

A: Thermal anomalous area manually extracted from Night2002 image

Appendix 6.5: Statistical Characteristics of Thermal Anomalous Areas on ETM+ Night Image (28 September 2002). Page: 2/2

FN	Standard deviation					Skewness					Kurtosis				
	A	Background Neighborhood				A	Background Neighborhood				A	Background Neighborhood			
		1	6	11	16		1	6	11	16		1	6	11	16
21	6.77	1.80	2.30	2.49	2.50	2.03	0.27	-0.04	-0.19	-0.09	6.74	0.89	-0.10	0.08	-0.04
11	3.95	3.65	3.42	3.20	3.13	0.61	1.19	0.98	0.87	0.86	0.07	4.59	3.29	3.20	3.12
33	7.92	3.25	4.13	4.48	4.47	0.69	-0.54	-0.59	-0.46	-0.29	-0.19	0.54	0.16	0.08	-0.08
41	5.96	3.45	3.90	4.10	4.11	1.03	0.32	-0.08	0.06	0.12	0.45	-0.05	0.28	0.79	0.57
44	7.89	4.28	3.85	3.36	3.21	0.10	2.31	1.25	0.91	0.78	-1.36	10.85	8.58	7.44	6.80
37	7.26	3.99	4.21	4.44	4.37	1.24	-0.28	-0.10	0.17	0.33	1.69	-0.67	-0.60	-0.64	-0.49
25	4.25	3.40	4.11	5.13	5.22	0.11	0.00	-0.02	0.14	0.29	-1.09	-0.47	-0.41	-0.56	-0.39
43	5.56	2.88	3.02	3.67	3.97	1.08	-0.22	0.29	-0.70	-0.76	1.06	-0.58	-0.09	0.95	0.54
7	2.06	2.07	2.36	2.40	2.41	1.19	-0.56	0.07	0.47	0.54	1.57	-0.63	-1.06	-0.52	-0.28
8	3.87	3.57	3.53	3.12	3.11	0.84	-0.23	0.36	0.67	0.60	-0.28	-0.78	-0.65	0.13	0.24
1	4.15	3.83	3.86	3.46	3.32	-0.22	-0.17	0.27	0.46	0.55	-0.31	-1.31	-0.73	-0.64	-0.47
40	8.89	2.01	2.40	2.67	2.86	1.47	0.29	0.31	0.22	0.31	1.34	-0.82	-0.05	0.29	0.21
23	5.97	2.06	2.32	2.69	2.78	0.78	-0.17	0.25	0.30	0.29	0.87	-0.03	-0.47	-0.56	-0.41
12	4.19	2.62	2.70	2.90	2.90	2.11	0.22	0.53	0.50	0.56	4.38	-0.51	-0.24	0.06	0.28
10	3.17	1.76	2.26	2.27	2.37	1.18	-0.01	-0.05	0.12	0.10	0.44	-0.09	-0.61	-0.40	-0.15
35	4.32	3.56	3.67	4.07	4.09	0.42	-0.08	0.35	0.11	0.24	-0.99	-0.88	-0.60	-0.12	-0.20
3	1.33	2.02	2.13	2.14	2.16	0.33	-0.94	-0.46	0.00	0.19	-0.59	1.02	0.23	-0.09	-0.09
36	4.77	2.80	2.58	2.92	3.06	0.10	0.43	0.86	0.71	0.41	-1.61	-0.62	0.34	0.18	0.02
17	1.71	1.75	2.03	2.16	2.09	0.44	-0.53	-0.13	-0.10	-0.16	-0.74	-0.23	-0.95	-1.01	-0.52
22	3.51	2.32	2.67	3.01	2.93	0.12	-0.19	-0.08	0.05	0.23	-1.82	-1.10	-0.70	-0.75	-0.71
45	5.66	3.42	3.60	3.30	3.62	1.39	-0.52	0.53	0.56	0.55	0.59	-0.31	-0.30	0.07	0.09
31	5.79	3.03	3.49	3.32	3.02	0.71	-0.20	0.11	0.16	0.13	-1.47	-0.81	-0.57	-0.49	-0.31
5	1.55	1.25	1.89	1.92	1.89	0.00	0.72	0.34	0.33	0.22	-1.96	-0.46	-0.68	-0.53	-0.12
6	1.72	2.23	2.67	2.64	2.58	0.38	-0.04	-0.19	0.16	0.27	-1.32	-1.50	-0.94	-0.80	-0.47
34	6.60	1.69	3.40	3.37	3.47	0.24	-0.29	1.69	1.21	0.85	-1.89	-1.17	5.64	3.14	2.36
13	0.71	2.29	2.50	2.77	3.00	0.00	0.05	-0.11	0.36	0.51	-1.40	-1.57	-0.78	-0.74	-0.59
24	2.51	1.00	1.72	1.63	1.79	0.97	0.07	-0.91	0.46	0.88	-1.04	-1.37	0.49	3.85	2.78
39	4.72	2.77	3.09	3.14	3.41	0.57	0.41	0.28	0.16	0.14	-1.84	-1.41	-0.80	-0.65	-0.46
38	2.52	3.66	3.18	3.25	3.40	-0.42	0.24	0.55	0.29	0.03	-1.82	-1.47	0.14	0.32	0.27
14															

Appendix 6.6: Statistical Characteristics of Thermal Anomalous Areas on ETM+ Day Image (21 September 2002). Page: 1/2

FN	Pixel Number					Maximum					Minimum					Mean				
	A	Background Neighborhood				A	Background Neighborhood				A	Background Neighborhood				A	Background Neighborhood			
		1	6	11	16		1	6	11	16		1	6	11	16		1	6	11	16
43	76	51	138	268	341	209	184	184	184	184	172	146	141	119	119	186	167	163	160	158
33	53	63	223	517	678	197	177	183	183	183	171	146	122	120	120	182	166	161	159	158
41	48	55	184	411	563	196	177	181	189	189	168	132	111	111	106	180	162	155	151	151
11	46	52	170	370	504	207	196	196	196	196	190	171	165	158	158	197	184	181	178	177
44	39	42	134	288	371	206	182	182	182	187	176	128	123	114	114	189	163	157	156	156
37	35	24	82	199	297	210	173	173	177	177	170	146	118	114	114	187	162	157	154	153
1	31	29	93	219	320	211	198	198	199	206	199	177	165	165	163	203	191	186	183	183
40	25	33	110	248	347	192	171	179	179	179	172	142	133	123	123	178	162	157	151	149
45	23	27	99	206	289	190	173	173	173	173	175	140	130	129	118	182	162	156	153	152
25	22	29	84	156	209	186	173	178	185	185	170	137	120	120	116	179	164	162	158	155
34	17	18	66	168	256	216	177	187	187	187	177	147	140	131	122	190	168	164	159	157
22	14	24	94	218	319	193	177	177	177	177	175	154	125	114	114	184	168	159	149	146
39	11	13	51	138	216	195	174	182	182	182	172	138	136	136	136	182	162	162	158	159
21	10	22	89	208	298	246	171	174	174	175	172	131	120	120	120	191	163	153	147	146
35	9	17	75	211	313	203	176	181	181	182	179	155	143	129	120	189	168	164	163	161
23	9	14	54	144	224	199	171	177	186	186	175	138	119	119	119	185	159	148	146	146
12	6	9	36	96	139	195	187	190	195	195	190	180	171	165	165	192	184	184	181	181
13	4	4	15	39	60	199	186	190	196	197	190	174	172	172	172	196	181	181	184	186
24	2	6	30	96	153	209	179	186	187	187	186	171	135	128	117					
3	2	6	30	96	156	203	194	195	195	196	200	174	165	165	165					
7	2	8	48	132	208	200	190	190	190	190	195	184	174	164	160					
31	2	6	30	96	160	182	176	176	176	176	181	158	139	135	132					
10	1	4	24	84	144	198	188	190	190	190	198	180	164	163	157					
8	1	4	24	84	144	202	194	194	194	194	202	183	171	165	165					

FN: Fire name number

A: Thermal anomalous area manually extracted from Day2002 image

Appendix 6.6: Statistical Characteristics of Thermal Anomalous Areas on ETM+ Day Image (21 September 2002). Page: 2/2

FN	Standard deviation					Skewness					Kurtosis				
	A	Background Neighborhood				A	Background Neighborhood				A	Background Neighborhood			
		1	6	11	16		1	6	11	16		1	6	11	16
43	6.23	8.17	9.75	11.67	12.74	0.52	-0.55	-0.23	-0.72	-0.68	0.93	-0.01	-0.59	0.37	0.00
33	6.03	6.36	9.51	10.85	11.22	0.53	-0.55	-0.87	-0.93	-0.80	-0.41	0.02	1.61	1.47	0.88
41	5.95	10.70	15.52	16.26	16.21	0.56	-0.97	-0.85	-0.63	-0.59	0.58	-0.01	0.00	-0.38	-0.42
11	3.89	5.54	6.64	7.31	7.09	0.48	-0.27	-0.02	0.09	0.11	-0.55	-0.48	-0.70	-0.51	-0.50
44	6.72	12.06	13.71	13.64	13.48	0.24	-0.69	-0.60	-0.91	-0.83	-0.38	-0.10	-0.47	0.41	0.47
37	9.71	8.66	11.86	13.60	13.65	0.46	-0.51	-1.15	-0.87	-0.78	-0.21	-1.08	1.26	0.15	-0.15
1	3.66	5.89	7.13	7.11	7.73	0.77	-0.91	-0.25	0.10	0.22	-0.69	-0.37	-0.52	-0.50	-0.25
40	5.93	6.56	8.81	11.32	11.47	0.80	-0.84	-0.37	-0.33	-0.26	-0.48	0.46	-0.09	-0.52	-0.63
45	5.30	8.22	9.53	9.25	10.58	-0.11	-1.04	-0.61	-0.50	-0.77	-1.63	0.54	-0.22	-0.28	0.16
25	4.04	9.46	10.88	13.98	15.03	-0.47	-1.44	-1.42	-0.91	-0.68	-0.44	1.38	1.98	0.00	-0.46
34	10.54	9.43	8.99	9.83	10.86	0.94	-0.95	-0.28	-0.20	-0.69	-0.08	-0.49	0.06	0.11	0.97
22	6.07	7.29	12.40	15.09	14.77	0.16	-0.40	-0.64	-0.14	-0.03	-1.47	-1.21	-0.11	-0.80	-0.70
39	6.63	11.54	10.31	10.01	9.27	0.28	-0.81	-0.52	-0.04	-0.18	-0.84	-0.84	0.04	-0.45	-0.31
21	24.03	9.29	14.19	14.49	13.40	1.31	-1.83	-0.77	-0.08	0.01	0.15	3.48	-0.40	-1.12	-0.90
35	7.60	6.80	9.27	8.49	10.96	0.48	-0.78	-0.51	-0.83	-0.94	-1.15	-0.79	-0.67	0.86	0.90
23	7.40	9.27	15.07	15.03	13.37	0.56	-0.58	-0.04	0.41	0.43	-0.92	-0.38	-0.87	-0.55	-0.15
12	1.94	2.40	5.41	6.80	7.07	0.08	-0.06	-0.78	-0.21	-0.13	-1.71	-1.67	-0.26	-0.75	-0.72
13	3.87	5.38	4.93	5.57	5.82	-0.52	-0.22	-0.01	0.15	-0.18	-1.81	-2.12	-1.04	-0.34	-0.51

Curriculum Vitae

Personal details:

Name: Jianzhong ZHANG
Sex: Male
Date of birth: April 23, 1964
Place of birth: Jilin, P.R. of China
Nationality: Chinese

Education:

1981 – 1985:
Department of Geography, Peking University, P. R. of China. Bachelor of Science in Geography.

1985 - 1988:
Department of Geography, Peking University, P. R. of China. Master of Science in Geography.

1994 - 1996:
Geological Division, International Institute for Aerospace Survey and Geosciences, The Netherlands. Master of Science in Geology.

Work Experience:

1988 – 2000:
Chinese Academy of Sciences, Institute of Remote Sensing Applications, Beijing, P. R. of China. Assistant professor to associate professor. Research on oil and gas exploration using remote sensing techniques.

2001 – 2004:
German Aerospace Center, German Remote Sensing Data Center, Oberpfaffenhofen, Germany. Ph.D Researcher. Research on coal fire detection by thermal remote sensing images.

Wien, 2004-04-01